Technical Report

TR-00-23

Inspection of copper canisters for spent nuclear fuel by means of ultrasound

Electron beam evaluation, harmonic imaging, materials characterization, and ultrasonic modelling

Ping Wu, Fredrik Lingvall, Tadeusz Stepinski

Uppsala University, Signals and Systems,
Department of Materials Science, Sweden

December 2000

Svensk Kärnbränslehantering AB
Swedish Nuclear Fuel
and Waste Management Co
Box 5864
SE-102 40 Stockholm Sweden
Tel 08-459 84 00
+46 8 459 84 00
Fax 08-661 57 19
+46 8 661 57 19

Inspection of copper canisters for spent nuclear fuel by means of ultrasound

Electron beam evaluation, harmonic imaging, materials characterization, and ultrasonic modelling

Ping Wu, Fredrik Lingvall, Tadeusz Stepinski

Uppsala University, Signals and Systems,
Department of Materials Science, Sweden

December 2000

Summary

This report presents the research in the sixth phase that is concerned with ultrasonic techniques for assessing electron beam (EB) welds in copper canisters. The research has been carried out in three main aspects: (1) comparative inspections of EB welds, (2) EB weld evaluation, and (3) quantitative evaluation of attenuation in copper.

Comparative inspections of EB welds in two copper canister blocks have been made by means of ultrasound and radiography. Comparison of the inspected results demonstrate that both techniques complement each other very well. The radiographic technique on the whole gives relatively better spatial resolution but low contrast in radiographs. It can reliably detect voids in EB, but cannot provide information about material structure in the EB weld. Ultrasonic technique provides information about flaw locations and shapes similar to the radiographs. Moreover, it can easily distinguish welded and non-welded zones and be used to study weld's macro- and microstructure. The defects in ultrasonic images often show higher contrast, and some flaw indications may be seen in ultrasonic inspection but not in radiographs. But small flaws are hard to distinguish from grain noise.

For EB weld evaluation, first, scattering from EB weld has been investigated using three broadband transducers with different center frequencies. The investigation has shown that more information on scattering and attenuation can be exploited in this case so that the EB welds can be better characterized, and that the best frequency range for characterizing welds is 2 – 5 MHz. Secondly, harmonic imaging (HI) of EB welds have been studied using two different sources of harmonics: (i) transducer harmonics, originating from the high-order resonant modes of transmitters excited by a broadband pulse, and (ii) material harmonics, stemming from the nonlinear distortion of waves propagating in materials. The transducer HI exploits additional information due to transducer harmonics, and higher order harmonic images have better spatial resolution. The material HI has been conducted on copper block CU2 and copper canister CAN 1 with an EB weld. The harmonics up to third order from the EB weld were clearly seen, and the fourth harmonic from artificial defects was visible. The results have demonstrated that the spatial resolution becomes better and the grain noise pattern becomes finer in higher harmonic images. The materials HI technique for ultrasonic NDE seem be promising and stimulating, similarly as the tissue HI technique in medical ultrasonography has resulted in significant improvement in image quality. Thirdly, signal processing investigations have been continued aiming to refine ultrasonic imaging and to perform better clutter suppression. Various filtering techniques have been applied to improve defect detectability, for example, standard matched filtering, wavelet filters, etc. A common requirement for success of these approaches is the presence of a significant difference in ultrasonic responses from defects (voids) and weld clutter. The results from the filtering experiments indicate that it does not seem to be enough difference between the responses from artificial defects and welds to construct a good clutter suppression/detection algorithm of the form used here, and the gain in terms of signal-to-noise ratio is, therefore, not dramatic after processing. However, filtering had some positive effects, e.g., 2-D matched filters removed the unwanted, low frequency oscillations coming from the transmitter and smoothened the images. Even the C-scan image quality could be slightly improved without losing spatial resolution. Processing (or deconvolving) the US data with a Wiener filter has shown a substantial improvement in temporal resolution so that the layered structure in the weld is much easier to see.

Quantitative evaluation of attenuation in copper block CAN 1 has been carried out in immersion-pulse-echo scheme using two focused transducers with different frequencies. The effective geometrical parameters of the transducers were first determined using a novel method developed based on the spatial impulse response theory. Then the diffraction effects of the transducers were corrected using the angular spectrum approach (ASA) that was implemented with a newly-developed algorithm, *θ -space* algorithm, that is more efficient and accurate than the existing *k-space* algorithm. The evaluated attenuation in the copper canister is small, around 0.1 dB/mm at 4 MHz.

Sammanfattning

Denna rapport innehåller fas 6 av forskningsprojektet gällande ultraljudstekniker för att säkerställa elektronstrålesvetsar (EB-svetsar) i kopparkanistrar. De tre huvudaspekter som har undersöks är:
(1) jämförande inspektioner av EB-svetstar, (2) EB-svets utvärderning och (3) kvantitativ uppskattning av dämpning i koppar. Jämförande inspektionerna av EB-svetsar har utförts mha. ultraljud och radiografi i två kopparkanisterblock. Resultaten från undersökningarna med dessa två tekniker kompletterar varandra mycket väl. Radiografimetoden ger generellt bättre spatiell upplösning än ultraljudsmetoden men kontrasten är relativt låg i radiogrammen. Radiografimetoden kan detektera defekter tillförlitligt men ger ingen information om materialstruktur i EB-svetsen. Ultraljudsmetoden ger dock information om sprickors position och form, på ett sätt som liknar radiogram. Utöver detta, så är det också enkelt att särskilja svetsområden från övriga områden i kopparblocken. Dessutom går det att studera svetsens macro- och microstruktur med metoden. Ultraljudsbilder har också högre kontrast än radiogrammen och vissa sprickor syns endast mha. ultraljudsmetoden. Notera dock att små sprickor kan vara svåra att särskilja från materialbruset (bakspridning).
Flera aspekter av ultraljudundersökning av EB-svetsen har beaktats. Först har spridningen från svetsen undersökts med tre bredbandiga sökare med olika centerfrekvens. Resultaten från dessa försök visar att mera information ang. spridining och dämpning har erhållits jämfört med om endast en sökare använts, vilket ger en bättre karakterisering av EB-svetsen. Det mest lämpliga frekvensområdet för ultraljudsinspektion ligger inom 2 - 5 MHz. För det andra har harmoniska komponenter (eng. harmonic imaging (HI)) studerats. Dessa härstammande från två olika källor (i) sökarkomponenter vilka kommer från högre ordningens resonanta moder hos sändaren som exciteras av en bredbandig puls, samt (ii) materialkomponenter, vilka härstammar från ickelinjär distortion hos vågor propagerande i ett material. Genom utnyttjande av sökarens harmoniska komponenter erhålls bilder med bättre spatiell upplösing. Material-harmoniska komponenter har undersökts på ett kopparblock CU2 samt ett kopparkanisterblock CAN1 innehållande en EB-svets. Harmoniska komponenter upp till ordning tre kan enkelt observeras, samt även 4:e ordningens komponenter från artficiella defekter. Resultaten visar också att den spatiella upplösningen ökar i bilder där högre ordnings harmoniska komponenter utnyttjas samt att materialbrusmönstret blir finare. Metoder som utnyttjar material-harmoniska komponenter ser lovande ut och är en mycket intressant teknik för NDE applikationer precis som vävnads-harmoniska komponenter har blivit för medicinska tillämpningar.
För det tredje har också undersökningar med signalbehandlingsmetoder fortsatt och vidareutvecklats. Målet med dessa metoder är att ge förbättrade ultraljudsbilder samt att ge bättre material-brusundertryckning. Olika filtermetoder har använts för att förbättra defekt detekterbarheten, bl.a. har matchade filter och wavelets använts. Ett krav för att dessa metoder skall fungera är att det finns en signifikant skillnad hos ultraljudsresponsen från defekter och svetsstrukturen. Resultatet från filterexperimenten pekar dock på att denna skillnad är liten vilket medför att förbättringen i termer av signal-till-brusförhållande blev relativt liten. Experiment med 2D-matchade filter tar dock bort oönskade lågfrekventa oscillationer härrörande från sändaren, samt "mjukade upp" ultraljudsbilderna. Även C-scanbilderna visade en viss förbättring utan att den spatiella upplösningen försämrades. Avfaltning mha. Wiener-filtrering visade sig ge en påtaglig förbättring av tidsupplösningen vilket medför att lagerstrukturen hos EB-svetsen blir mycket lättare att observera.
Puls-eko mätningar i immersion med två fokuserade sökare med två olika centerfrekvenser har använts för att ge en kvantitativ utvärdering av dämpning hos CAN 1 kopparblocket. En ny metod har använts för att bestämma de geometriska parametrarna hos sökaren vilken är baserad på den spatiella impulssvars teorin. Kompensation för diffraktionseffekter hos sökaren har gjorts mha. ASA-algoritmen (eng. angular spectrum approach) vilken har implemanterats med en ny rums-algoritm vilken är effektivare och noggrannare än den traditionella k-rums algoritmen. Den funna dämpningen i kopparkanistern är liten, ca. 0.1 dB/mm vid 4 MHz.

CONTENTS

1 Comparative Inspections of Electron Beam Welds

1.1 Introduction - radiographic and ultrasonic inspections

Radiography and ultrasonics are of the most commonly used techniques in nondestructive evaluation (NDE). They have been chosen by SKB for inspecting EB welds of copper canisters. In the present work these two methods have been compared based on the inspection results (the radiographic and ultrasonic images) of EB welds in two copper canister specimens, CAN 1 and W123-3. The geometry of the first specimen (CAN 1) is shown in Fig. 1.1. This specimen contains artificial defects, i.e., nine pairs of holes, of which the first nine (#1 to #9) are in the EB weld zone and the second (#10 to #18) outside the weld zone. The second specimen (W123-3) is a segment of copper canister W123, and it contains some natural flaws or defects.

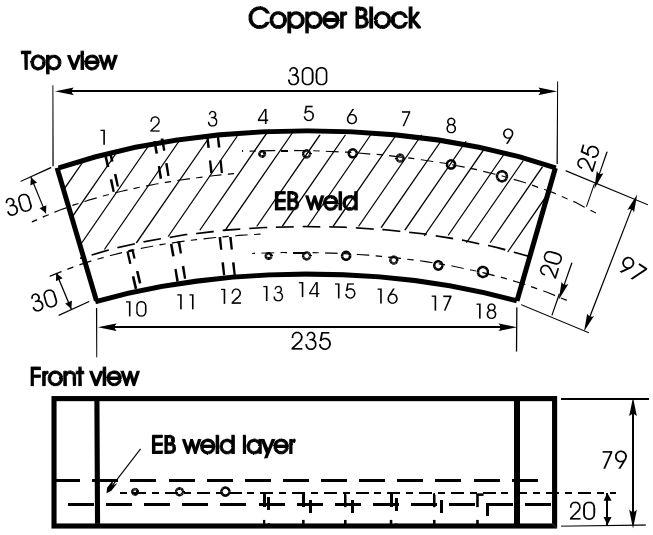

Hole No.	1	2	3	4	5	6	7	8	9
	10	11	12	13	14	15	16	17	18
Type	SDH			FBH			RBH		
Diameter	1.0	1.5	2.0	1.5	2.0	2.5	2.0	2.5	3.0

Fig. 1.1. Geometry of the inspected copper block CAN 1.

The radiographic inspection of CAN 1 and W123-3 was performed at the SKB Canister laboratory in Oskarshamn. The ultrasonic inspection of two specimens was carried out using a new transducer connected to the ALLIN ultrasonic system in our laboratory. The experimental setup used for this inspection is shown in Fig. 1.2. The new transducer was specially designed for harmonic imaging. It has two spherically concentric elements with radius of curvature of 210 mm. The inner element is circular with a 20-mm diameter, and has a 4.83-MHz center frequency with a 73% bandwidth. The outer element is annular with an approximate 20-mm inner diameter and a 38-mm outer diameter, and

has a 2.26-MHz center frequency with a 69% bandwidth. The reasons for using the transducer instead of the ALLIN array are as follows:

(i) to test the performance of the new transducer,

(ii) to facilitate the data processing and illustration, and

(iii) to examine the welds in two different frequency bands.

To fully image the above-mentioned two specimens, we need a scanning width (y) of 85~95 mm and a scanning length (x) of 250~300 mm. Since the ALLIN array consists of 64 elements with a 1-mm spacing, the width of a C-scan will be 33 mm for the 32-element aperture, and 49 mm for a 16-element aperture. In the former case we would need three measurements (stored in three data files), and in the latter case, two measurements to acquire a complete C-scan. Since the ALLIN array has a center frequency of 3.1 MHz with a bandwidth of 58%, the center frequencies of 2.26 and 4.83 MHz may extend the frequency range of inspecting EB welds and provide more information on EB welds.

For both specimens the measurements were made in immersion configuration and in pulse-echo mode. The outer and inner elements were used separately, both in pulse echo mode. The measured sound velocities (of longitudinal waves) in copper and water were 4596 and 1485 m/s, respectively. The water column was set to 30 mm, and thus the focal zone of the transducer was positioned about 60 mm inside the copper block, the depth around which the EB weld was located, so that the best spatial resolution zone was set around the EB weld. The scanning region was 85x270 mm for CAN 1 and 85x290 mm for W123-3. The scanning interval was 1mm for both cases. Comparative inspections of the two specimens by means of the radiographic and ultrasonic techniques are presented in Sects. 1.2 and 1.3, respectively, and the conclusions and given in Sect. 1.4.

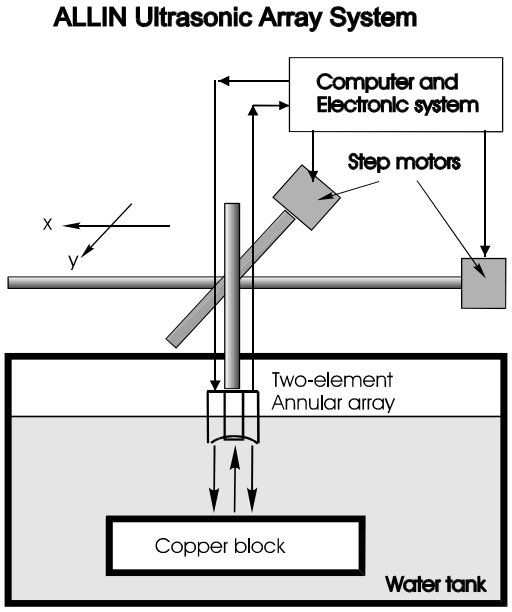

Fig. 1.2. Experimental system and measurement setup.

The comparison of the results from the inspections is based on C-scans of the EB welds because the C-scans presentation provides information similar to that contained in radiographic images.

1.2 Comparative inspection of the EB weld in CAN 1

The radiographs of the EB weld in copper block CAN 1 are shown Fig. 1.3 in which (a) and (b) are the side and top views of the weld, respectively. The contrast and brightness of the figure have been adjusted to get the best illustration of the artificial defects (the side- and bottom-drilled holes). From the images all nine pairs of holes can be seen. The side-view image (Fig. 1.3(a)) shows the side-drilled holes (SDH #1-3, #10-12) with high contrast and the bottom drilled holes with low contrast. The situation observed at the top-view image (Fig. 1.3(b)) is reversed, the bottom-drilled holes (FBH #4-6, #13-15, and RBH #7-9, #16-18) are characterized by high contrast and the SDHs by low contrast. The reason for that is simple, the contrast observed at the radiographic image increases with void size in the beam direction. At the edge (e.g., the edge on the right hand side in Fig. 1.3(b)) the SDHs look smooth in the radiograph. In the top-view image we can see an arc going in the middle, which is the interface between the canister wall and the lid. This interface can not be seen in the side-view image. In both views only a little information on the structure of EB welds can be captured, and the welded and non-welded zones can not be distinguished from the radiograph.

The ultrasonic scans of the EB weld from the 2.26- and 4.83-MHz transducers are shown in the form of C-scans in Figs. 1.4 and 1.5, respectively. The C-scans in the figures are all in top-view and they were obtained using the time gates set at different times (or depths). The C-scans are flipped left to right to facilitate the comparison with the radiographs. Appropriate gate adjustment for extracting C-scans is very important for the effective exploitation of information characterizing the inspected material, especially for EB welds that are layered media with large attenuation. Quite a detailed investigation of this problem has been done in our earlier work, cf. [2]. The C-scans in panel (a) of the figures are extracted using a gate that covers the fusion zone (FZ) of the EB weld. Since the SDHs and the tops of the bottom-drilled holes are located at 60 mm beneath the canister's surface, the depth where the FZ of the weld is located, the images of all the holes in the specimen are well pronounced in the C-scans in panel (a). The C-scans in panel (b), showing the interface between the wall and the lid, was constructed with the gate set deeper than the gate in panel (a) which means that the gate covered the interface between the back heat-affected zone (HAZ) and the host material. The interface might not be seen if the gate was not set properly because the scattering from the interface, although being stronger in the properly gated layer, can be weaker than the scattering from the grains in the FZ.

The C-scans in panels (a) and (b) in Figs. 1.4 and 1.5 jointly provide information on the weld that is similar to that obtained from the radiograph (Fig. 1.3(b)); that is, the nine pairs of the holes and the wall/lid interface are well pronounced. A comparison of Fig. 1.4 with Fig. 1.5 demonstrates that the image from the 2.26-MHz transducer has a better spatial resolution than that obtained using the 4.83-MHz transducer and the wall/lid interface shows a higher contrast. This is because the 2.26-MHz transducer, although having a lower center frequency, has a larger aperture than the 4.83-MHz transducer, and the lower frequency band results in less attenuated echoes. The resolution of the 2.26-MHz is comparable with that in the radiograph. From ultrasonic images the information on the structure of EB welds can be captured; for example, the layered structure and the grain difference in the layers are distinguishable. This is an advantage of the ultrasonic technique over the radiography. At the same time it is a disadvantage since scattering from the structure appears as grain noise that often masks flaws and hence makes the flaw more difficult to be detected.

Unlike in the radiographs, mapping of the SDHs in the ultrasonic images at the edge of the block is not perfect. This is because the block edge is inspected using only a part of the transducer aperture.

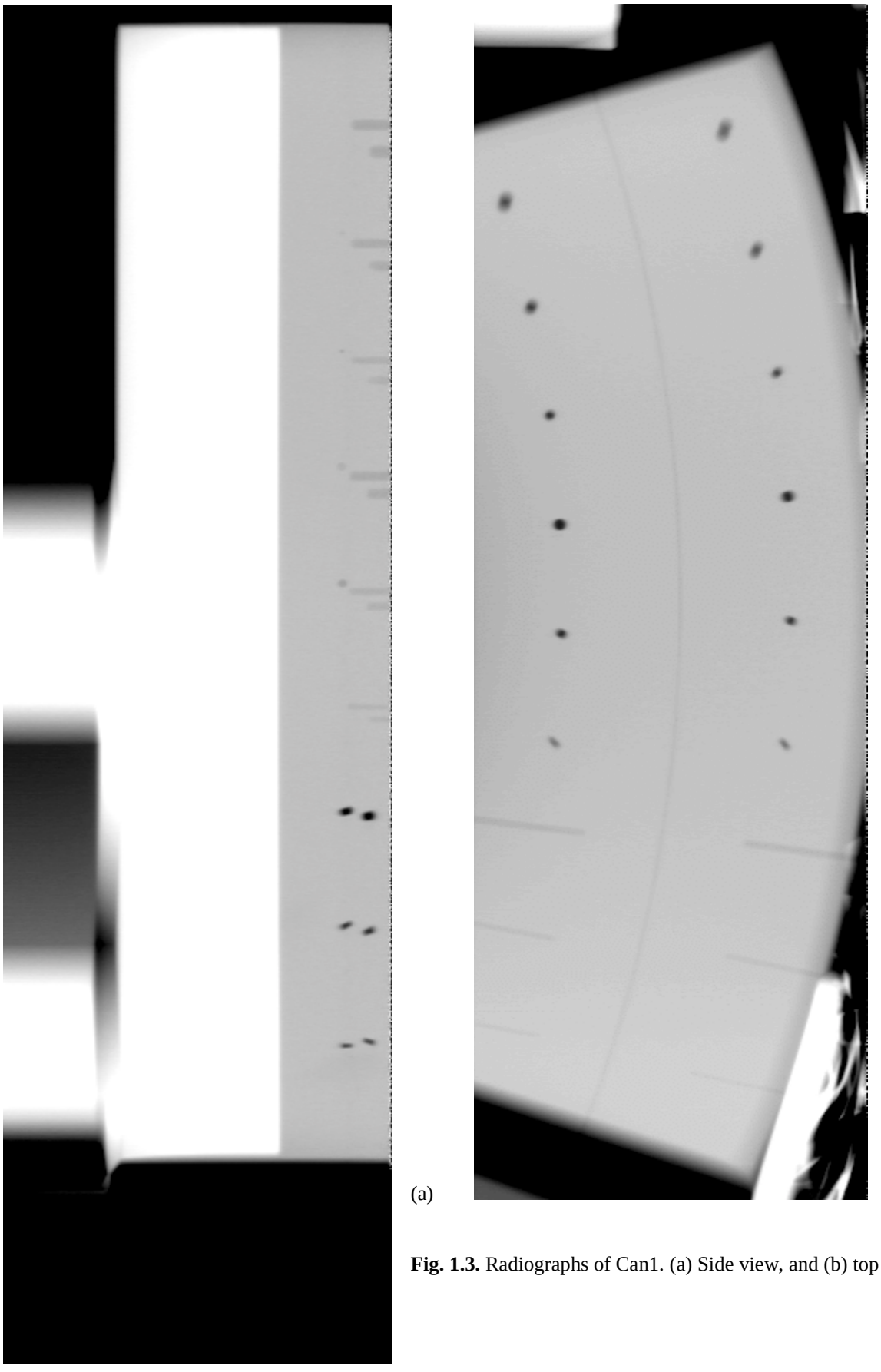

Fig. 1.3. Radiographs of Can1. (a) Side view, and (b) top view.

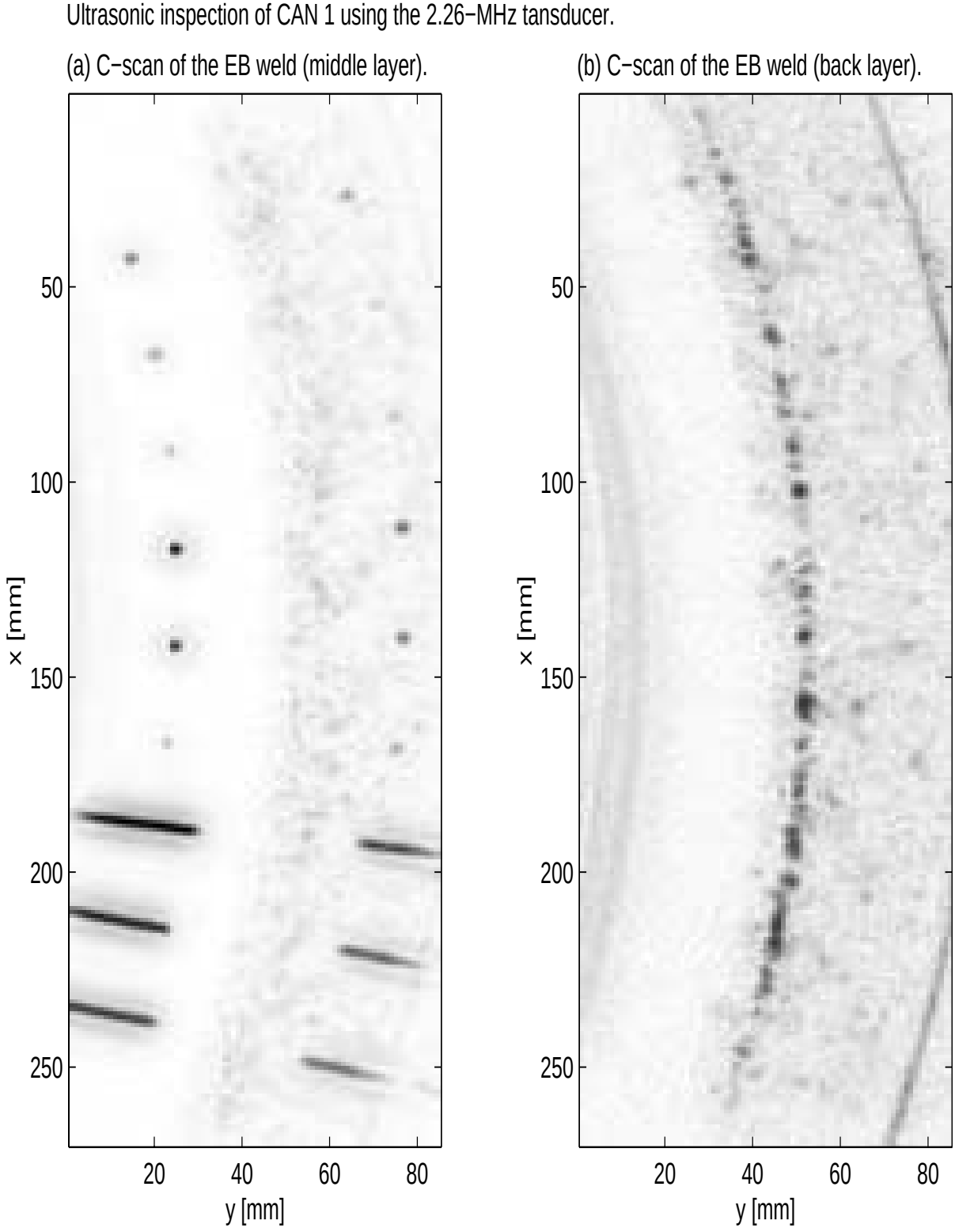

Fig. 1.4. Ultrasonic inspection of copper block CAN 1 using the 2.26 transducer. C-scans of copper block CAN 1 with the gates located over (a) the middle layer (the FZ) and (b) the back layer (the back HAZ), respectively.

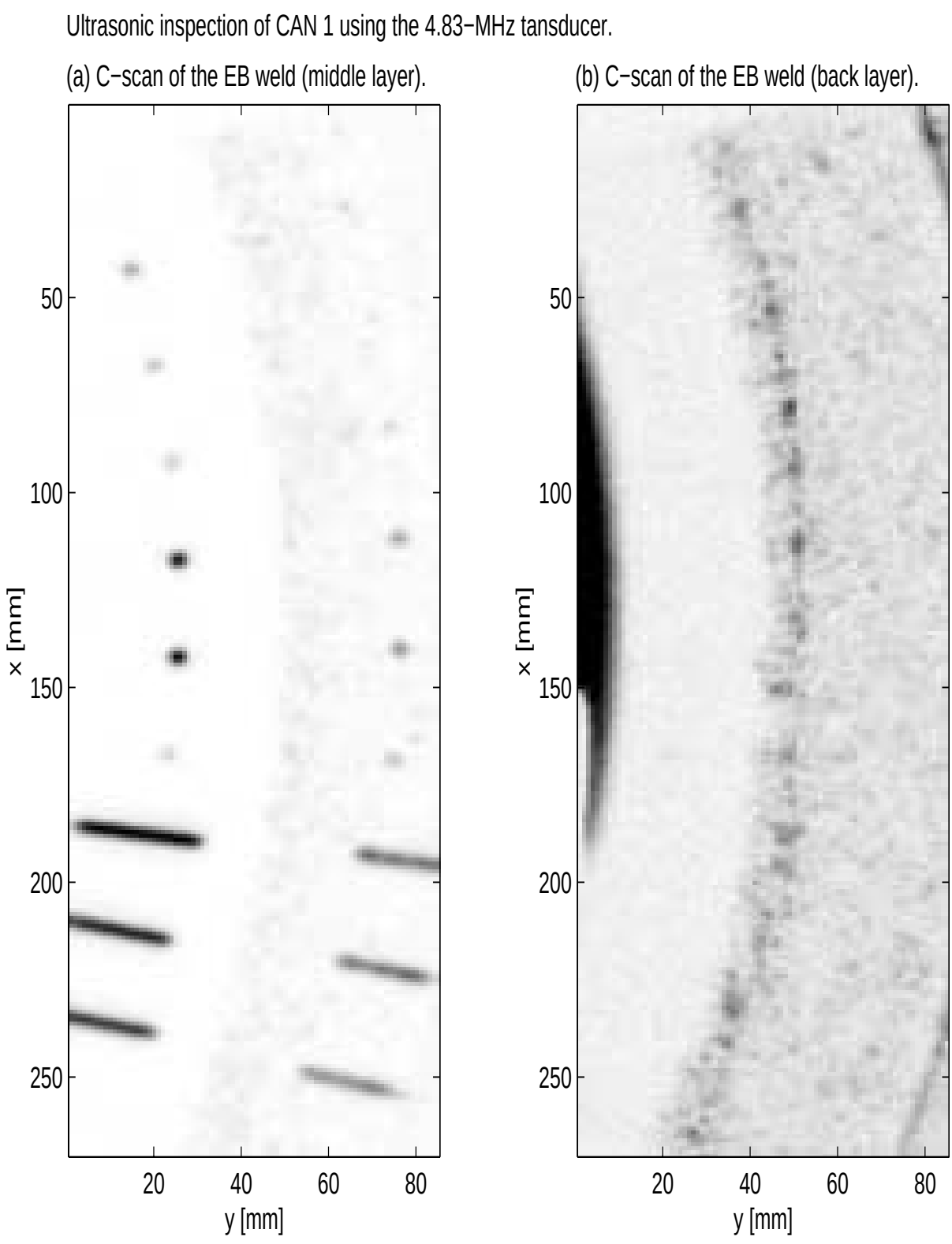

Fig. 1.5. Ultrasonic inspection of copper block CAN 1 using the 4.83 transducer. C-scans of copper block CAN 1 with the gates located over (a) the middle layer (the FZ) and (b) the back layer (the back HAZ), respectively.

1.3 Comparative inspection of the EB weld in W123-3

The radiographs are shown Fig. 1.6 in which (a) and (b) are the side and top views of the EB weld. The contrast and brightness in the figure are also adjusted to yield the best illustration of flaw indications. In the side-view image (Fig. 1.6(a)) five indications #1~5 and one reference indication #R1 can be seen. But in the top-view image (Fig. 1.6(b)) only the four (#1~4) of the five indications and another reference indication #R2 can be seen. Reference hole #R1 was a shallow hole drilled from the side at the EB weld, and reference hole #R2 was a top-drilled shallow hole. Indication #5 is shallow hole drilled from the outer side of the copper canister, and thus it can be distinguished at the side view (Fig. 1.6(a)) but not at the top view (Fig. 1.6(b)). The wall/lid interface is also clearly shown in the middle of the top-view image. The interface looks thicker than the one of CAN 1.

The ultrasonic images of the EB weld from the 2.26- and 4.83-MHz transducers are shown in Figs. 1.7 and 1.8, respectively. These C-scans were obtained using gate settings different from the previous case. The C-scans in panels (a) and (b) of the figures are all in top-view and they were obtained using the time gates set across the upper boundary (HAZ/FZ) and the lower boundary (FZ/HAZ) of the EB weld, respectively. The C-scans are also flipped left-to-right so that they look similar to the radiographs. The C-scans images of the wall/lid interface are not shown here for the sake of limiting the report size. However, they provide information similar to that found in the radiographic images.

It is worth noting that the indications #1, #3 and #4 can be seen in the C-scans in panels (a) of the figures, and the indications #2 and #5 are seen in panel (b). This means that indications #1, #3 and #4 are located deeper than indications #2 and #5. In addition to these five indications, some other indications labeled with ?1 and ?2 are seen in panel (a) of both figures, but they are not present in the radiograph.

Comparing Figs. 1.7 and 1.8, we can see that indications # 3 and #4 result in a higher contrast for the 2.26-MHz transducer and indication #5 has clearer shape and higher contrast. The spatial resolution for the 2.26-MHz transducer also looks better than for the 4.83-MHz transducer. This may reveal that the responses of some flaws and defects to ultrasonic waves with different frequency bands may be quite different and inspections of EB welds using different frequency bands can be complementary.

The advantages and disadvantages of the ultrasonic technique compared to the radiographic one are similar as in the previous case. The contrast of the indications in ultrasonic images is high (and thus better) than in the radiographs. Moreover, the indications ?1 and ?2 are seen in ultrasonic images but not in radiographic inspection. Only destructive inspection of the W123-3 can give an answer whether they correspond to real defects.

(a)

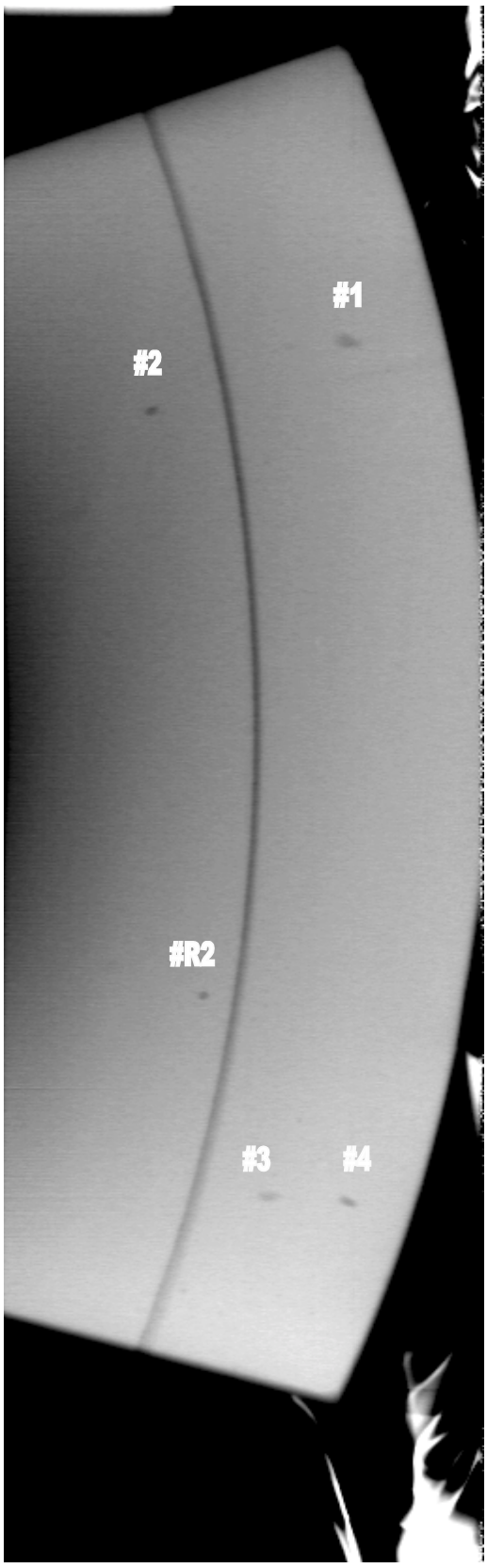

(b)

Fig. 1.6. Radiographs of W123-3. (a) Side view, and (b) top view.

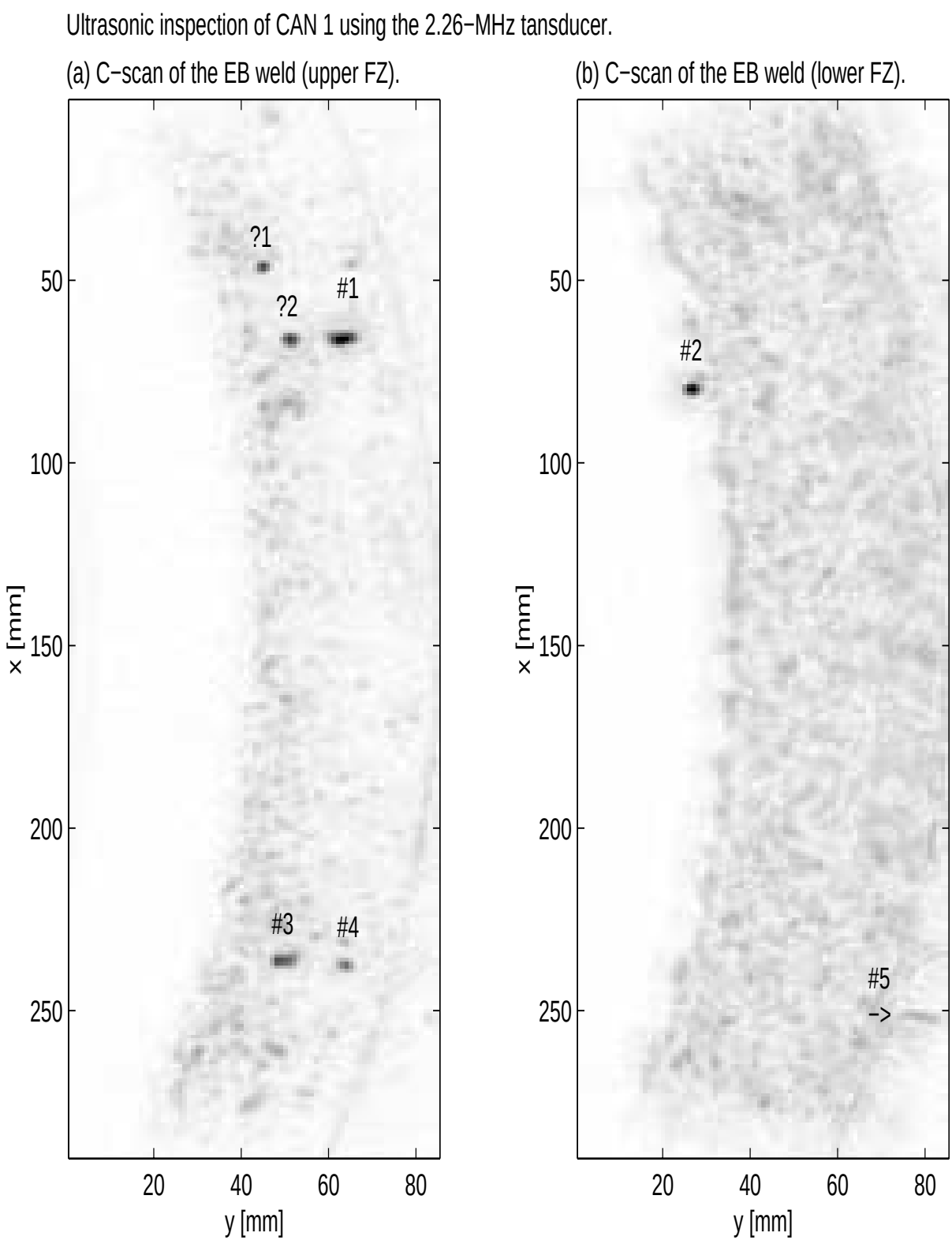

Fig. 1.7. Ultrasonic inspection of copper block W123-3 using the 2.26 transducer. C-scans of copper block W123-3 with the gates located across (a) the upper boundary (HAZ/FZ) and (b) the lower boundary (HAZ/FZ) of the EB weld, respectively.

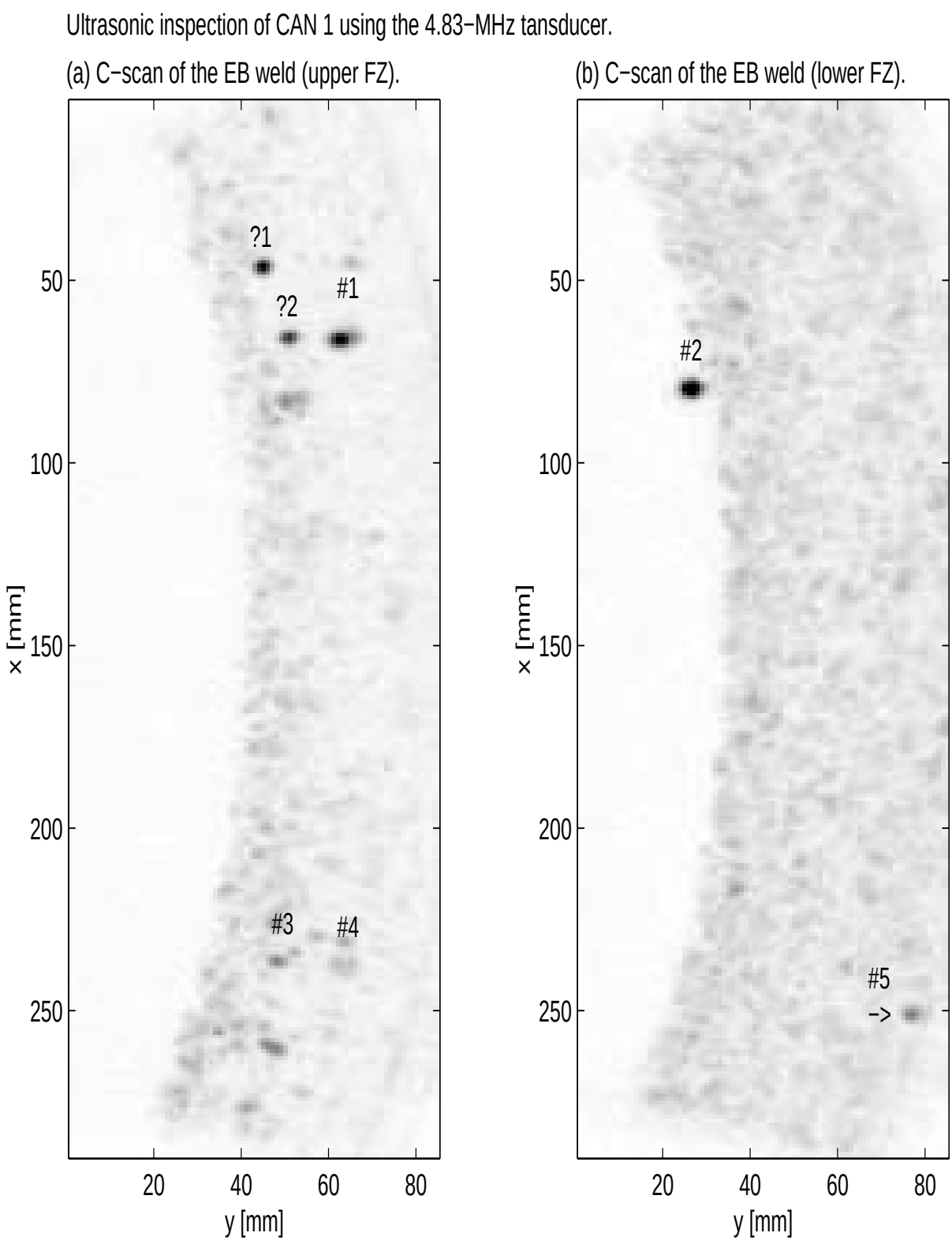

Fig. 1.8. Ultrasonic inspection of copper block W123-3 using the 4.83 transducer. C-scans of copper block W123-3 with the gates located across (a) the upper boundary (HAZ/FZ) and (b) the lower boundary (HAZ/FZ) of the EB weld, respectively.

1.4 Conclusions

Ultrasonic and radiographic inspections of EB welds have been made on two copper specimens, and the inspected results have been compared. The comparison demonstrates that both techniques complement each other very well.

The radiographic technique on the whole gives relatively better spatial resolution but low contrast in the radiographs. This technique can reliably detect voids in EB and the weld structure does not affect results which means that the radiographic inspection cannot provide information about material structure in the EB weld. It should be noted however, that there is a considerable difference in setup between the above presented radiographic inspection and that performed on real canisters. Although the same source and detector were used as for the full-scale inspection, two different views could be obtained for relatively small blocks. This is impossible for the real EB weld and therefore weld image is taken using beams incident at the weld plane at a very small angle, resulting in an unfavorable weld projection.

Ultrasonic technique provides information about flaw locations and shapes similar to that obtained from radiography. Moreover, it can easily distinguish welded and non-welded zones and it can be used to study both macrostructure and microstructure of an EB weld. Structure of EB welds has been studied in our early work [2] and further study has been done recently (see Chapter 2 of this report). Compared to the radiographs, the flaws and defects in ultrasonic images often show high contrast, and some indications may be seen in ultrasonic inspection but not in radiographs, e.g., in the case of specimen W123-3. Small flaws, however, result in indications with amplitudes often close to grain noise pattern, and are, thus, hard to distinguish from the grain noise. This is why the suppression of ultrasonic grain noise is one of our important tasks.

Comparisons of ultrasonic images from two different frequency bands have shown that the images may complement each other because the responses of flaws depend on frequency. The images obtained using larger aperture and lower frequency have shown better spatial resolution than those from the smaller aperture and higher frequency. For an array, this implies that more array elements should be used to form a larger aperture to obtain better spatial resolution. A detail research on the resolution of ALLIN array has been done and reported in [1].

1.5 References

[1] P. Wu, and T. Stepinski, *Inspection of Copper Canisters for Spent Nuclear Fuel by Means of Ultrasonic Array System - Modelling, Defect Detection and Grain Noise Estimation*, SKB Technical Report TR-99-12, July 1998.

[2] T. Stepinski, and P. Wu, *Ultrasonic Inspection of Nuclear Fuel Copper Canisters*, SKB Projektrapport 97-01, December 1996.

[3] T. Stepinski, and P. Wu, *Inspection of Copper Canisters for Spent Nuclear Fuel by Means of Ultrasonic Array System*, SKB Projektrapport 97-06, Augusti 1997.

[4] P. Wu, and T. Stepinski, *Inspection of Copper Canisters for Spent Nuclear Fuel by Means of Ultrasonic Array System – Electron Beam Evaluation, Modelling and Materials Characterization*, SKB Technical Report, July 1999.

2 Electron Beam Weld Evaluation

2.1 Introduction

Evaluation of electron beam (EB) welds is of great importance for developing ultrasonic methods capable of detecting flaws in the weld. A number of contributions to this task have been presented during the past years [1-4]. Research presented here addresses the following issues:

(i) ultrasonic properties of EB weld, like sound velocity, scattering and attenuation,

(ii) harmonic imaging of EB welds,

(iii) grain noise suppression and flaw detection enhancement.

Motivation for the above listed issues results from the following needs:

(i) to gain deeper insight into generation of elastic waves (backscattering) from welds and flaws in order to investigate features significant for the welds and flaws from the viewpoint of physical acoustics,

(ii) to extend the ultrasonic imaging technology used in nondestructive evaluation (NDE) with nonlinear methods,

(iii) to further investigate methods capable of suppressing backscattering from weld zone resulting in increasing the probability of detecting flaws.

A comprehensive review of our research dealing with EB weld evaluation until 1998 was given in the last year's report [4]. During the year of 1998/1999 an extensive, systematical investigation of EB welds had been made, concerned with analyzing the microstructure of EB welds, examining ultrasonic interactions with the welds from ultrasonic data, and ultrasonic imaging of the welds [4]. The relevant ultrasonic properties of EB welds, including reflection and scattering from the EB weld, have been studied. ALLIN ultrasonic array has been extensively used in this research mainly for investigating the feasibility of ultrasonic array technique for detecting defects and flaws in EB welds and developing various methods for improving defects detectability. From ultrasonic imaging of an EB welded copper canister, a layered structure of the weld could be seen consisting of a fusion zone (FZ) surrounded by a heat-affected zone (HAZ). In each zone (the HAZ, the FZ and the host material zone) a different grain noise pattern could be observed, which indicates difference in their microstructure. In the present work ultrasonic properties of EB welds and host material, such as, ultrasonic velocity, attenuation and reflectivity have been further investigated in order to gain deeper insight into the mechanism of formation of ultrasonic signals from the welds and defects. Result of this study will be presented in Sect. 2.2.

To extend the area of the existing ultrasonic imaging in NDE, we have developed two harmonic imaging techniques. The first undertakes imaging using harmonic components due to higher order

resonant modes of an ultrasonic transducer excited with a broadband pulse. The second one realizes imaging by means of nonlinear propagation of finite-amplitude waves. Preliminary results concerning both techniques are presented in Sect. 2.3.

Grain noise is still one of the main barriers to detection of flaws. The development of techniques for grain noise suppression, which has been done using various methods these past years [1-4], is further conducted by exploiting signal processing methods, such as, matched filters and deconvolution. Flaw detection can also be improved by using directly those flaw features that are different from features of grain noise and structural noise of EB welds. These issues will be addressed in Sect. 2.4.

2.2 Ultrasonic properties of EB welds

Electron beam (EB) welding is a fusion welding process using energy of a beam of high-speed electrons on the metal to weld metals [5,6]. Because of the high power and heat concentration of an EB, the fused zone of an EB weld is narrow and the heat-affected zone is very small, and thus both metallurgical damage and distortion are low [5,7]. An EB weld, in general, consists of a fusion zone (FZ) and a heat-affected zone (HAZ) (see Fig. 2.1). The microstructure (e.g., grain size and elasticity) in the fusion and heat-affected zones are differ depending on the amount of heat developed. Therefore, a copper canister with an EB weld is a layered medium in which the EB weld is an embedded multiple layer. This multiple layered structure can be seen by means of ultrasonic imaging when an EB weld is inspected using an ultrasonic beam whose axis is perpendicular to the weld axis (see Fig. 2.1) [4]. The ultrasonic grain noise patterns in the FZ, HAZ and the host material are shown to be different because different grain sizes in the layers result in different scattering effects. The variation of grain size with depth in a copper canister is schematically shown in Fig. 2.2. In the present work we will study other ultrasonic properties of EB welds, namely, scattering, velocity and attenuation.

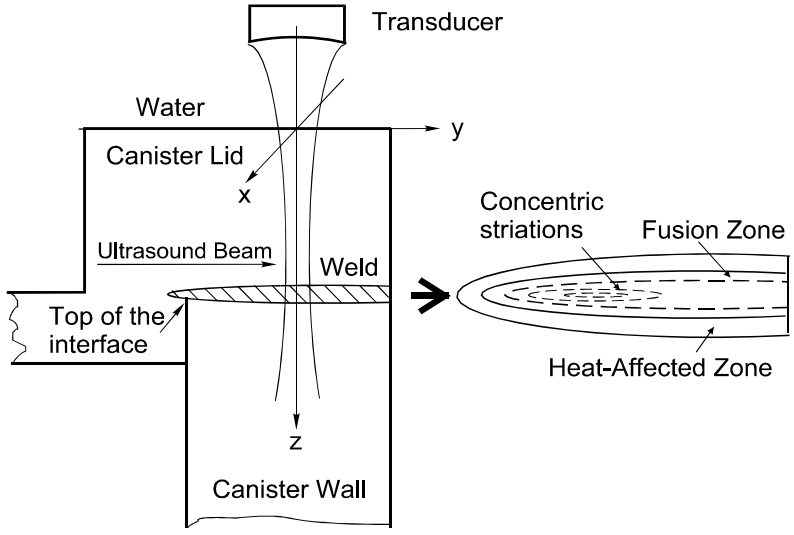

Fig. 2.1. Schematic of EB weld structure and of ultrasonic inspection of the EB weld.

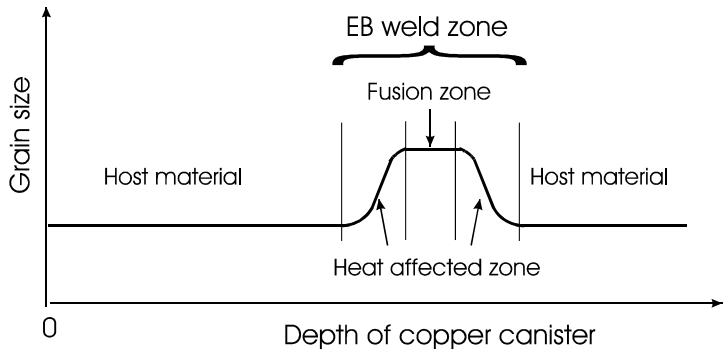

Fig. 2.2. Schematic plot showing the variation of grain size as a function of depth in a copper canister with an EB weld.

2.2.1 Experimental setup and measurements

The experimental setup used for this study is the same as presented in the previous chapter (Fig. 1.2), that is, the two-element annular transducer array is used with the ALLIN ultrasonic array system. The copper block inspected was CAN 1 (see Fig. 1.1). The conditions used for the measurements are almost the same as in the previous chapter. The difference in the present study is in the inspected regions of interest. Referring to Fig. 1.1, the horizontal and vertical directions are assumed to be the *x* and *y* directions, respectively. The region of interest selected and mechanically scanned is an area of 40x65 mm including flat bottom holes (FBH) #5 and #14 that are in and out of the EB weld zone, respectively (see Fig. 1.1). The scanning intervals in the *x* and *y* directions are 1.0 and 0.5 mm, respectively. Under these measurement conditions, 3-dimentional data were acquired. From these data C-scans were extracted by taking the absolute maximum values of echoes in the properly selected time gates, and the B- and A-scans of interest can be located from the C-scans. Note that the B- and A-scans in this report are displayed in such a way that the vertical axis is *y* (one scanning direction) and the horizontal is *z* (the depth). This implies that the transducers are positioned on the left-hand side of images. For examining ultrasonic scattering from EB weld, described in the next section (Sect. 2.2.2), we used the two-element annular array transducer, and also the third one, Panametrics V315. The latter one had nominal center frequency of 10 MHz, but a measured center frequency of 8.65 MHz and the measured –6 dB bandwidth of 82%.

Since C-scans provide an overall, top view of an inspected sample, the above selected regions of interest can be seen from the C-scans. The ultrasonic images of CAN 1 using the 2.26- and 4.83-MHz transducers are shown in Figs. 2.3 and 2.4, respectively, in the form of C-scans. The C-scans in panels (a), (b) and (c) of these two figures show the specimen front surface, the EB weld, and the back

surface, respectively. Note that different gains (see Table 2.1) were used to make these measurements from which the C-scans are constructed.

Table 2.1. Gains (dB) used in the measurements for the front surface, EB weld, and back surface.

	Gains (dB) used for		
	Front surface	EB weld	back surface
2.26 MHz transducer	0	13	22
4.83 MHz transducer	0	10	25

2.2.2 Ultrasonic scattering of EB welds and their imaging

In our previous work [4], ultrasonic scattering from EB welds had been investigated using the ALLIN array having a 3.1-MHz center frequency and a 58% bandwidth, and the investigation was undertaken within this limited frequency range. Inspection of EB welds over a wider frequency range may enable obtaining more information on the welds. For example, attenuation in EB welds varies with frequency and thus the investigation over a wider frequency range may supply more complete picture of the attenuation. It is well known that an EB weld has HAZ and FZ zones and the grains in each zone are different in size and elasticity (related to sound velocity). Usually, fine grain structure is difficult to see at low frequency but easier at high frequency. The grains in the HAZ of an EB weld are much smaller than in the FZ. Therefore, using high frequency ultrasound may result in better ultrasonic imaging of the HAZ.

Since C-scans are obtained from the absolute maximum values of echoes in the properly selected time gates, they reflect the dynamic range of echo strengths. Let us look more carefully at the C-scans of the front surface, EB weld and back surface.

Figs. 2.3(a) and 2.4(a) show the C-scans of the front surface of CAN 1 from the 2.26- and 4.83-MHz transducers, respectively. From the figures it can be seen in both cases that the echoes from the front surface vary in small ranges, namely 91~114 (or $103.3^{+10\%}_{-12\%}$) and 96~118 (or $107.6^{+9\%}_{-10\%}$). The C-scans containing the EB weld zone are shown in Figs. 2.3(b) and 2.4(b). Since the strong echoes from FBH #15 are displayed in full, unsaturated waveform the weld zone is only weakly pronounced in the upper parts of the figures. The C-scans of the back surface (in Figs. 2.3(c) and 2.4(c)) show that the echoes coming through the weld (the upper parts in light blue) are much weaker than those not coming across the weld (the lower parts in red). This can be more easily demonstrated using the profiles of the C-scans along the *y*-direction. An example is shown in Fig. 2.5 in which the normalized profiles are displayed at x= 6 mm of the C-scans in Figs. 2.3(c) and 2.4(c). Note that in Fig. 2.5 the vertical axis is the *y*-axis and the horizontal axis is the amplitude.

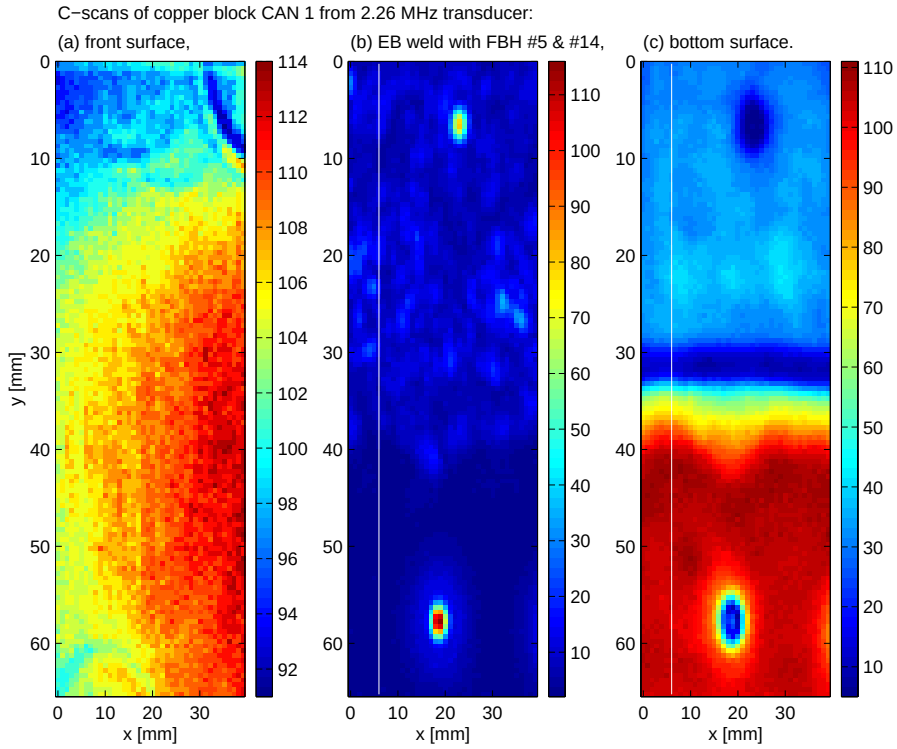

Fig. 2.3. C-scans of copper block CAN 1 by means of 2.26 MHz annular transducer with spherical focus (radius of curvature of 210 mm). (a) Front surface, (b) EB weld, and (c) back surface.

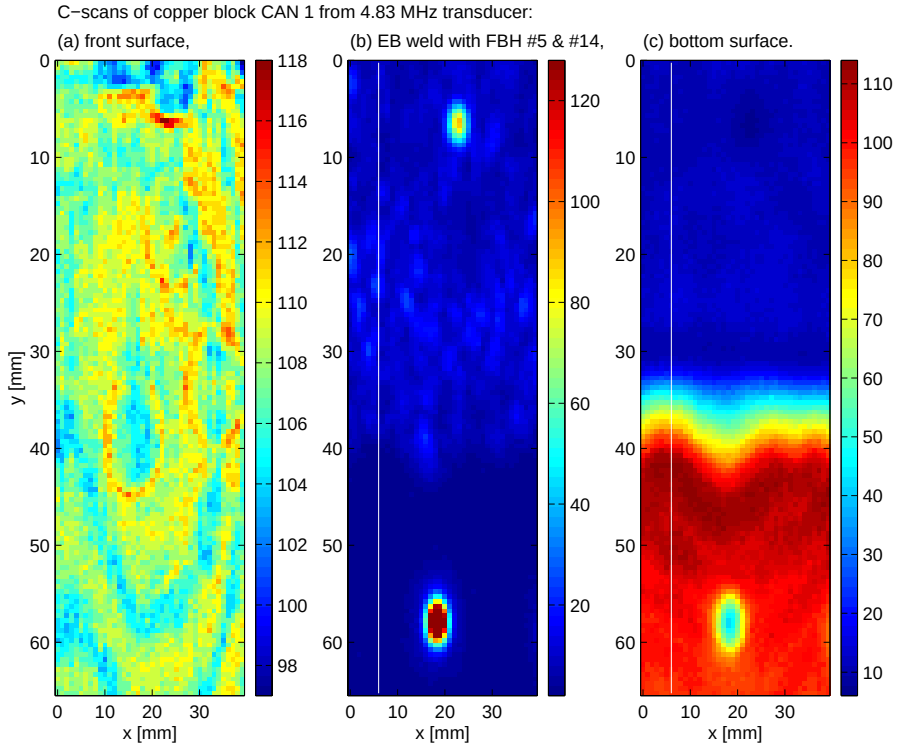

Fig. 2.4. C-scans of copper block CAN 1 by means of 4.83 MHz circular transducer with spherical focus (radius of curvature of 210 mm). (a) Front surface, (b) EB weld, and (c) back surface.

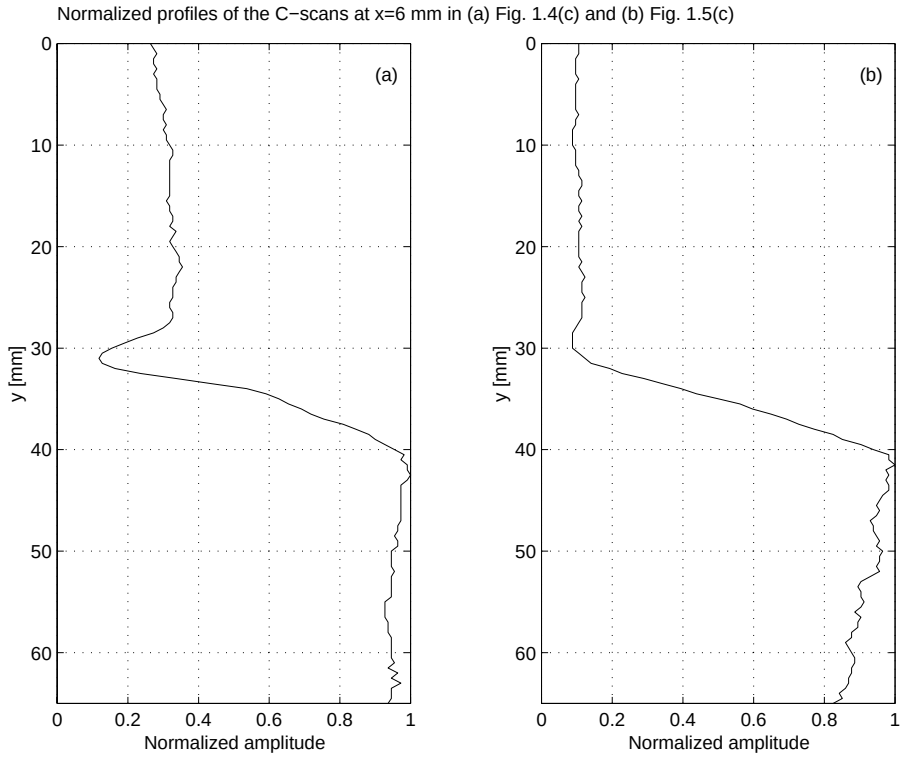

Fig. 2.5. The normalized profiles of the C-scans at *x*=6 mm in (a) Fig. 2.3(c) and (b) Fig. 2.4(c).

The big difference of the echoes coming through and not coming across the weld results from both the reflection and attenuation loss of the EB weld. Comparison of the normalized profiles in Figs. 2.5(a) and (b) also shows that the back surface echoes are less attenuated for the 2.26-MHz transducer than for the 4.83-MHz transducer. More discussion on attenuation will be given below. From images of the FBHs in Figs. 2.3(b) and 2.4(b) it can be seen that in the EB weld zone the spatial resolution for the 2.26-MHz element is better than for the 4.83-MHz element. This is because the aperture dimension of the former element, although having a lower center frequency, is much larger than the latter one. This implies that for a better spatial resolution a larger aperture is needed, as observed in Chap. 1 of the report.

As we have seen, C-scans yield an overall, top view of an EB weld and the dynamic range of scattered echoes. To examine the structure of an EB weld, the cross-sectional view that is shown in B-scan is helpful. To the purpose, we used the three transducers with center frequencies of 2.26, 4.83 and 8.65 MHz. The first two transducers are the separate elements of the two-element annular array transducer used in the previous section, and the third one used is Panametrics V315 with a measured center frequency of 8.65 MHz. The transducers were used with the ALLIN system in the similar way as shown in Fig. 1.2. The B-scans from those three transducers are shown in Fig. 2.6(a), (b) and (c), respectively. Vertical axis in Fig. 2.6 is the scanning position y and the horizontal axis is $z\text{-}z_0$ (where

z_0 is the path length of the water layer), the depth in the copper block. Note that logarithmic scale of the signal envelope in these images used to highlight the weak scattering from the HAZ.

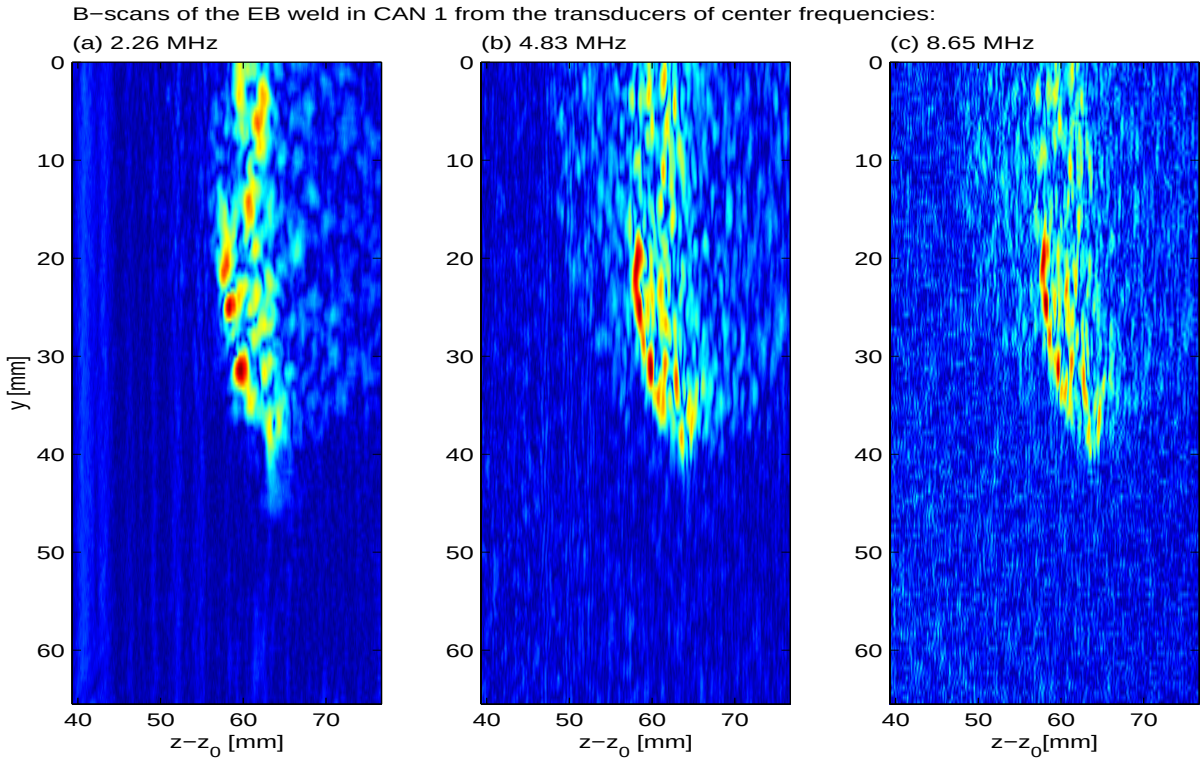

Fig. 2.6. B-scans of the EB weld in CAN 1 form the transducers with three different center frequencies: (a) 2.26 MHz, (b) 4-83 MHz, and (c) 8.65 MHz. Here z_0 is the water path length. The scans are located at *x*=6 mm in Figs. 2.3 (b) and 2.4 (b).

From these B-scans we can examine the cross-section of the EB weld. The tip of the weld is located around *y*=42 mm, *z*- z_0 =60. In each image a strip-like strong echo zone is seen that indicates the FZ within the region of *y*=0~42 mm, *z*- z_0 =56~64 mm. In the B-scan from the 2.26-MHz transducer the HAZ is very difficult to see. But the HAZ is easy to see in the B-scan from the 4.83-MHz transducer as well as the 8.65-MHz transducers (however, for the 8.65-MHz transducers the grain noise from the host material is more apparent and the electronic noise becomes larger as well). The reason for this is that the fine grains (in the HAZ) result in less scattering to the low frequency ultrasound than to the higher frequency one. In other words, the higher frequency ultrasound is more sensitive to fine grains. From Fig. 2.6(b), the thickness of the HAZ can be measured to be around 8 mm (from 48~56 mm in the *z* direction) in front of the EB weld. Therefore, to inspect the HAZ of an EB weld, a transducer with higher frequency, e.g., 5 MHz, may be a good choice (if the EB welding process is made under normal conditions). To inspect the FZ, the transducer with lower frequency, e.g., 2~3 MHz (from the

present and the early research [4]), can be a better choice. Combination of the inspections in the two frequency bands will give us more information on EB welds.

2.2.3 Sound velocity

Sound velocity in an EB weld is ultrasonic parameter related with its elastic constants. Since an EB weld is a layered medium consisting of the HAZ and the FZ and embedded in its host material, the sound velocities in the HAZ and FZ are different. It is difficult to estimate the velocity in each zone. But it is possible to estimate the average velocity over the whole weld. To this purpose, B-scans as well as A-scans in the B-scans are used. The B-scans come from the measurements presented in Sect. 2.2.1. To facilitate the velocity estimation, the B-scans of the block front surface and the corresponding back surface are selected, and shown respectively in panels (a) and (b) in Fig. 2.7 (from the 2.26 MHz transducer) and Fig. 2.8 (from the 4.83 MHz transducer). For the sake of easy observation, the B-scans are shown only in negative half wave. The B-scans of the front surface in Figs. 2.7(a) and 2.8(a) is used as a reference. The straight stripes in the scans reveal that the echoes from the front surface at all scanning positions have almost the same phase fronts and the same frequency bands. Looking at the B-scans from the back surface (Figs. 2.7(b) and 2.8(b)), we can see two different regions. In the upper part (y=0~30 mm) where the EB weld is located, the stripes look rather straight and parallel. This may demonstrate that the back surface echoes coming back through the EB weld have quite similar phase fronts, in other words, the sound speed in the weld zone is almost position independent. In contrast, in the lower part (y=35~65 mm) that is out of the weld zone, the stripes become bent towards the right hand side (the later times). This means that the phase fronts of the echoes coming back through the non-welded zone vary with position, namely, the farther away from the weld (the larger the y coordinate) the later the echoes come back. In other words, the sound speed seems to vary with position and the farther away from the weld (the larger the y coordinate) the lower the sound speed. The reason for this might be the gradient variation of heat effect of EB welding on a host material, which in turn results in different microstructure (e.g., grain size and elasticity) in the host material. As far as we could see this effect cannot be explained by a variable block hight.

Comparing an A-scan coming back through the weld with an A-scan in the non-welded zone, e.g., at x=6 mm and y=66 mm, we may find that their time difference is -0.16 microsecond for the 2.26-MHz transducer case and -0.19 microsecond for the 4.83-MHz transducer case, respectively. This may be explained by the fact that the sound speed in the EB weld is higher than in the parent material, and that there exists a speed variation in the non-welded zone. From the measured thickness of the HAZ (approximately 8 mm on one side) and of FZ (approximately 8 mm), we may have the approximate thickness of 24 mm for the whole EB weld including the two side HAZ and the FZ. Assuming that parent material, used both for lock and walls of the copper canister has a sound velocity of 4596 m/s

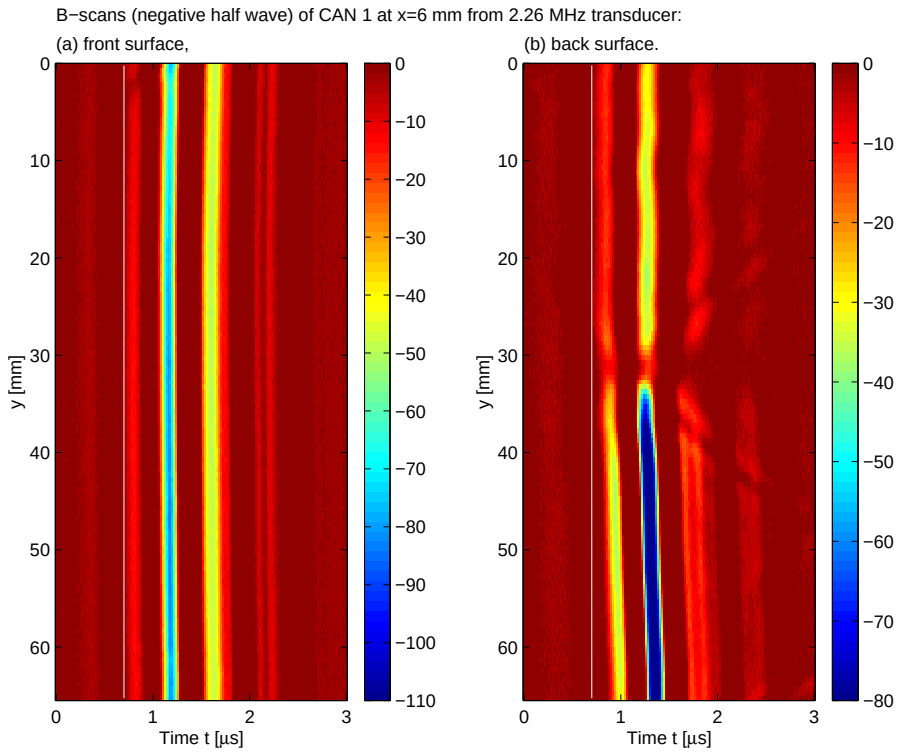

Fig. 2.7. B-scans of copper block CAN 1 from 2.26 MHz annular transducer with spherical focus (radius of curvature of 210 mm). (a) Front and (b) back surface at *x*=6 mm in Fig. 2.2.

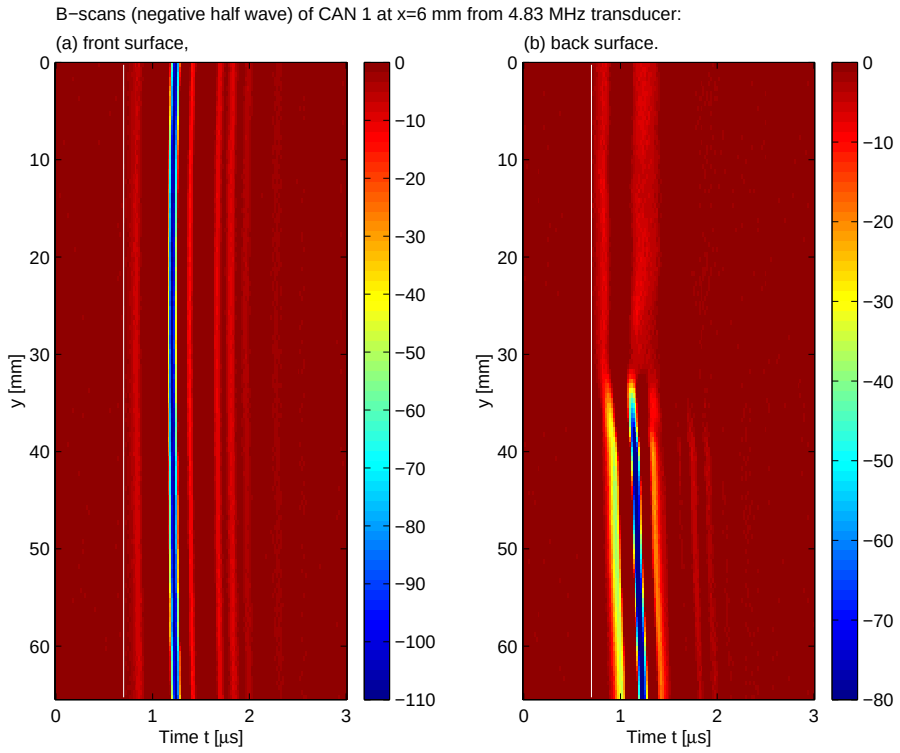

Fig. 2.8. B-scans of copper block CAN 1 from 4.83 MHz circular transducer with spherical focus (radius of curvature of 210 mm). (a) Front and (b) back surface at *x*=6 mm in Fig. 2.3.

and taking the average time difference of -0.175 microsecond, we obtain the average sound velocity in the EB weld approx. 4674 m/s, which is 1.7% higher than that of its host material. The velocity is obtained from the following relation,

$$V_w = 1 \Big/ \left(\frac{1}{V_c} - \frac{\Delta t}{2D_w} \right),$$

where V_w and V_c are the sound velocities in the weld and the copper block without welding, D_w is the weld thickness, and Δt is the time difference between the two same copper blocks, one being welded and the other being not.

From Figs. 2.7 and 2.8 appears that the sound velocity in the non-welded zone at a position closer to the EB weld (closer to HAZ, e.g., at y=50 mm) will differ less. Difference and variation of sound velocities result in beam deflection. The greater difference of the sound velocities between the HAZ and the FZ results in better-pronounced beam refraction as well as reflection at the boundary between the HAZ and FZ.

2.2.4 Sound attenuation

Higher attenuation of ultrasound by an EB weld has been observed in the previous section (Sect. 2.2.2). Examining the separations of the stripes in the B-scans in Fig. 2.7(b) and 2.8(b), we can see that the separations in the lower part are smaller than in the upper part (especially in the case of the 4.83-MHz transducer, c.f., Fig. 2.8(b)). It means that the echoes coming back through the non-welded zone are of higher frequency than those being back through the EB weld. In other words, the EB weld is more attenuative.

To quantitatively estimate the attenuation of EB weld is not an easy task. The microstructures in the HAZ and FZ are different and inhomogeneous so that the ultrasonic properties (including sound speed) may be different, and the boundaries between the host material and HAZ and between the HAZ and FZ are not clearly defined (see Fig. 2.2). For example, grain size in an EB-welded copper canister may vary with positions in the host material, the HAZ and the FZ. Thus the thickness of each zone is difficult to accurately measure.

However, it is possible to observe and estimate the excess attenuation of EB weld by looking at the center frequency difference of the spectra of two echoes, one coming back through the EB weld and the other through the non-welded zone. Figs. 2.10 and 2.11 show such a comparison for the 2.26- and 4.83-MHz transducers, respectively. The center frequency differences for two cases are 0.44 and 2.33 MHz, respectively, that correspond to 19% and 48% relative to the center frequency of the transducers, respectively. Obviously, the excess attenuation for the 4.83-MHz transducer is much

larger. More accurate estimation of the excess attenuation can be made using the log spectral difference method. Taking the difference of the natural logarithms of the amplitude spectra of two back echoes in Figs. 2.10(a) and 2.11(a), respectively, (shown in Figs. 2.10(c) and 2.11(c)), we can see for each case a region (1 to 4.5 MHz in Fig. 2.10(c) and 1 to 6.5 MHz in Fig. 2.11(c)) in which the amplitude vary with frequency quite linearly. For each case, we find a fitting line over the linear variation region, that is, $Ad_{\ln} = 0.92 f - 0.9$ for the 2.26-MHz transducer and $Ad_{\ln} = 0.92 f - 0.95$ for the 4.83-MHz transducer. Both lines have the same slope 0.92 that will be used for attenuation estimation.

Denoting α_c and α_{cw} to be the attenuation coefficients of the copper block without and with an EB weld, respectively, and α_w the attenuation of the EB weld including the reflection loss, and D is the block thickness, D_w the EB weld thickness, we may have the following approximate relation

$$\alpha_{cw} \cdot 2D = \alpha_w \cdot 2D_w + \alpha_c \cdot 2(D - D_w)$$

that holds for the plane wave case, and from this equation, we can find the relation for calculuating the excess attenuation of EB weld,

$$\Delta\alpha = \alpha_w - \alpha_c = (\alpha_{cw} - \alpha_c) \cdot D / D_w .$$

Here $\alpha_{cw} - \alpha_c$ can be found from the slopes of the fitting lines for the log spectral differences, that is, $\alpha_{cw} - \alpha_c = 0.92/(2D)$ in the unit of $\text{Np/(MHz} \cdot \text{mm)}$. Considering the present case where the block thickness, D=79 mm, and the EB weld thickness, approximately D_w=10 mm (c.f., [8]), the excess attenuation of EB weld can be found,

$$\Delta\alpha = \alpha_w - \alpha_c = 0.0458 \text{ Np/(MHz} \cdot \text{mm)} = 0.3997 \text{ dB/(MHz} \cdot \text{mm)} .$$

For example, at 5 MHz, the excess attenuation is 1.9985 dB/mm, which can be more ten times larger than that of a pure copper block with fine grains (e.g., 0.15 dB/mm at 5 MHz).

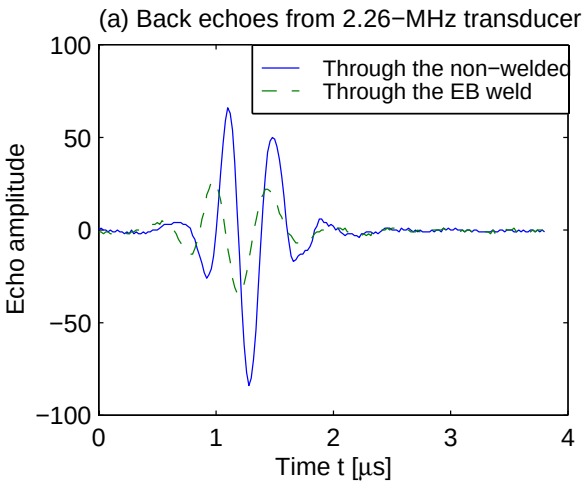

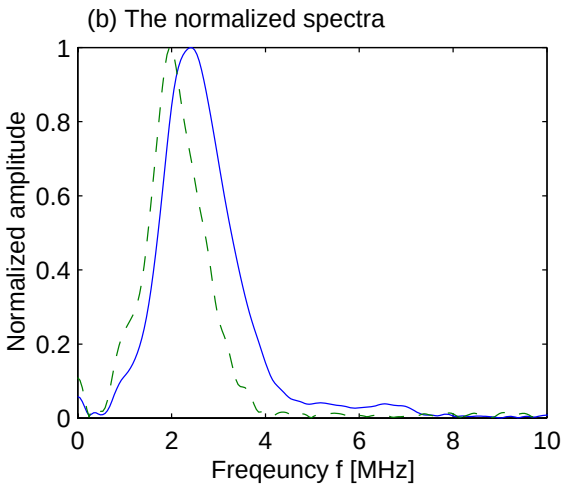

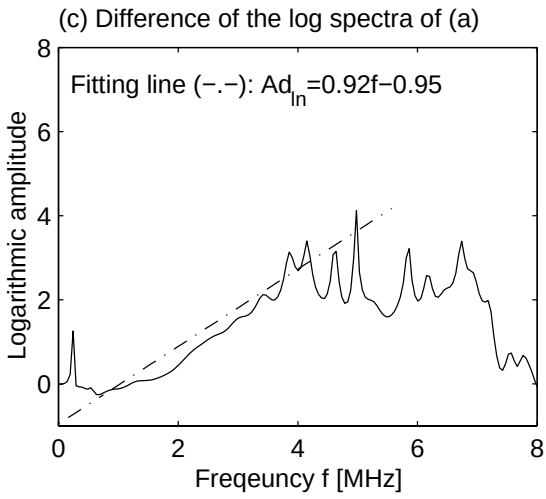

Fig. 2.10. (a) Back echoes from the 2.26-MHz transducer, (b) their normalized spectra, and (c) the difference of their log spectra.

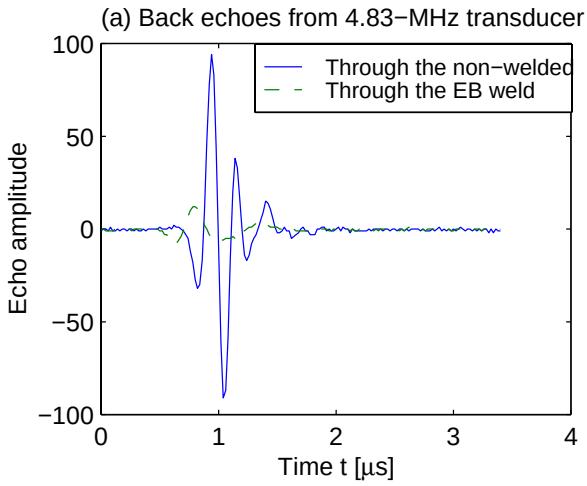

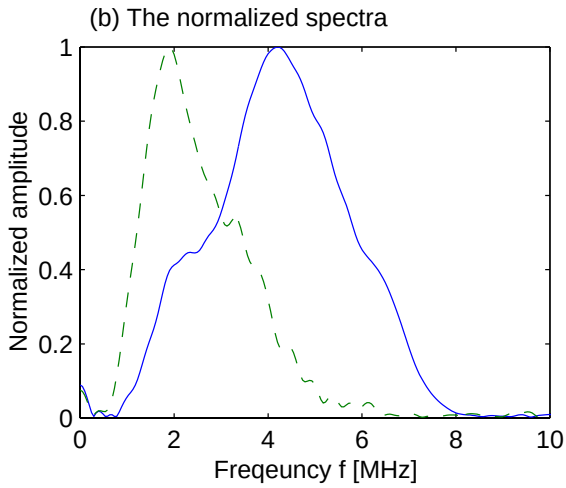

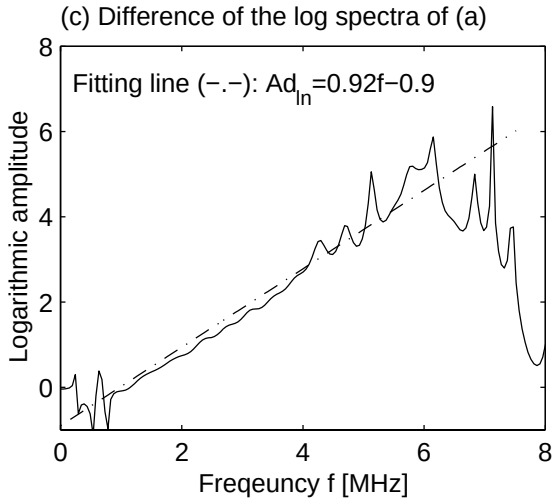

Fig. 2.11. (a) Back echoes from the 4.83-MHz transducer, (b) their normalized spectra, and (c) the difference of their log spectra.

2.2.5. Ultrasonic properties - Summary

The ultrasound generated by the 2.26-MHz transducer has relatively long wavelength (2 mm at the center frequency for longitudinal wave) resulting in the fact that not much scattering is observed from a fine grain material in HAZ but scattering from fusion zone with coarse grains is clearly visible. Thus, the HAZ shows low contrast and the fusion zone (FZ) shows high contrast in the ultrasonic image so that the FZ structure is highlighted and the layered structure from its front and back surfaces is possible to recognize. The ultrasound from the 4.83-MHz transducer (wavelength nearly 1 mm at the center frequency for longitudinal wave) yields significantly high contrast for HAZ above the FZ although not so high as that observed for the FZ. Therefore, the structure of the HAZ in this case becomes apparent and easier to measure, but the back surface of the FZ becomes difficult to recognize. In both cases, however, the HAZ behind the FZ is immersed in the grain noise from the FZ. The wavelength of 8.65-MHz transducer is relatively short (0.53 mm) and results in a significantly large grain noise from the host material obscuring the HAZ. This implies that the 8.65-MHz ultrasound is too high in frequency to be used for EB welds imaging.

The results from the study of sound velocity in a copper canister with an EB weld have shown that the sound velocity in an EB weld can be 1.7% larger than the same material as the copper canister without welding effect. The sound velocity in the non-welded zone shows a variation with the distance to the EB weld, that is, the closer it becomes to the EB weld's velocity the nearer the position to the weld. The difference of sound velocities in the EB weld and the host material will cause scattering, reflection, and refraction.

The study on ultrasonic attenuation in EB welds reveals that attenuation in an EB weld is much higher than its host material and can be more ten times larger for such copper materials that copper canisters are made of. The studies on scattering and attenuation may suggest that a suitable ultrasound frequency band for evaluating EB welds should be less than 5 MHz.

2.3 Harmonic imaging of EB welds

The harmonic imaging technology has emerged as a major imaging trend in medical ultrasound over the recent years, and resulted in significant improvement in image quality in medical ultrasonic imaging. This technology was initially developed for *contrast* harmonic imaging (also called *contrast agent* harmonic imaging) and later for *tissue* harmonic imaging (also called *native tissue* harmonic imaging). The contrast harmonic imaging is based on the fact that small contrast micro-bubbles radiate significant energy at multiples of the interrogation frequency. The tissue harmonic imaging, on the other hand, exploits the nonlinearities of ultrasound propagation that gradually change the shape of the wave as it passes through tissue, and thus result in the harmonic components. It dramatically reduces near field and side lobe artifacts. Over the past decade, a large amount of work on contrast harmonic

imaging [9-13] and tissue harmonic imaging [14-19] has been done in the medical ultrasonic imaging area. Up to now, this technology has already been equipped in the commercial medical ultrasound systems.

In nondestructive testing, however, this technology has not been applied, although some attempts focused on investigating the nonlinear propagation in water of waves from NDT ultrasonic systems have been made recently, cf. [20-22].

In addition to the two sources above mentioned, there is another source from which harmonic components originate [23]. It is common in ultrasonic NDE that a broadband pulse is applied to excite a transducer having a limited frequency bandwidth. The broadband excitation causes the transducer to vibrate not only in its fundamental resonant mode but also in high order resonant modes. When the transducer is used in pulse-echo mode, the fundamental resonant component in a received signal remains strong but the harmonic components due to the high order resonant modes are filtered out. It means that much information contained in the signals (in higher harmonic components) sent out by a transmitter is lost in pulse-echo mode. If a wide band receiver is employed, the high harmonic components can be captured. These harmonics will be called *transducer harmonics* in the sequel.

It is known from medical ultrasonic imaging that the high harmonics due to the nonlinear propagation of waves can be combined to enhance the signal to noise ratio and the resolution in B-scan images [16]. Using the similar idea we make an attempt to apply such technique to the NDE for improving the quality of ultrasound B-scans acquired in immersion inspection of copper. In addition to the improvement, each of the harmonic components is separated and processed by means of some signal processing method in order to exploit more information on EB welds from received signals.

In our present case where copper canisters are inspected, the second source of harmonics, namely, nonlinear radiation from micro-bubbles, does not exist. Therefore, the harmonics from the other two sources have been dealt with. Especially, the harmonics from the nonlinear propagation of waves in materials has been studied more systematically. By analogy to *tissue harmonics*, these harmonics will be called *material harmonics* in the sequel.

The overall purpose of the research on harmonic imaging is to expand the existing space of ultrasonic imaging technology used in nondestructive evaluation (NDE) and to explore more information on materials and defects that may be contained in harmonics. The goals of the present work is rather general, firstly, to make the best use of information (including transducer harmonics) contained in ultrasonic signals received by wide band receivers. Secondly, to investigate experimentally the nonlinear phenomenon of elastic wave propagation in solids, and thirdly, to show the possibility of applying the harmonic imaging technology to the NDT.

2.3.1 Harmonic imaging using transducer harmonics

Let us begin with studying *transducer harmonic imaging*, named after the fact of employing transducer harmonics, namely harmonic components from the high order resonant modes of transducers, to construct images. This study had two particular aims: investigating the feasibility of basic harmonic imaging technique, and developing a signal processing technique for improving the signal to noise ratio.

2.3.1.1 Experimental study

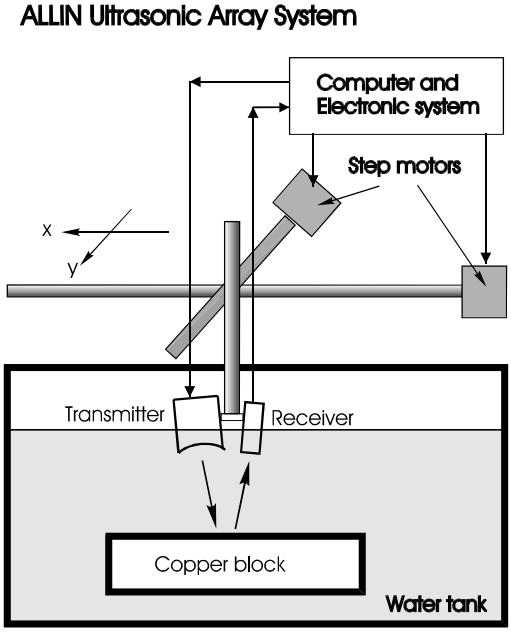

Fig. 2.12. Experimental setup for transducer harmonic imaging.

The experimental setup used for this study is shown in Fig. 2.12. The transmitter used was a broadband, spherically focused transducer (PANAMETRICS V392) that had a 0.85-MHz center frequency (measured), an 87% –6-dB bandwidth (although relative bandwidth was broad, the absolute bandwidth was not due to the low center frequency), a 38-mm diameter, and a 190-mm focal length. The receivers respectively used with the transmitter were four broadband planar transducers (PANAMETRICS V325, V383, V326 and V327) that had nominal center frequencies of 2.25, 3.5, 5, and 10 MHz, respectively, and the measured frequencies were 2.25, 3.4, 4.7, and 7 MHz, respectively. The transmitter/receiver pairs used in the experiments will be denoted 1/2.25, 1/3.5, 1/5 and 1/7 MHz, respectively. Copper block CAN 1, containing an EB weld, and a set of side-drilled holes (SDH) and bottom-drilled holes (SDH) (see Fig. 1.1) has been inspected with each of the above mentioned transmitter/receiver pair. 3-dimensional RF data that can be used to create the A-, B- and C- scans of the copper block has been acquired has been acquired for each pair. An example is shown in Fig. 2.13 in which the C-, B- and A-scan come from the measurement made on copper block CAN 1 using the

1-MHz focused transmitter and the 7-MHz planar receiver (1/7 pair). The C-scan in (a) was obtained using the gate selecting the whole EB weld. The B-scan in (b) shows the cross-sectional view at *y*=72 mm in the C-scan. The A-scan in (c) is at *x*=56 mm in the B-scan, and the echo comes from the side-drilled hole, SDH No. 11.

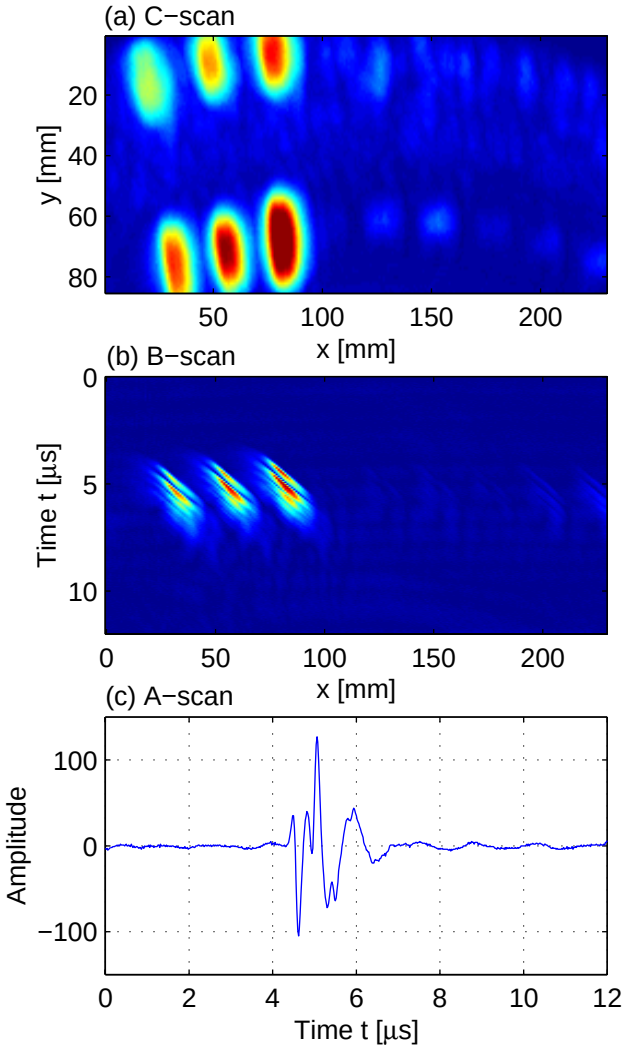

Fig. 2.13. C-, B- and A-scan from the measurement made on the copper block using the 1-MHz focused transmitter and 7-MHz planar receiver. (a) C-scan, (b) B-scan at y=72 mm, and (c) A-scan at x=56 mm and y=72 mm that comes from the side-drilled hole, SDH #11.

To investigate transducer harmonics, let us examine the echoes from SDH #11 for all the transmitter/receiver pairs, and their spectra, which are shown in Fig. 2.14. In this figure we can see that for the 1/2.25, 1/3.5, 1/5, and 1/7-MHz pairs the harmonic components are visible up to the 2nd, 3rd, 4th, and 4th, respectively. This demonstrates that the frequency range of a received signal is much wider than that when the transmitter is used in pulse echo mode.

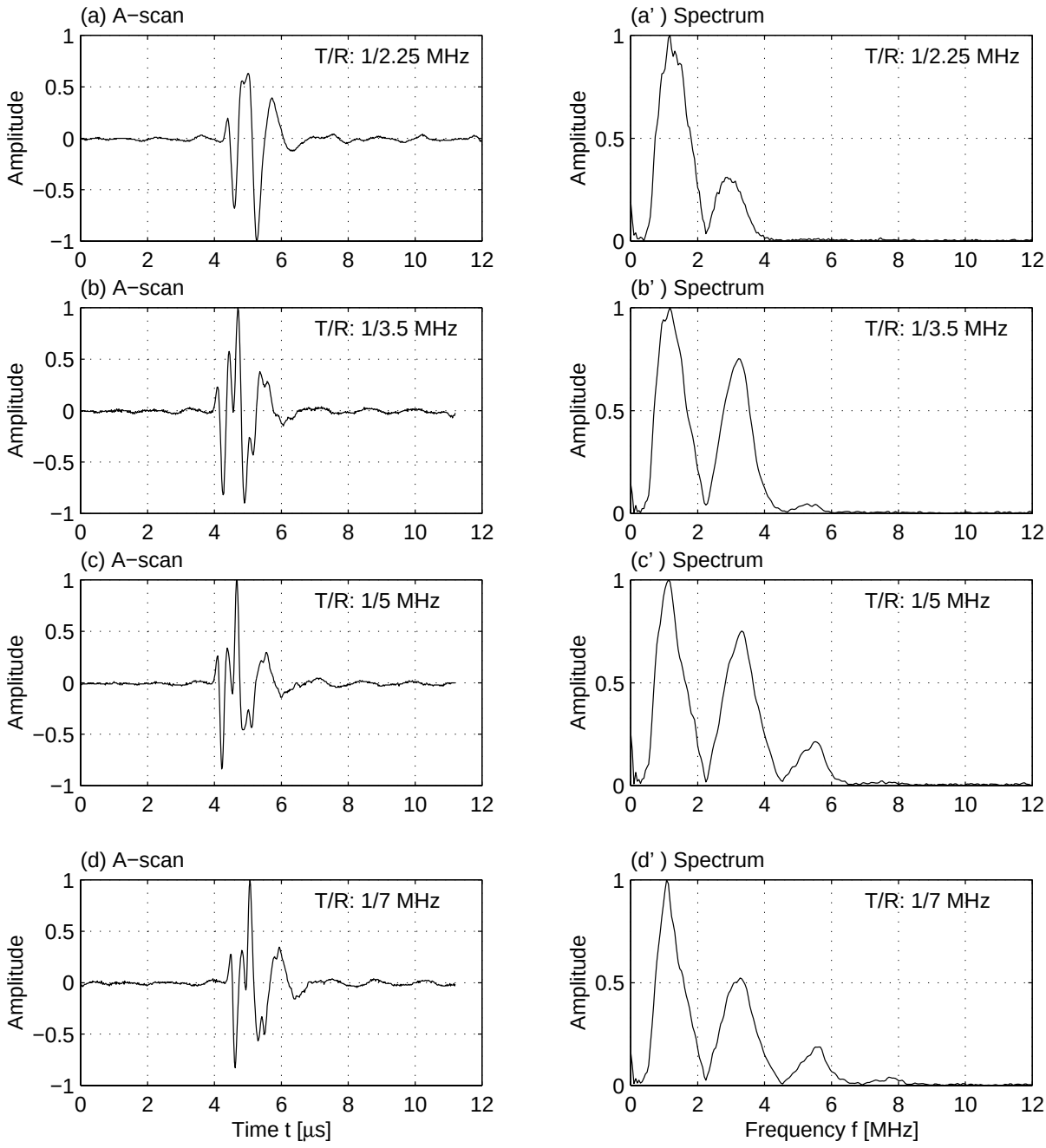

Fig. 2.14. Pulse echoes (a) – (d) from the side-drilled hole, SDH No. 11, obtained using the transmitter and receiver pairs (T/R): 1/2.25 MHz, 1/3.5 MHz 1/5 MHz, and 1/7 MHz, respectively, and their corresponding spectra (a') – (d').

It is worth noting that although the captured harmonic components may contain some material harmonics, the latter ones are small in this case, which will be explained in Sect. 2.3.2. Using Hanning window for filtering the spectra, each harmonic component can be extracted. The four harmonics extracted for 1/7-MHz pair are shown in the form of A-, B- and C-scan, respectively in Figs. 2.15-2.17. The four waves in the A-scan form (Fig. 2.15) would have similar time duration if the noise could be removed. The observation shows that the fundamental component has the largest signal-to-

noise ratio (SNR), whereas the fourth harmonic has the lowest SNR. From the harmonic B- and C-scans in Figs. 2.16 and 2.17, we can see that the higher order the harmonic the better the spatial resolution, but the larger the electronic noise. Note that A-scan envelopes are shown in B-scans. If the four harmonic B-, or C-scans are compounded (averaged), the grain noise can be reduced in the way similar to the frequency diversity method (c.f. [3, 4]).

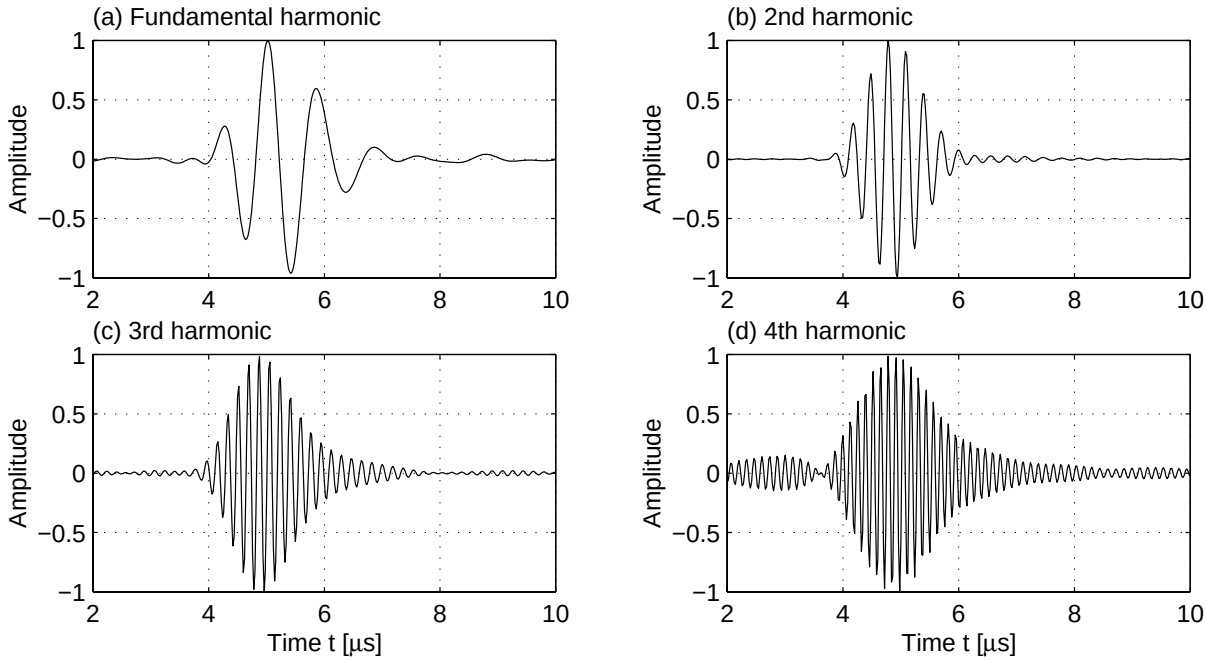

Fig. 2.15. A-scans (a)– (d) constructed from the fundamental to the forth components, respectively, in the case of using the transmitter and receiver pair, T/R: 1/7 MHz.

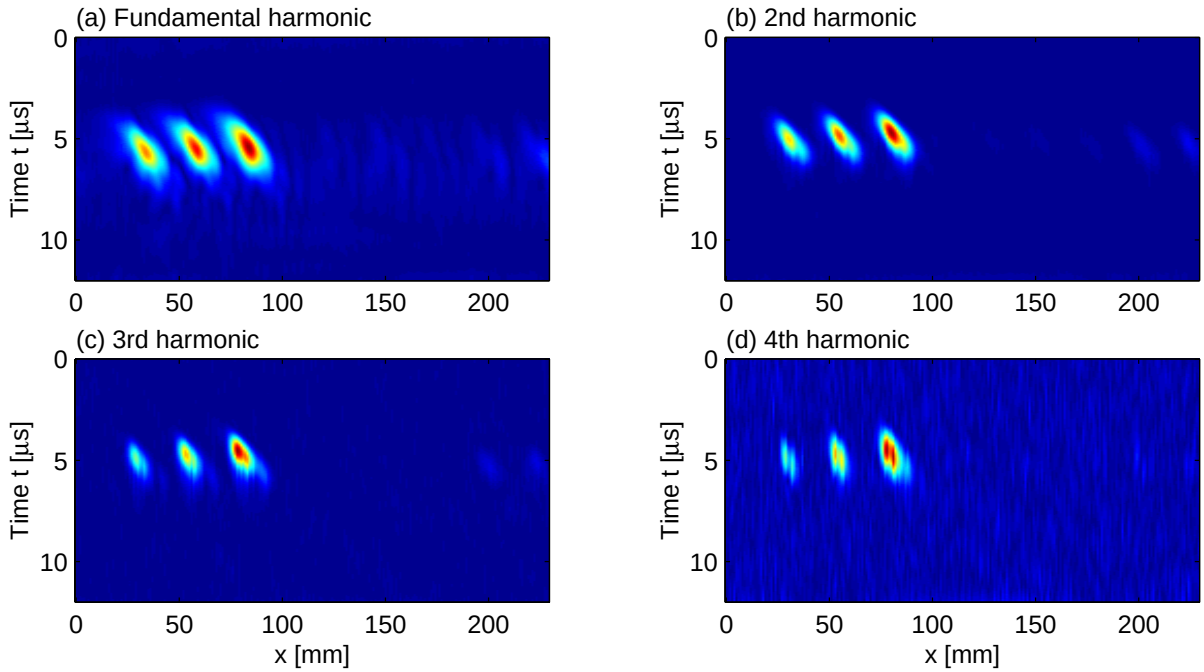

Fig. 2.16. B-scans (a)– (d) constructed from the fundamental to the forth components, respectively, in the case of using the transmitter and receiver pair, T/R: 1/7 MHz.

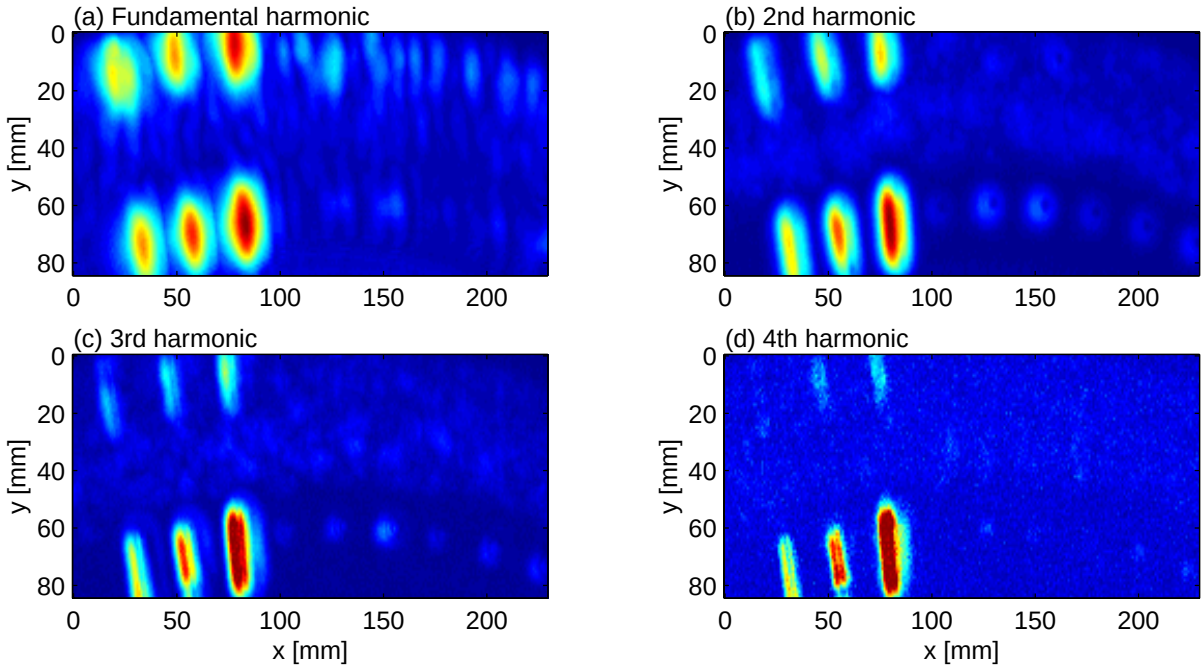

Fig. 2.17. C-scans (a)– (d) constructed from the fundamental to the forth components, respectively, in the case of using the transmitter and receiver pair, T/R: 1/7 MHz.

2.3.1.2 Signal processing using 2-D matched filter

Below the C-scans obtained from different harmonic components before and after 2-D matching filtering are compared (see also Section 2.4.4). The harmonic extraction was performed by filtering A-scans in frequency domain using rectangular windows.

The envelope of A-scan calculated using Hilbert transform was used for C-scan extraction. The 2-D matching filtering was performed for all B-scans used for the extraction of C-scans. The extracted C-scans from the full frequency data for whole block CAN1 are presented in Fig. 2.18. In this figure the C-scan presented in the left column was obtained from the A-scans processed by the described above band-pass filters, while the C-scan shown on the right column was extracted from the data processed by 2-D matched filter.

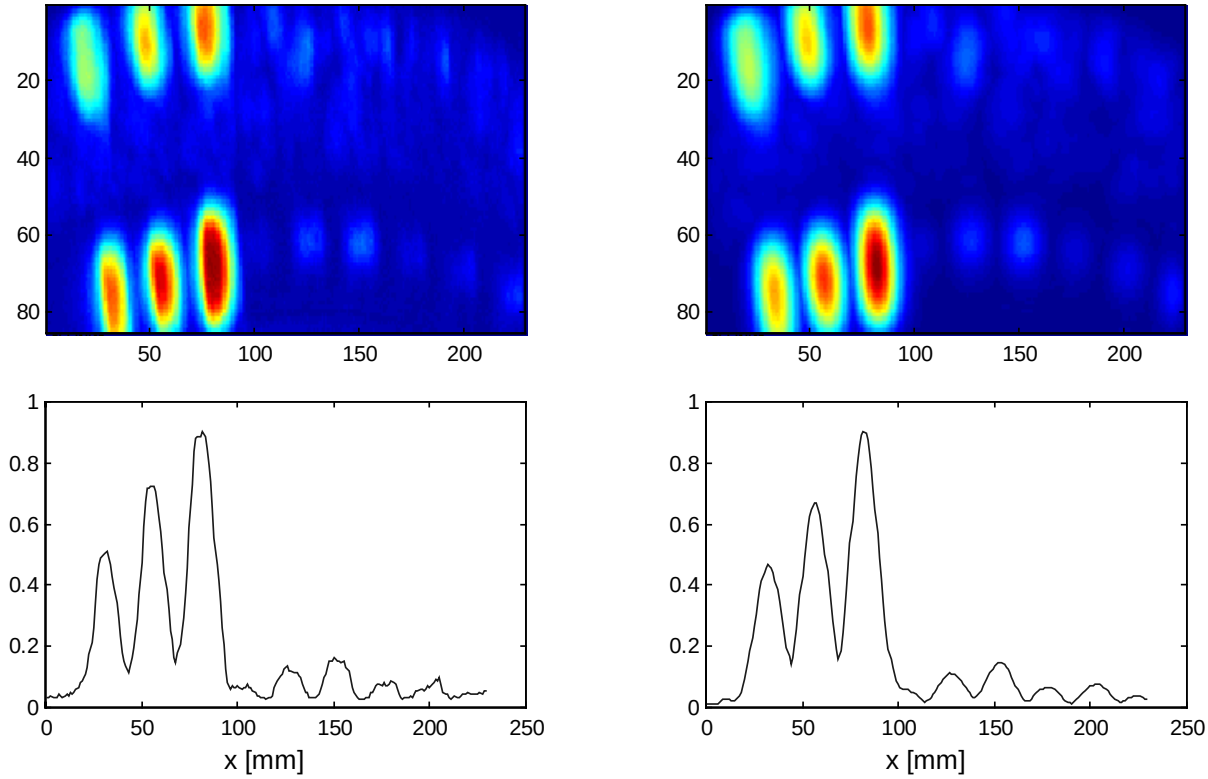

Fig. 2.18. C-scan of the specimen CAN1. Left – extracted from the unprocessed B-scan data. Right – extracted from B-scans processed by 2-D matched filter. Upper row shows C-scans extracted from raw data and the vertical (y) and horizontal (x) axes are in mm. Lower row shows normalized profile of line 62 mm in the C-scans (the largest peaks correspond to the side-drilled holes).

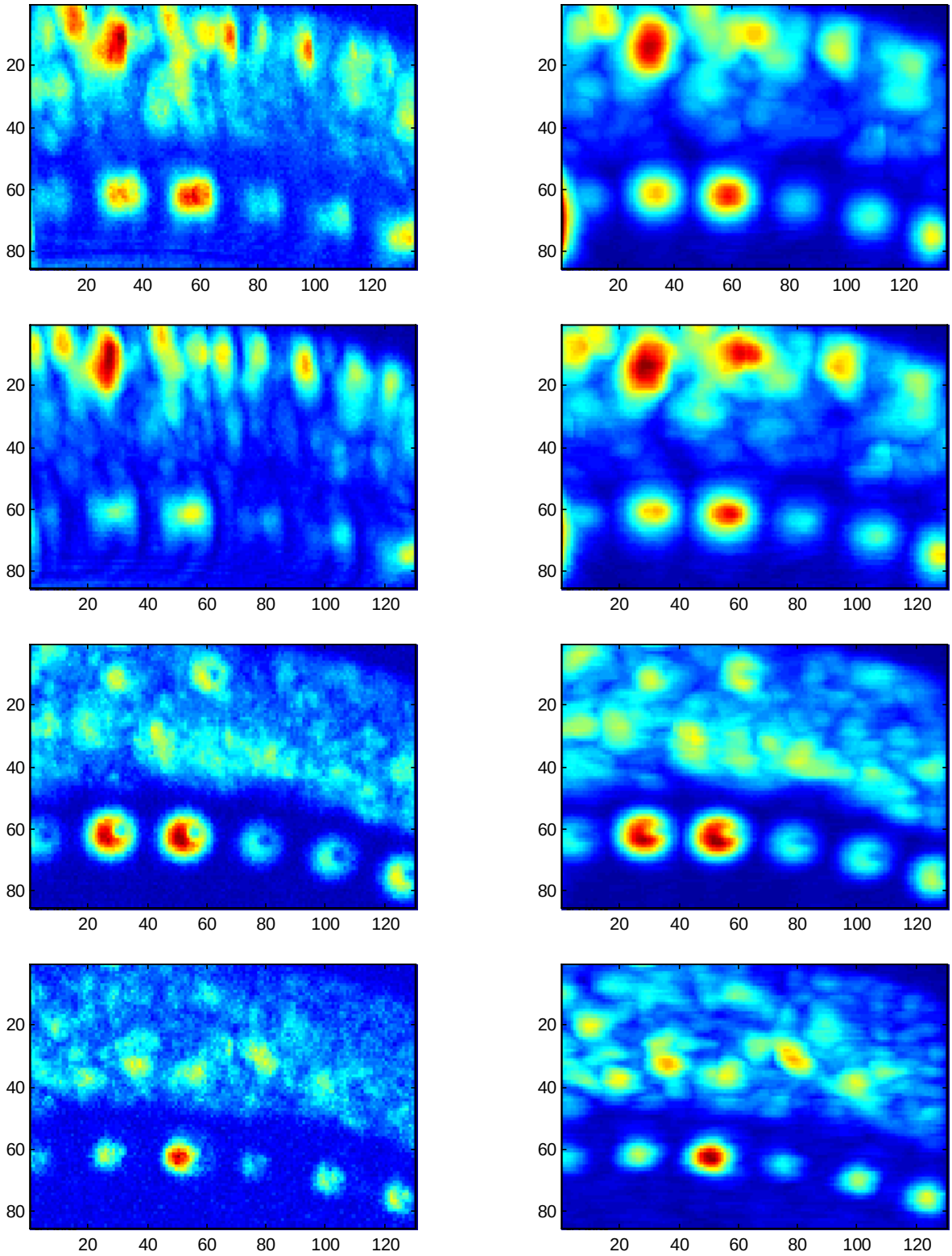

Fig. 2.19. C-scans of the right part of the specimen (bottom holes only). Left column – extracted from the unprocessed B-scan data. Right column – extracted from B-scans processed by 2-D matched filter. Sequential rows from the top show C-scans extracted from full frequency raw data, first, second, and third harmonic, respectively. All the vertical (y) and horizontal (x) axes are in mm.

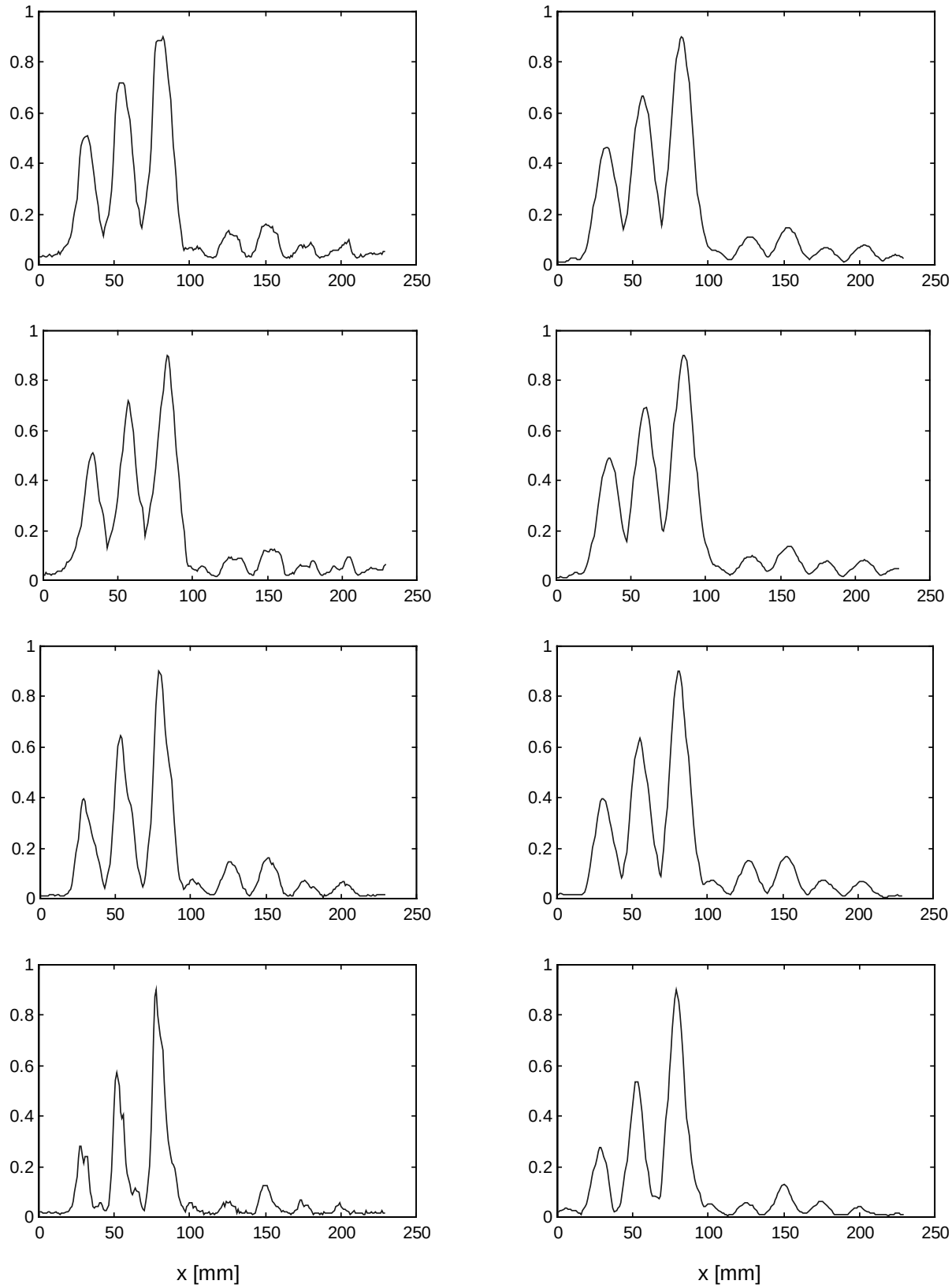

Fig. 2.20. Normalized profiles of at *y*=62 mm in the C-scans of the whole specimen (the largest peaks correspond to the side-drilled holes). Left column – extracted from the unprocessed B-scan data. Right column – extracted from B-scans processed by 2-D matched filter. Sequential rows from the top show lines extracted from full frequency raw data, first, second, and third harmonic, respectively.

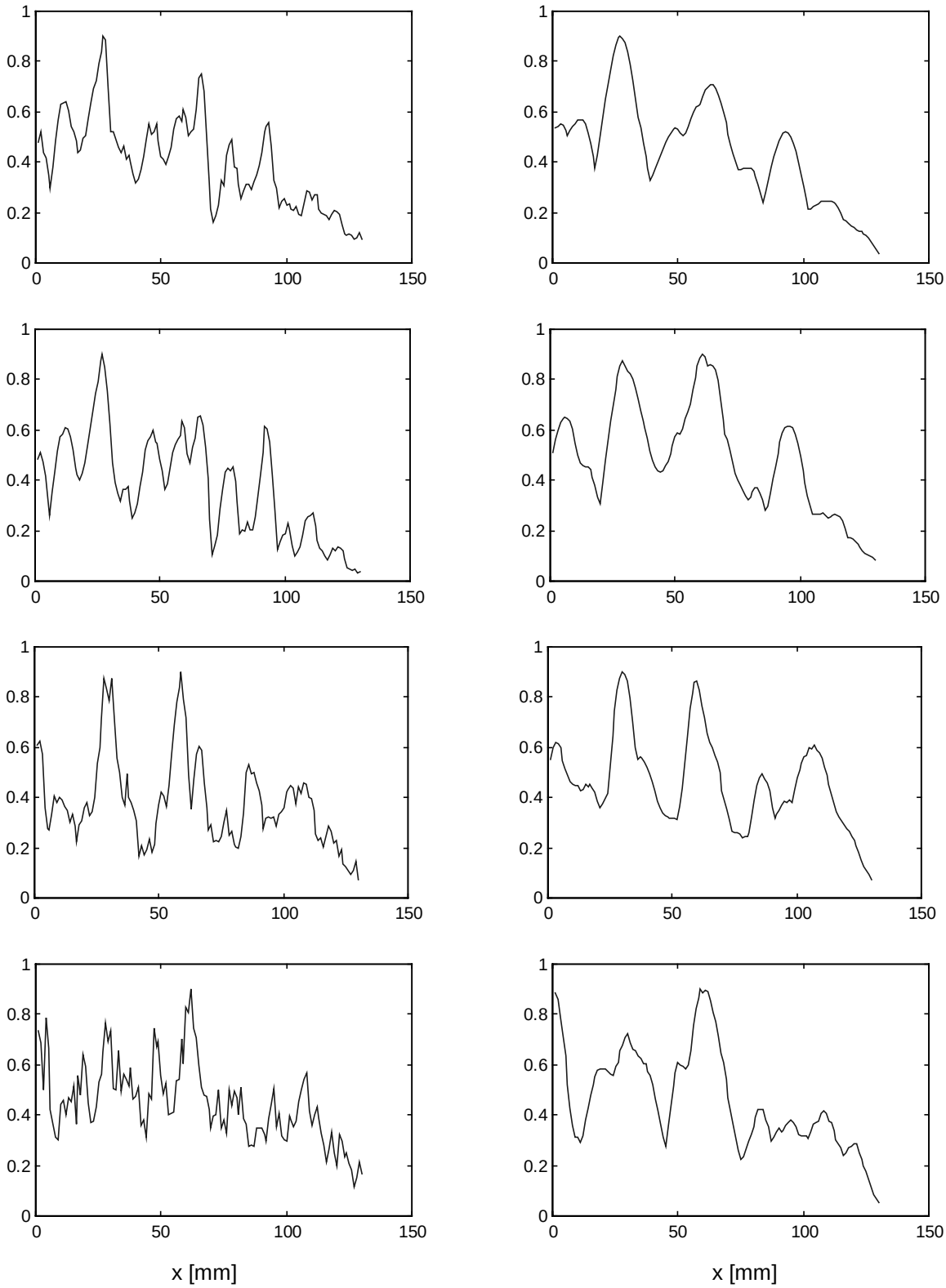

Fig. 2.21. Normalized profiles at *y*=10 mm in the C-scans of the right side of specimen (from the right peaks corresponding to the holes # 4, 5, and 6, respectively). Left column – extracted from the unprocessed B-scan data. Right column – extracted from B-scans processed by 2-D matched filter. Sequential rows from the top show lines extracted from full frequency raw data, first, second, and third harmonic, respectively.

The C-scans extracted from the full frequency data and from the first three harmonics in the region containing bottom-drilled holes are presented in Fig. 2.19. From the first row to the fourth are the C-sans from the full frequency spectrum data and the successive first three harmonics, respectively. The matched filter has averaged the weld scattering without affecting the spatial resolution, which is more easily seen from some profile lines, e.g., in Fig. 2.20 in which the profile lines presented are for y=62 mm. It has to be remembered that the spatial processing of the 2-D matched filter results in processing along the horizontal lines in Fig. 2.19. Strong backscattering from the welded area of the specimen is visible in the upper part of each C-scan. The lower bottom-drilled holes (#13 - #18) can easily be distinguished while the upper ones are masked by backscattering from the EB weld.

The C-scan obtained from the second harmonic, shown in Fig. 2.19, seems to have optimal resolution and signal to noise ratio measured for the bottom-drilled holes. This can be better seen from the profile lines crossing the EB weld with the upper holes (#4 - #9) at y=10 mm (Fig. 2.21). All three holes # 4, 5, and 6 can be distinguished at the processed C-scan extracted from the second harmonic component. It is very interesting that both the resolution and the signal to noise ratio is better for the second harmonic component than for the whole signal spectrum.

From the above examination and analysis it appears that the spatial resolution increases with the order of harmonic component, i.e., the higher order harmonic gives the better spatial resolution. The observed resolution improvement agrees with the theory since the higher harmonic components correspond to the shorter wavelengths.

2.3.2 Harmonic imaging of the copper material

Material harmonics, as defined earlier in the report, originate from the nonlinear propagation of ultrasonic waves in materials. Material harmonic imaging makes use of such harmonics for visualization of some material features. In contrary to the *transducer harmonics* material harmonics do not stem from transducers but from nonlinear distortion of ultrasonic waves propagating in materials. Therefore nonlinear properties of materials can be studied [24,25] and third-order elastic constants of solids can be evaluated [26] using material harmonics. Material harmonics can also be used for enhancing some defects [27, 28] and for detecting some types of material degradation (e.g. fatigue micro-cracking) [29-31]. Unlike tissue harmonic imaging in medicine, material harmonic imaging has not been yet exploited in ultrasonic NDE. In the present study, the nonlinear phenomenon of elastic wave propagation in solids is experimentally investigated, and the possibility of applying the harmonic imaging technology to the NDE is demonstrated. We do hope that this research will stimulate the development of material harmonic imaging technique for the NDE applications, in the way similar to the development of tissue harmonic imaging technique in medical ultrasound.

2.3.2.1 Experimental setup

For this study we have designed a transducer, a two-element array transducer, that has been presented in Chap. 1. In the present case, the transducer is used in pitch-catch mode, that is, the outer element with lower center frequency (2.26 MHz) is used as transmitter, and the inner one with higher center frequency (4.83 MHz) is used as receiver. The experimental setup for the study is schematically shown in Fig. 2.22.

From the previous section (Sect. 2.3.1), we know that transducer harmonics will appear when a transmitter is broadband excited with a pulse. To avoid transducer harmonics and to get material harmonics, we excited the transmitter with a narrow band excitation, a tone burst, whose frequency was close to the transmitter center frequency. In this case only the fundamental resonant mode of the transmitter was excited, and thus the higher-order resonant modes were eliminated. The tone burst was created by the tone burst card TB-1000 made by Matec (more details on the card is given below in Sect. 2.3.2.2), and applied to the transmitter (the outer element). The receiver (the inner element) was connected to the ALLIN system that implements signal amplification, mechanical scanning, and data acquisition.

This study has been conducted systematically in the following steps: first of all the frequency spectrum of the tone burst exciting the transmitter was selected so that only the fundamental resonant mode was excited. Then, material harmonics were examined in water, in copper block with a set of side-drilled holes at different depths (Cu 2), and finally, in copper canister block CAN 1. The two

copper blocks were inspected in immersion configuration, as shown in Fig. 2.22. The water path was set to 30 mm so that the focal zone was located approximately at the depth of EB weld.

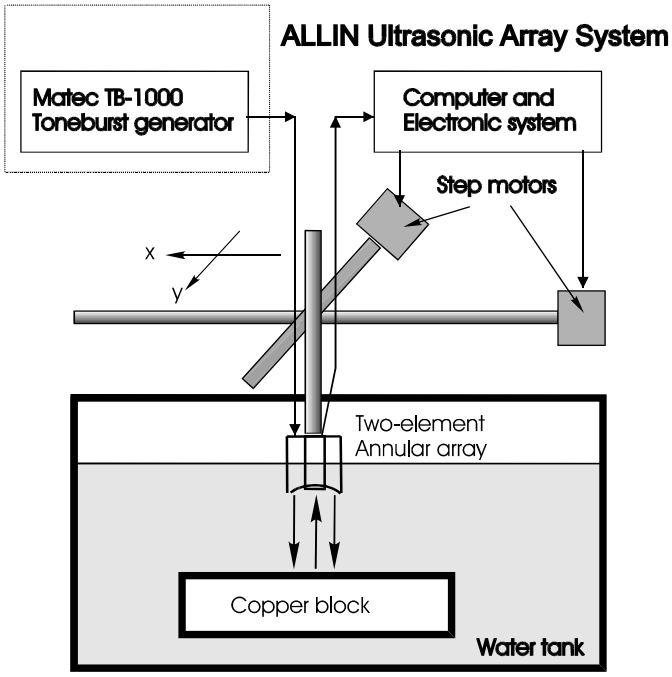

Fig. 2.22. Experimental setup for material harmonic imaging.

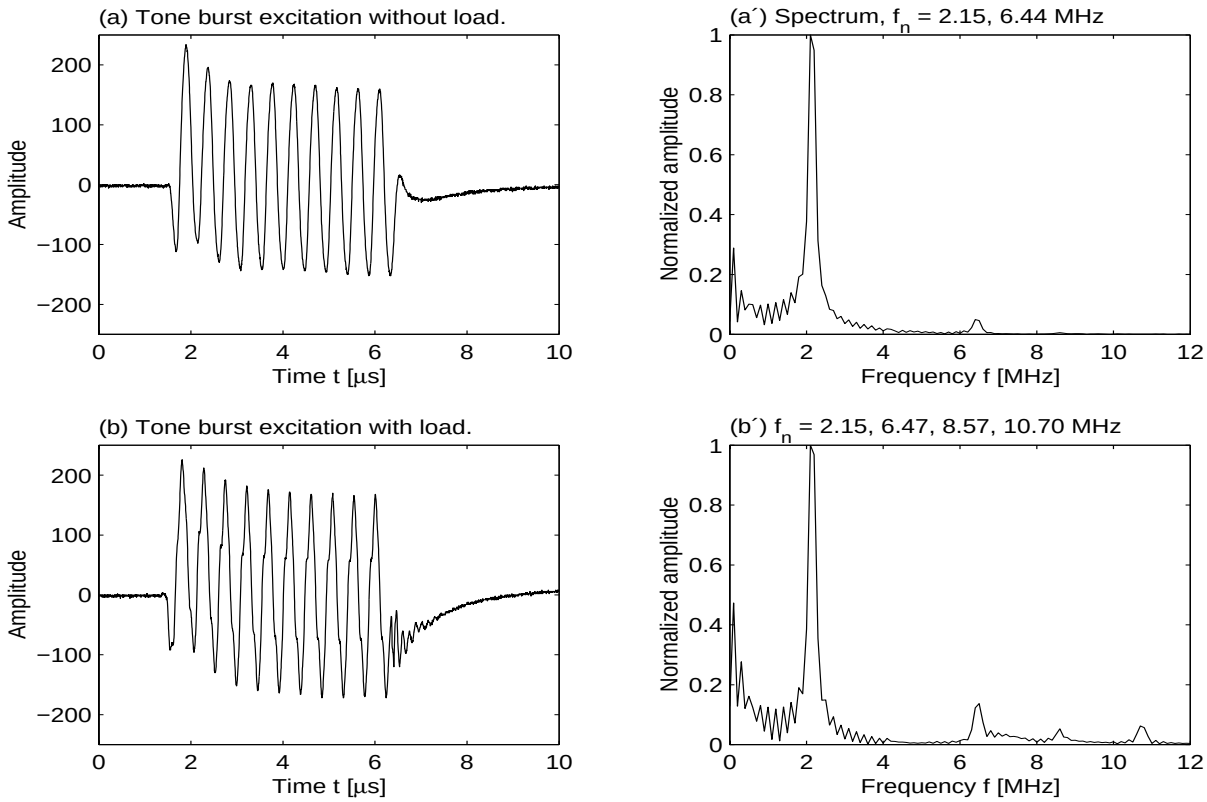

Fig. 2.23. Tone burst excitations (a) when the transmitter is unloaded and (b) loaded, and their spectra shown in (a') and (b'). The spectra are normalized.

2.3.2.2 Excitation to the transmitter -- Tone burst

The tone burst card TB-1000 generates tone bursts that are adjustable in pulse width (or duration), frequency, and amplitude (output voltage). It also has a built-in amplifier that has adjustable gain and 14 high- and low-pass filters. Two output voltages can be chosen, low and high, but they vary with transducers, and tone burst frequencies used. The tone burst frequency can be changed from 50 kHz to 20 MHz with a minimum step of 50 kHz. The filters allow various combinations to produce band-pass filters of varying bandwidth. The 3-dB roll-off frequencies for both high- and low-pass filter selections are NONE, 100 kHz, 250 kHz, 500 kHz, 1.00 MHz, 2.25 MHz, 5.00 MHz, and 10.0 MHz.

The output tone burst card of the TB-1000 was recorded in two cases, in unloaded condition and loaded with the transmitter. Although the measured center frequencies of the outer and inner elements are 2.26 and 4.83 MHz, the maximum amplitude frequencies of the two elements are about 2.0 and 4.4 MHz, respectively. Therefore, the tone burst was tuned to 2.15 MHz, which seemed to give a relatively larger output to the receiver receiving an echo from a point scatterer in water. With the transmitter loaded at frequency of 2.15 MHz, the peak-peak amplitude was above 300 volts for the low voltage output and approximately 400 volts for the high voltage output. Both low and high voltage outputs were used in the measurements. The duration was almost 11 cycles, which makes 5.1 μs. The tone bursts and their spectra in the unloaded and loaded conditions with lower voltage output level are shown in Fig. 2.23. From the spectra we can see that the tone burst in the unloaded condition had a narrow band at fundamental frequency (2.15 MHz) and another band with small amplitude at the third harmonic frequency (6.44 MHz), but not at the second harmonic frequency (4.30 MHz). When the card was loaded, the tone burst still had a narrow band at fundamental frequency (2.15 MHz) and its bandwidth was slightly increased. Small amplitude at the third harmonic frequency (6.44 MHz) was observed, but the second harmonic frequency (4.30 MHz) was not present. Moreover, peaks at the fourth, and sixth harmonic frequency (8.57, and 10.70 MHz) appeared in the spectrum with small amplitudes. This may demonstrate that the fundamental resonant mode of the transmitter is dominant, the second resonant mode is almost not excited, and the energy of the higher-order resonant modes is small compared to the fundamental mode.

From the above observation, we conclude that the fundamental resonant mode of the transmitter under this tone burst excitation is dominant, and the higher-order resonant modes are small, especially the second one is almost unexcited.

2.3.2.3 Harmonic generation in water

Harmonic generation in water has been dealt with for several decades and a large amount of literature on nonlinear acoustic waves and harmonic generation is available [32-34]. Here, we have

also examined nonlinear acoustic waves and harmonic generation from our system shown in Fig. 2.22. This was made for reference before studying harmonic generation in solids, which will be presented in the following sections (Sects. 2.3.2.4 and 2.3.2.5).

With the above tone burst (Fig. 2.23) exciting the transmitter with the lower frequency, the echoes from a point scatterer were measured at different positions by the receiver with the higher frequency. The measurements were made on the axis of the transducers at positions z=65, 74, 95, 115, 135, 155, and 195 mm. The echoes and their spectra are shown in Fig. 2.24. The measurements were also made off the axis at positions x=0, 1.2, 2, and 2.8 mm for z=195 mm. All the spectra are normalized so that the higher harmonics are easy to compare to the fundamental component. Earlier results [32,33] have shown that on the whole a fundamental field pattern of a nonlinear field is quite similar to that of a corresponding linear field radiated by a transducer with the same frequency as the fundamental. Therefore, it is reasonable use the fundamental field as a reference for comparison. However, it must be noted that the receiver had a limited bandwidth of 73% with a center frequency of 4.83, and thus it had a much better sensitivity to the second harmonic than to the fundamental and to the higher harmonics.

Looking at the on-axis results in Fig. 2.24, one can see that the high harmonics (e.g., 2nd – 5th harmonics) increase with distance towards the focal point (210 mm). For example, the echo at z=65 mm (Fig. 2.24(a) and (a')) have small second and third harmonics. Whereas the echo at z=195 mm has strong second and third harmonics that are both larger than the fundamental one. It also has a considerably large fourth harmonic and a small fifth harmonic.

Each harmonic has its beam pattern. The higher the harmonic the narrow the beam width [32-34], which is a feature similar to case of linear acoustics. This feature can be roughly seen when examining the off-axis results in Fig. 2.25. The spectra for the echoes at x=0, 1.2, and 2 (Fig. 2.25(a)-(c)) show that the second to fourth harmonics become smaller relatively as the off-axis distance increases. After increasing the distance to x=2.8 mm the second harmonic becomes larger than the fundamental again. The reason is that at this position the side lobe of the second harmonic appears. Since the measurements were made at sparse positions and limited distance, the harmonic beam patterns cannot be figured out in a complete picture. However, much similar results can be found in the existing literature (e.g., [32-34]). Our attention is focused on harmonic generation in solids, which is presented below.

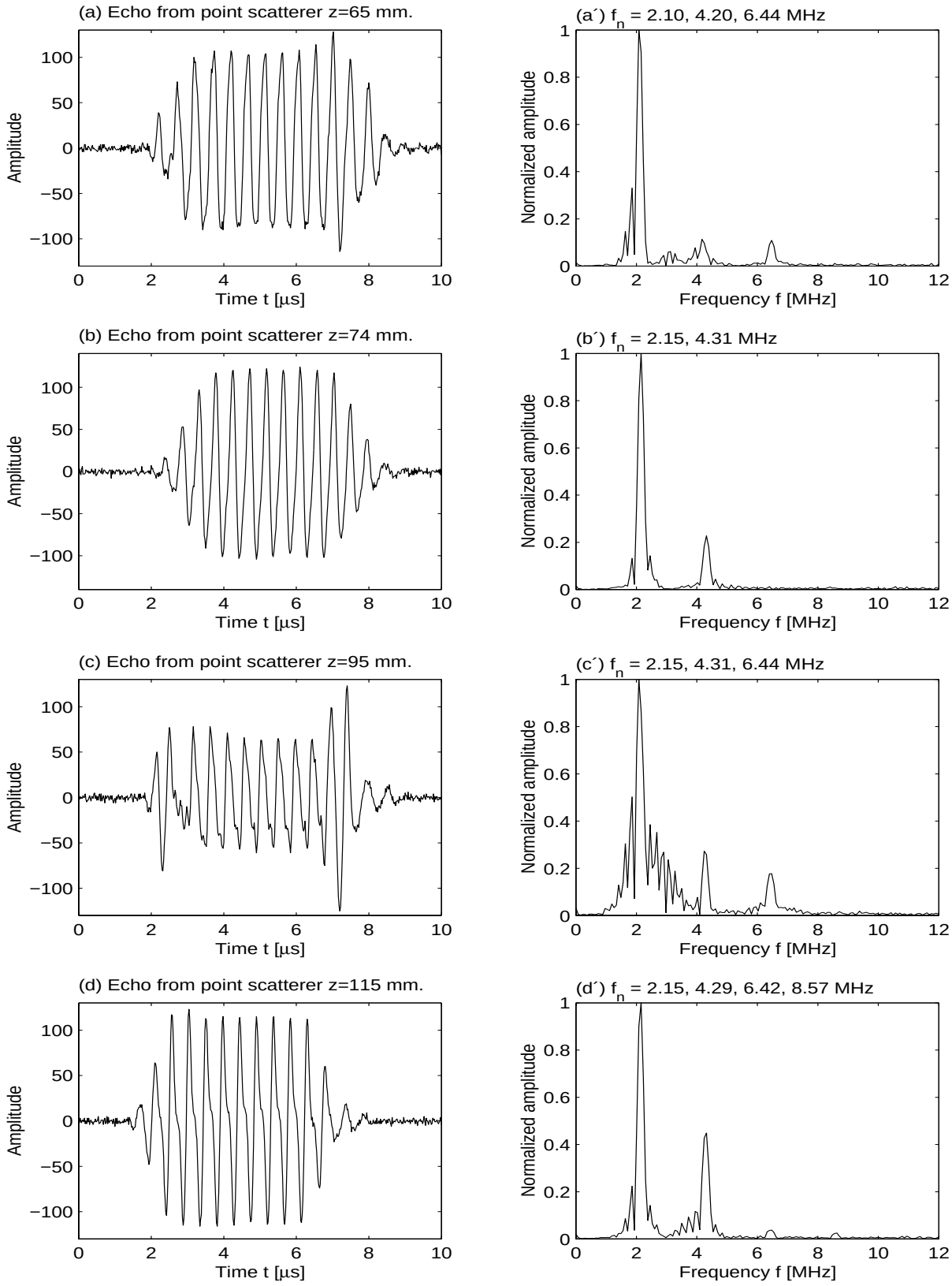

Fig. 2.24. Pulse echoes from a point scatterer at different distances on the transducer axis. (a) *z*=65 mm, (b) *z*=74 mm, (c) *z*=95 mm, (d) *z*=115 mm, (e) *z*=135 mm, (f) *z*=155 mm, (g) *z*=195 mm.

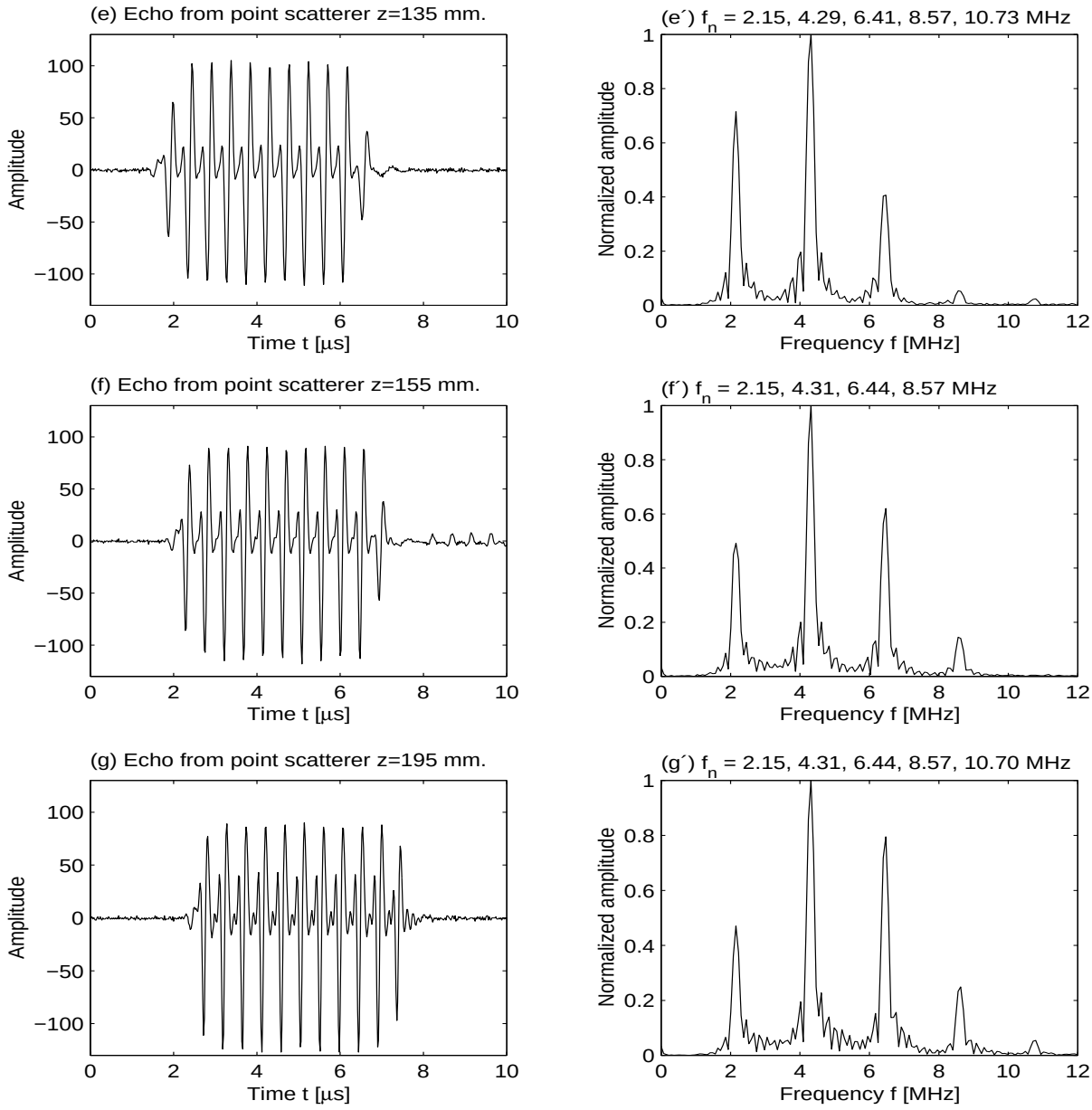

Fig. 2.24. Pulse echoes from a point scatterer at different distances on the transducer axis. (a) *z*=65 mm, (b) *z*=74 mm, (c) *z*=95 mm, (d) *z*=115 mm, (e) *z*=135 mm, (f) *z*=155 mm, (g) *z*=195 mm.

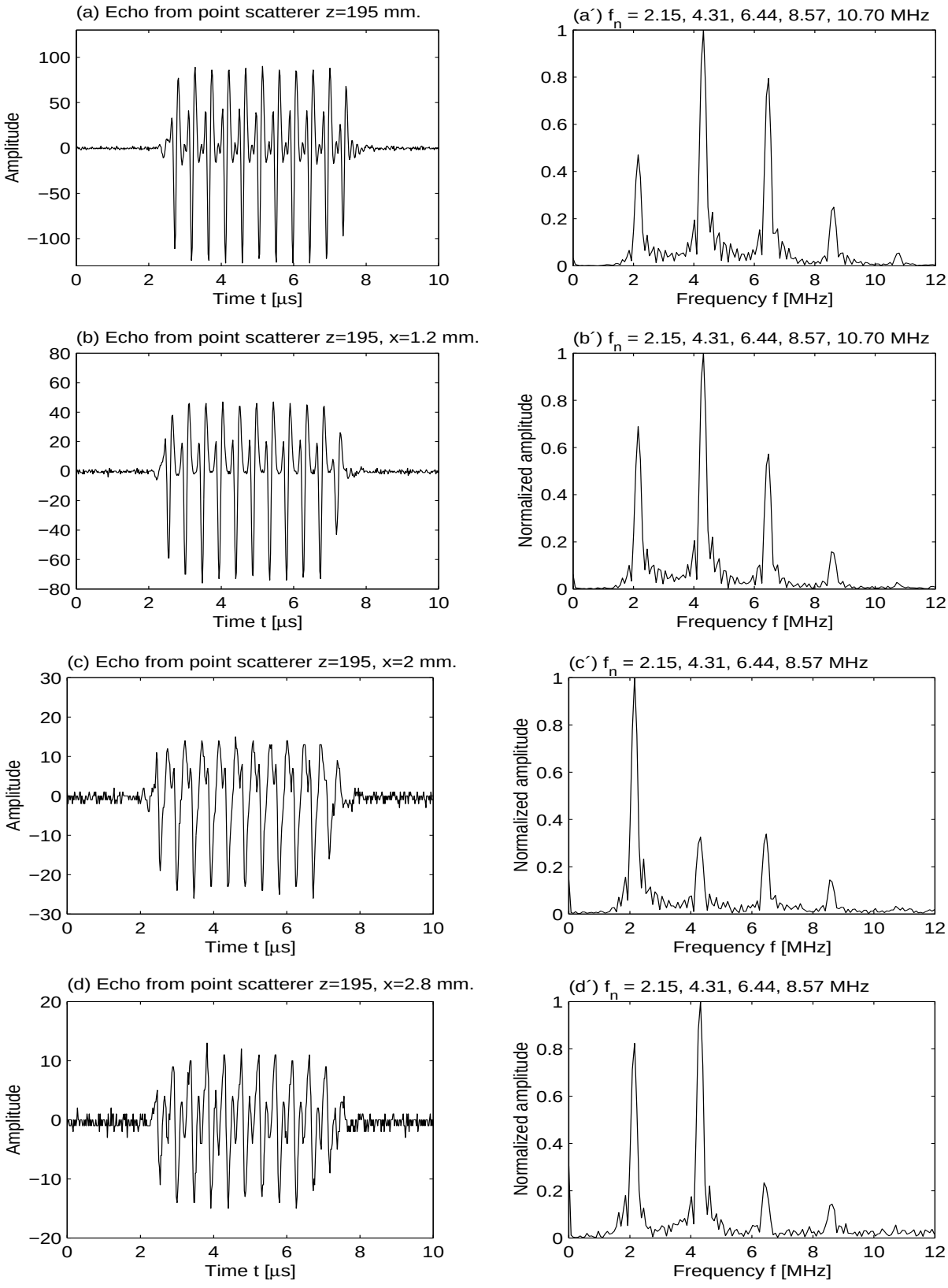

Fig. 2.25. Pulse echoes from a point scatterer at different distances off the transducer axis: (a) *x*=0 mm, (b) *x*=1.2 mm, (c) *x*=2 mm, and (d) *x*=2.8 mm for *z*=195 mm.

2.3.2.4 Harmonic generation in copper block CU 2

The solid material in which harmonics are to be generated is copper block CU 2 that has 18 side-drilled holes (SDH) at different depths (Fig. 2.26). The experimental setup used has been shown in Fig. 2.22. The two-element transducer was put over the copper block immersed in water and the water path was 30 mm. The duration of the tone burst excitation was slightly increased to 5.6 μs (12 cycles, at frequency 2.15 MHz). The receiving transducer was connected to the TB-1000's amplifier and then to the ALLIN system. The transducer pair was scanned in the *x* direction (see Fig. 2.26). A series of measurements were made on CU 2 using different voltages (both low and high) and different settings of the high- and low-pass filters of the TB-1000 amplifier.

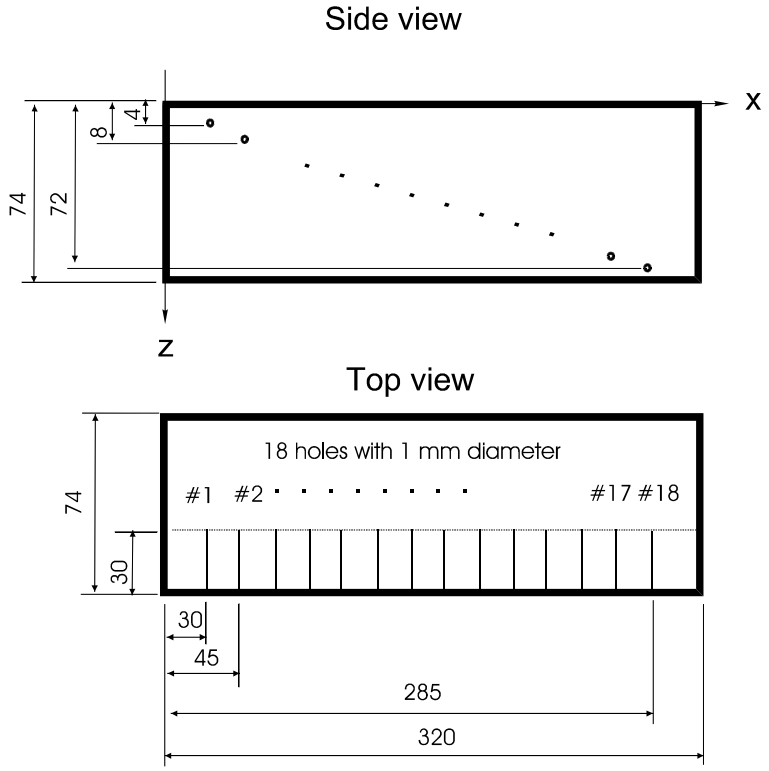

Hole #	3	4	5	6	7	8	9	10	11	12	13	14	15	16
z [mm]	12	16	20	24	28	32	36	40	44	48	52	56	60	64

Fig. 2.26. Geometry of copper block CU2.

To keep the report in a reasonable size, we are only presenting some selected results measured with high voltage output and two filter settings. First, we show the results for both high- and low-pass filters set NONE (a kind of flat filter in the maximum frequency band), and second, for the high-pass

filter set to 5 MHz and low-pass to NONE (just a 5-MHz high-pass filter). B-scan of CU 2 obtained for the first filter setting is shown in Fig. 2.27(a), along with the profile of peak magnitude of the B-scan as a function of *x*, shown in Fig. 2.27(b). The profile which is a good illustration of elastic field propagation can be also used to pick out any echoes of interest. For instance, the echo from hole #10, one of the largest, is picked out and shown in Fig. 2.28(a), together with its linear spectrum (b) and log spectrum (c). In the linear spectrum plot (Fig. 2.28(b)) the fundamental at f_1=2.15 MHz is apparently strong and the 2nd harmonic can also be seen at f_2=4.31 MHz although small. However, the 3rd harmonic at f_3=6.44 MHz is so small that it is hard to see. But these two high harmonics are easily seen at f_2 and f_3 in the log spectrum in Fig. 2.28(c). From the log spectrum, it can be seen that the 2nd harmonic is 22 dB smaller and the 3rd is 40 dB smaller than the fundamental.

To emphasize high harmonics (2nd or high order), we used two available filter settings on TB-1000, namely, 2.5- and 5.00-MHz high-pass filters, and we found that the 5-MHz high-pass filter gave a better enhancement to high harmonics. Therefore, the measured results using the 5-MHz high-pass filter are presented here. The echoes from SDH #6 - #15 located at different distances (refer to the table in Fig. 2.26) are presented in Fig. 2.29, respectively, in panels (a)-(j), the linear spectra of the echoes are, respectively, in panels (a')-(j'), and the log spectra are collected in Fig. 2.30. From Fig. 2.29(a)-(j), the growth of nonlinear distortion of waves propagating in the solid can be seen. This nonlinear distortion results in harmonics in the frequency domain (c.f., the spectra in Fig. 2.29(e') and Fig. 2.30(e")). A comparison of the spectra in Fig. 2.28 with those in Fig. 2.29(e') and Fig. 2.30(e") demonstrates that the 5-MHz high-pass filter makes the high harmonics (2nd, 3rd, and even 4th) much more pronounced. In the linear spectra the 2nd and 3rd harmonics are clearly visible and in the log spectra besides the 2nd and 3rd harmonics the 4th one is also shown up in panels (c")-(j"). Observing each harmonic in the spectra in Figs. 2.29 and 2.30, we may get a rough picture of the development of each harmonic with propagation distance, e.g., the 2nd harmonic increases with depth.

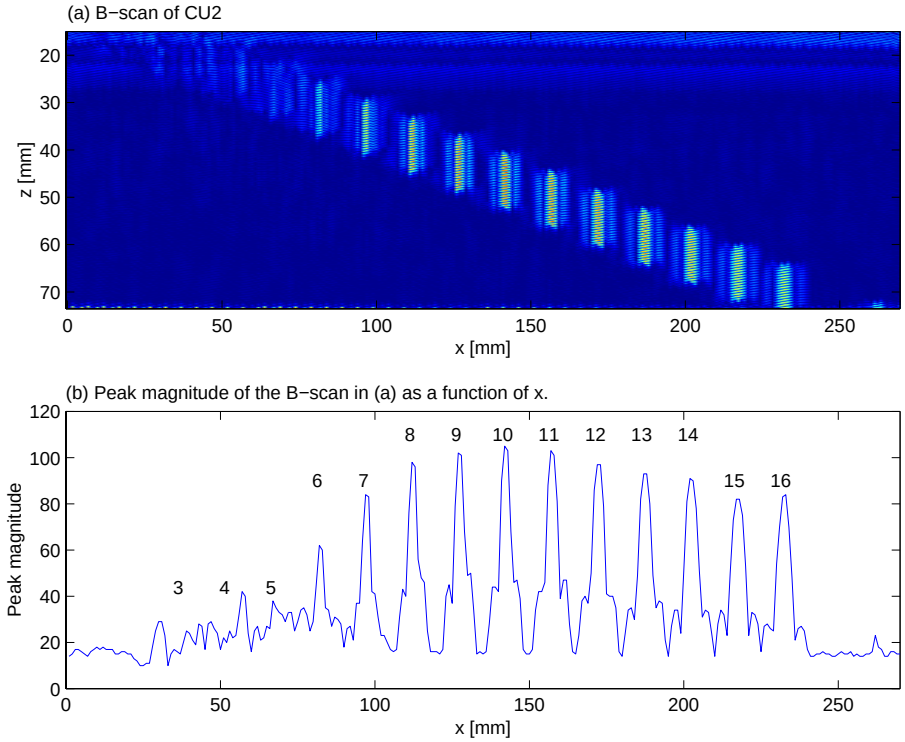

Fig. 2.27. (a) B-scan of CU2 and (b) its peak magnitude as a function of *x*.

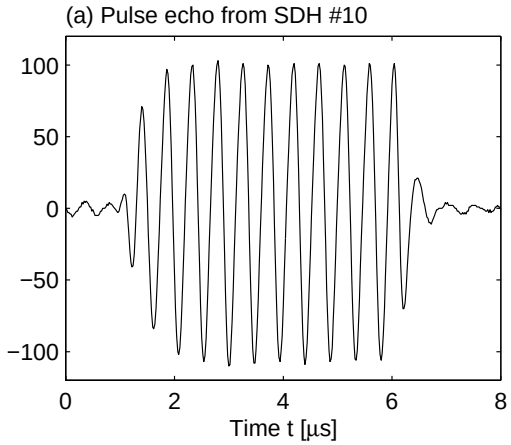

Fig. 2.28. (a) Pulse echo from SDH #10, (b) its spectrum, and (c) its log spectrum.

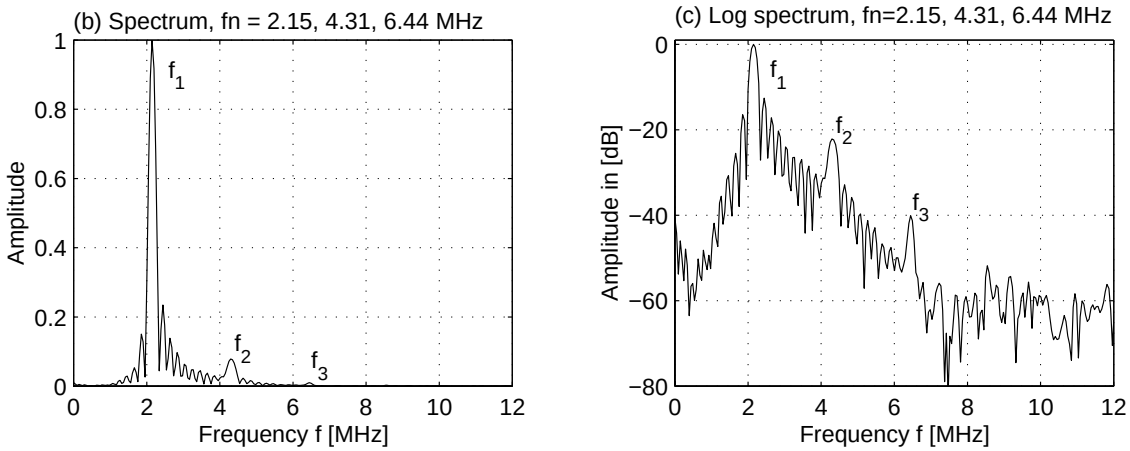

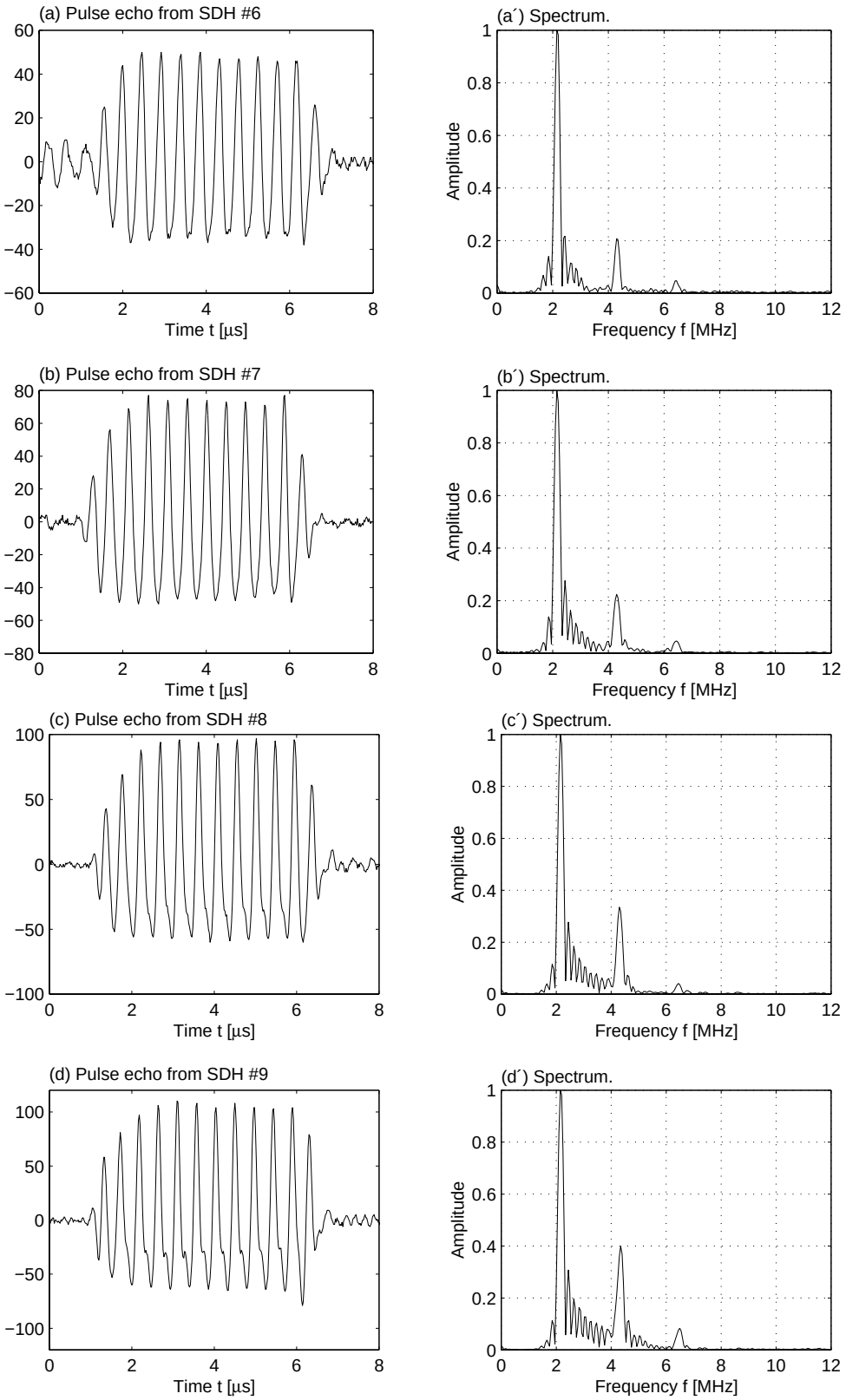

Fig. 2.29. Pulse echoes from SDHs #6 - #15, respectively, shown in (a) to (j), and their spectra, respectively, shown in (a') to (j').

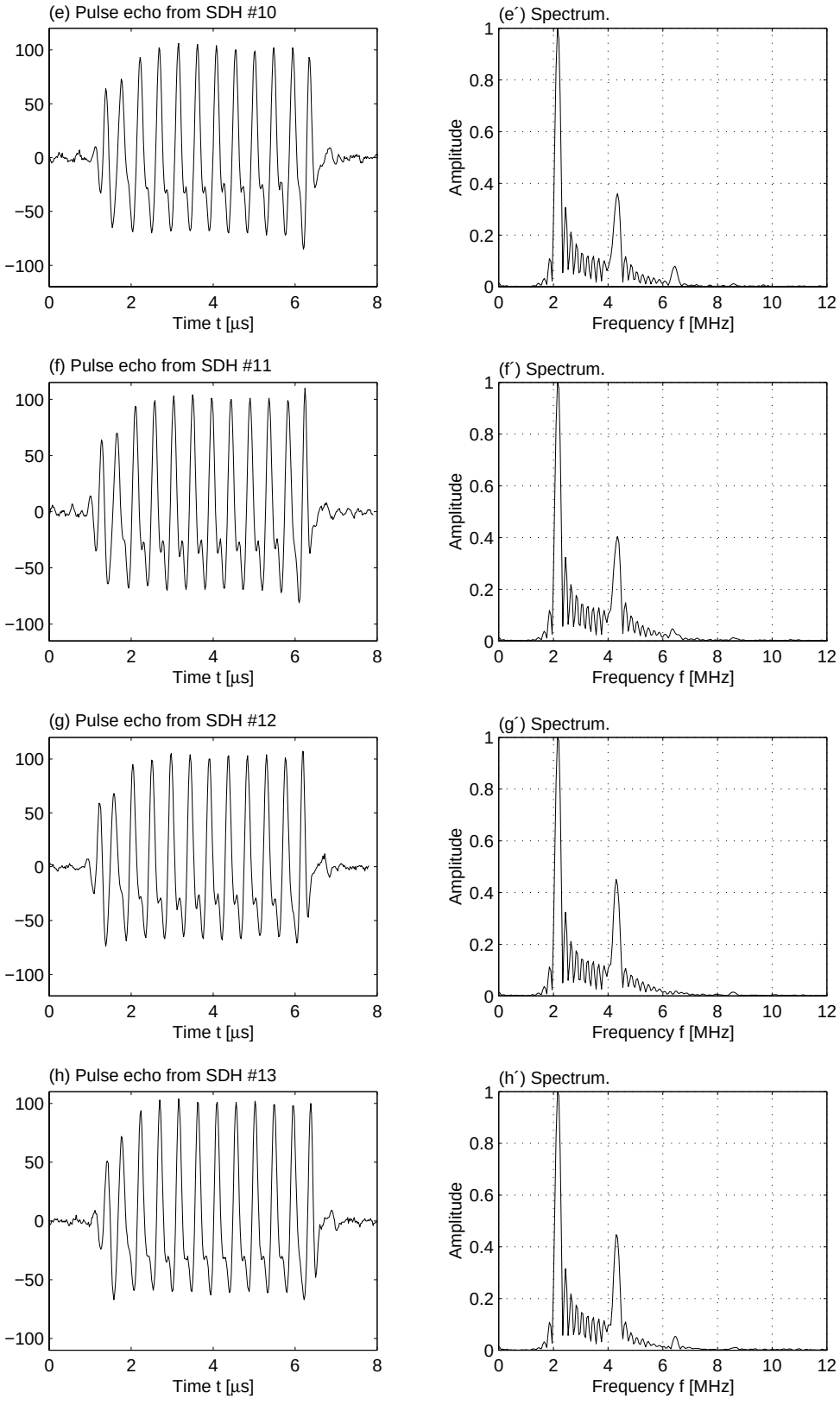

Fig. 2.29. Pulse echoes from SDHs #6 - #15, respectively, shown in (a) to (j), and their spectra, respectively, shown in (a') to (j').

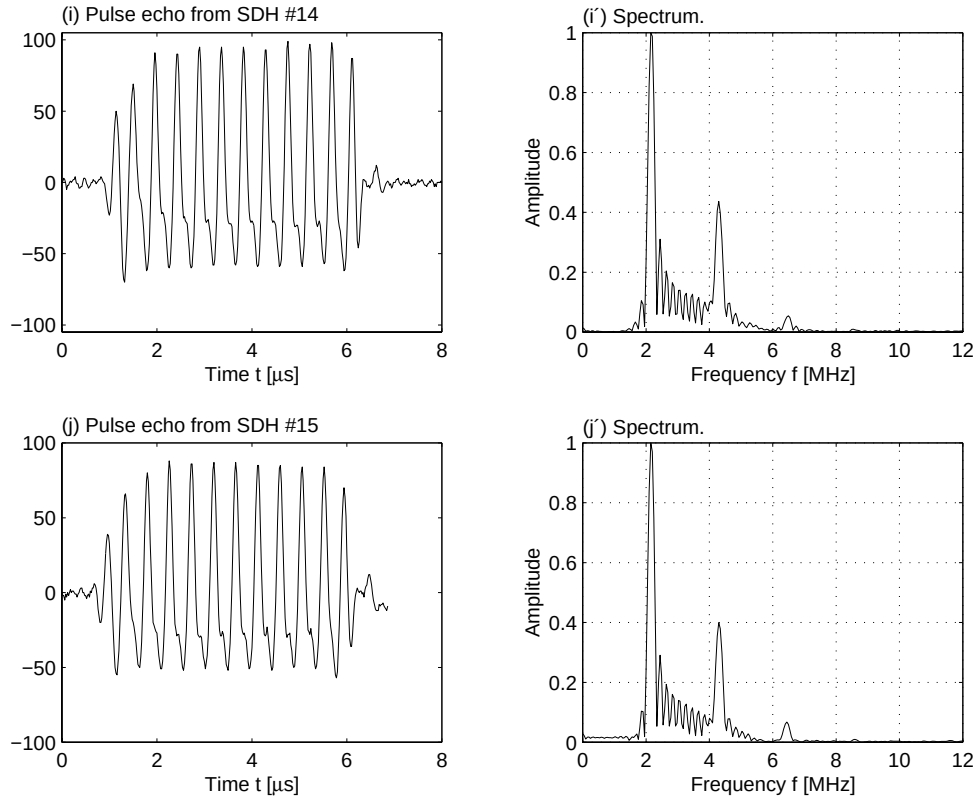

Fig. 2.29. Pulse echoes from SDHs #6 - #15, respectively, shown in (a) to (j), and their spectra, respectively, shown in (a') to (j').

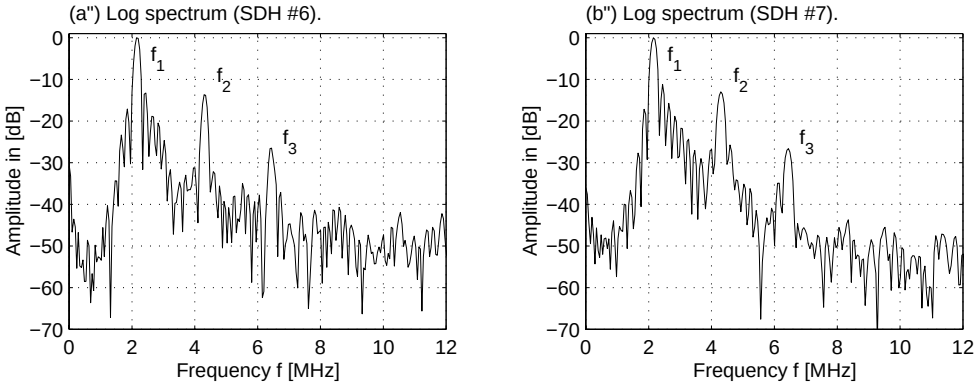

Fig. 2.30. Log spectra of the pulse echoes from SDHs #6 - #15, respectively, shown in (a") to (j").

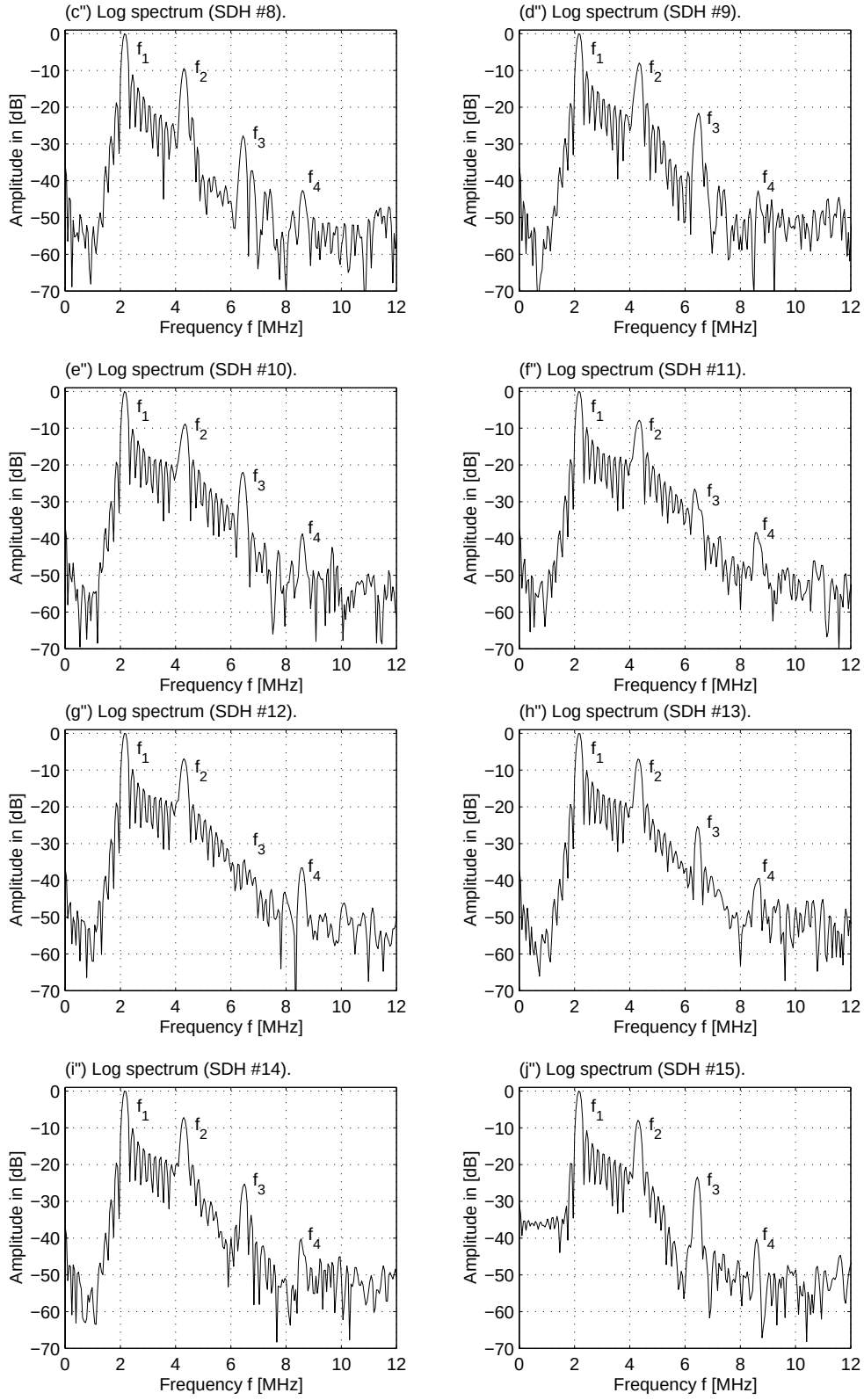

Fig. 2.30. Log spectra of the pulse echoes from SDHs #6 - #15, respectively, shown in (a") to (j").

2.3.2.5 Harmonic imaging of the EB weld in copper block CAN 1

In the previous section (Sect. 2.3.2.4) it has been shown that it is possible to generate high harmonics in copper block CU2 up to fourth order, however, they are much weaker than the harmonics generated in water (Sect. 2.3.2.3). In this section, we employ the same experimental setup (Fig. 2.22) to generate harmonics in a copper canister block CAN1 and then to construct the harmonic images of the EB weld in the canister.

A series of measurements were made on CAN 1 using a similar procedure and conditions as that described in Sect. 2.3.2.4. The transducer was scanned over the block in a dimension of 270x85 mm with a step of 1 mm. The first measurement was made with high excitation voltage and the low- and high-pass filter set to NONE on TB-1000. In this case, the fundamental component is dominant and the higher harmonics are small, similarly to the case presented in Fig. 2.28 in the previous section (Sect. 2.3.2.4). A C-scan was extracted from the acquired data using the gate covering the whole EB weld, and it is shown in Fig. 2.31. From the C-scan we selected the following six positions of interest: SDH #3 (x=77 mm, y=10 mm), FBH #6 (x=159 mm, y=10 mm), SDH #12 (x=82 mm, y=61 mm), FBH #15 (x=154 mm, y=61 mm), and two EB weld spots (x=100 mm, y=27 mm) and (x=168 mm, y=27 mm). A-scans acquired at these positions will be presented for the purpose of demonstrating harmonics. These A-scans that come from another measurement made using the high voltage output and the 5-MHz high-pass filter, and are shown in Fig. 2.32 together with their log spectra. When observing the harmonics it is good to bear in mind that SDH #12 and FBH #15 are in the non-welded zone, and the rest positions are in the welded zone.

Looking at the spectra of the echoes from SDH #12 and FBH #15 (Fig. 2.32(c') and (d')), we can see the higher harmonics up to the fourth order. A comparison of the echoes (Fig. 2.32(c) and (d)) reveals that the nonlinear distortion of the echo (backscattering) from FBH #15 looks more pronounced than from SDH #12. A comparison of the spectra demonstrates that all high harmonics of the SDH #12 echo are larger than those of the FDH #15, and the second harmonic of the SDH #12 echo is even larger than that of the fundamental.

From the spectra of the SDH #3 and FBH #6 echoes (Fig. 2.32(a') and (b')) the second and third harmonics are clearly visible, and the fourth in the SDH #3 spectrum is just recognizable and in the FBH #6 spectrum does not appear. The nonlinear distortion of the FBH #6 echo (Fig. 2.32(b)) still looks more pronounced than the SDH #3 (Fig. 2.32(a)). Compared to the SDH #12 and FBH #15 echoes, the SDH #3 and FBH #6 echoes exhibit less pronounced nonlinear distortions. The higher attenuation in the EB weld and the reflection loss at the HAZ/FZ are among the reasons for this.

Moving to the echoes from two EB weld spots (Fig. 2.32(e) and (f)) and their spectra (Fig. 2.32(e') and (f')), we first can see that these two echoes are significantly smaller than those corresponding to the four holes (SDH #3 and #12 and FBH #6 and #15). And secondly we see that the nonlinear

distortion in this case is still apparent, the 2nd and 3rd harmonics are clearly there although smaller than for the echoes from the four holes, however the fourth harmonic is not present.

The above presented observations and analysis we have confirmed that it is possible to generate harmonics in an EB weld. This also reveals that harmonic imaging of EB welds is feasible. Now we will extract the harmonics applying the Hanning widows with center frequencies being the same as the harmonics to the spectra. After extracting harmonics, A-, B- and C-scans of each harmonic are available. Here we only present the C-scans of the fundamental to the fourth harmonics (Fig. 2.33). The fundamental C-scan of the EB weld, extracted from the measured data (when the low- and high-pass filter was set to NONE) is shown in Fig. 2.33. Since the fundamental component is dominant, this fundamental C-scan looks very similar to the one in Fig. 2.31. The 2nd to 4th harmonic C-scans in Fig. 2.33(b)-(c) were obtained from the data measured with the 5-MHz high-pass filter (six A-scans used for thes C-scan are displayed in Fig. 2.32). All the SDHs (#1-#3 and #12-#15) and the FBHs (#13-#18) in the non-welded zone are seen both in the fundamental C-scans and in the 2nd and 3rd harmonic C-scans. The SDHs #10-#12, the FBHs #14-#15 and parts of the SDHs #2-#3 are possibly recognized in the fourth harmonic C-scan. The fourth harmonic C-scan can be further improved by adjusting the amplitude scale.

Comparing the images of the holes in these four C-scans yields that the spatial resolution becomes better for the higher-order harmonic image. Observation of the grain noise may allow us to say that the grain noise pattern becomes finer for the higher-order harmonic.

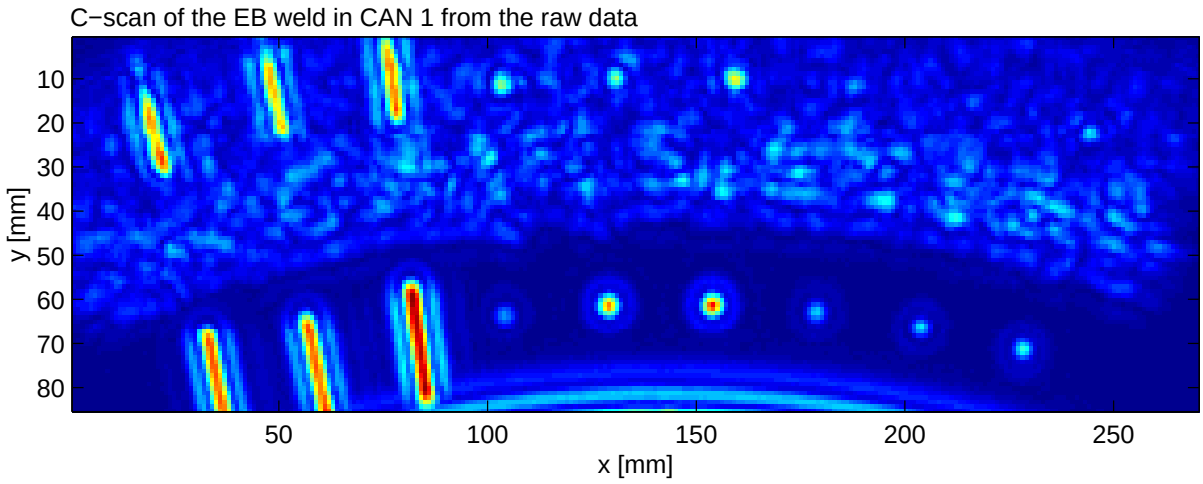

Fig. 2.31. C-scan of the EB weld in CAN 1 from the raw data.

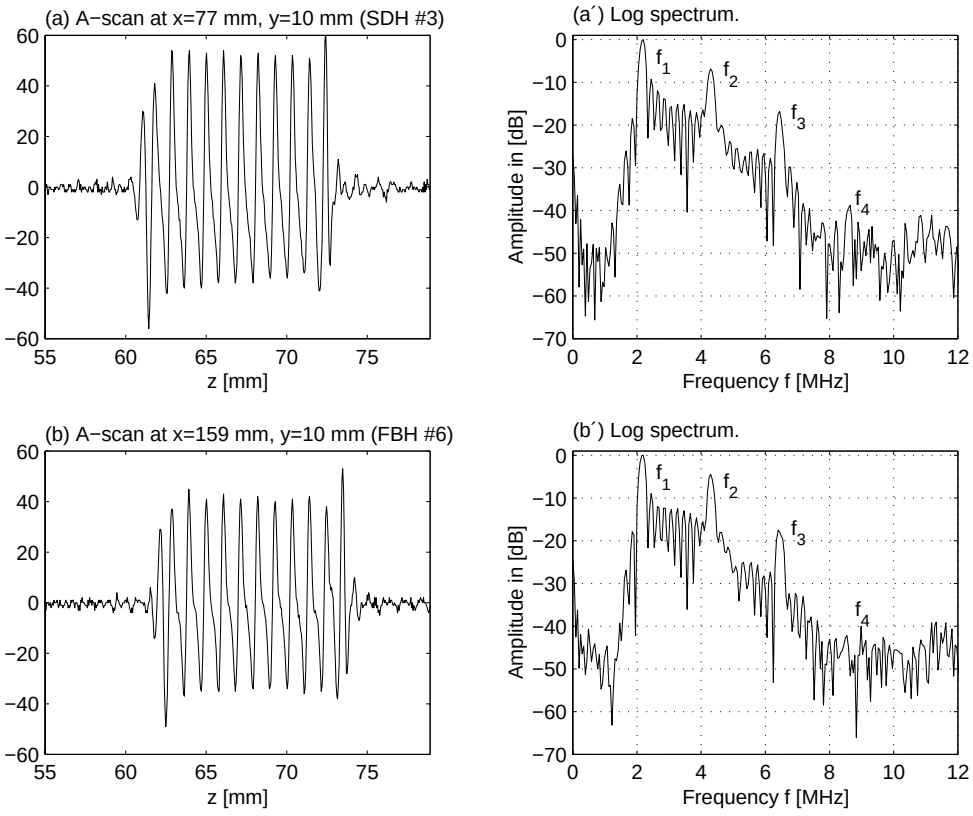

Fig. 2.32. A-scans at positions (a) *x*=77 mm, *y*=10 mm (SDH #3), (b) *x*=159 mm, *y*=10 mm (FBH #6), (c) *x*=82 mm, *y*=61 mm (SDH #12), (d) *x*=154 mm, *y*=61 mm (FBH #15), (e) *x*=100 mm, *y*=27 mm (weld), and (f) *x*=168 mm, *y*=27 mm (weld).

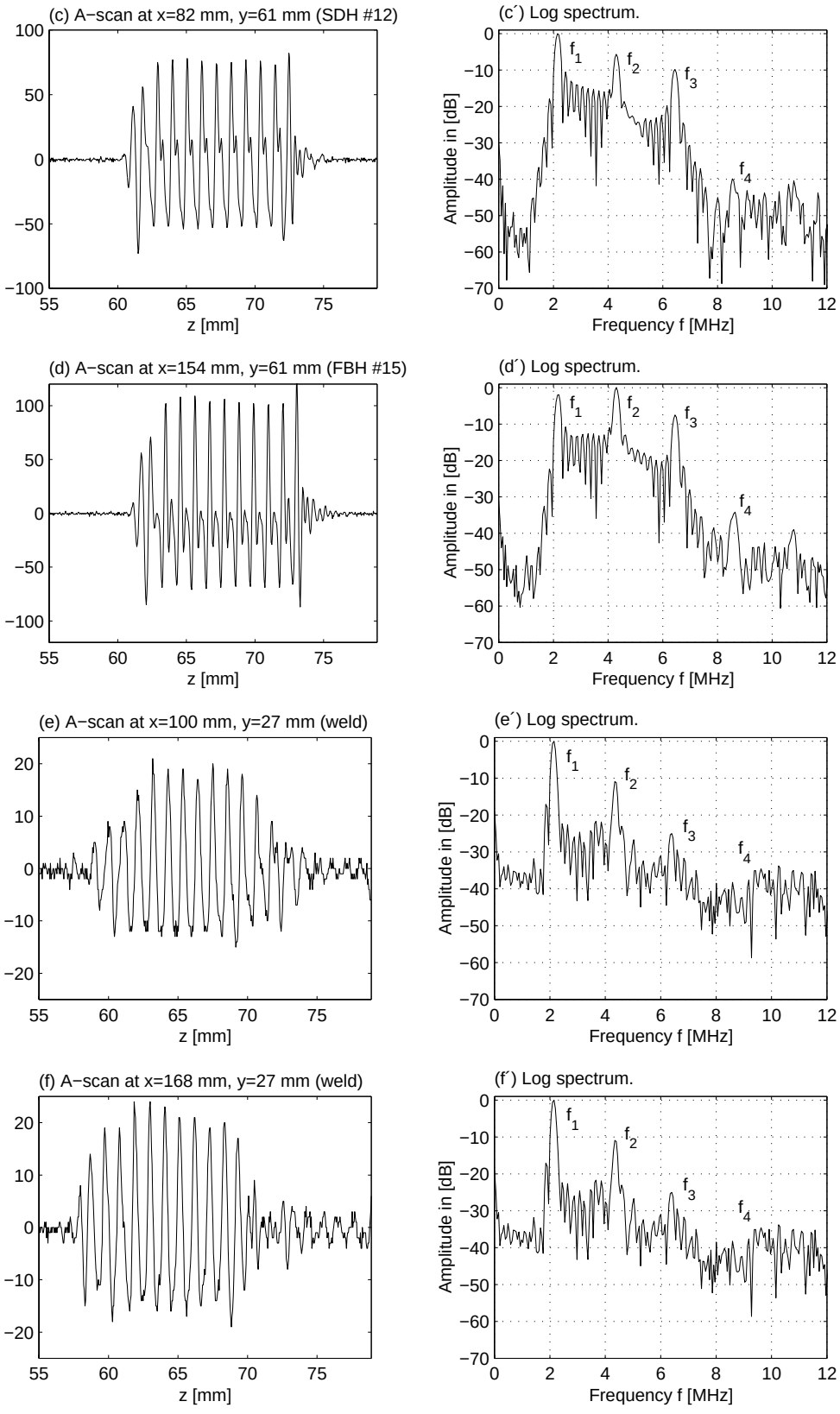

Fig. 2.32. A-scans at positions (a) *x*=77 mm, *y*=10 mm (SDH #3), (b) *x*=159 mm, *y*=10 mm (SDH #6), (c) *x*=82 mm, *y*=61 mm (SDH #12), (d) *x*=154 mm, *y*=61 mm (SDH #15), (e) *x*=100 mm, *y*=27 mm (weld), and (f) *x*=168 mm, *y*=27 mm (weld).

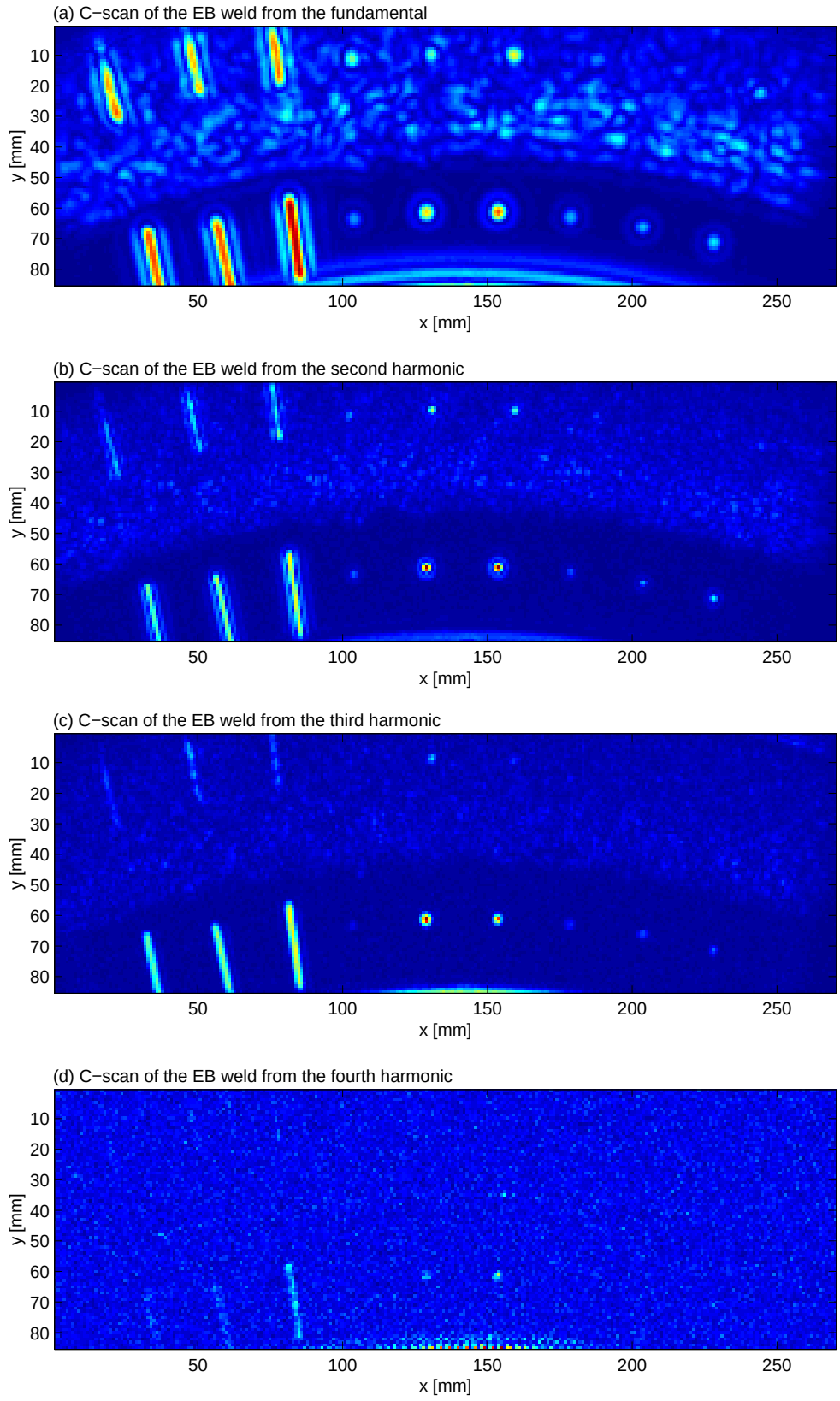

Fig. 2.33. C-scans of the EB weld in CAN 1 from (a) the fundamental, (b) the second, (c) the third, and (d) the fourth harmonic.

2.4 Grain noise suppression and flaw detection enhancement

2.4.1 Introduction

In the previous research filter bank approaches (i.e., wavelets) was used for clutter suppression using the phased linear array transducer for both transmission and reception [4]. In the present research we have also utilised the two-element transducer (annular array) and a pitch-catch set up with two different transducers, both having different centre frequencies. This exploits the fact that there are higher harmonics present in the transmitted signal, as described in Section 2.3, which results in a more broadband system than using the linear array. Therefore, by using this technique more information should be gained compared to the previous linear array measurements. In this section the signal processing efforts, performed on the new measurements, are described. In Section 2.4.3 an attempt to utilise the harmonic components are described, and in Section 2.4.5 the filter bank methods using wavelets from the previous report are continued [4]. We have also used traditional matched filters for detection of the artificial defects in the CAN1 block, which is described in Section 2.4.4. Since the weld clutter varies with depth it is reasonable to use a filter that also is depth dependent. This has also been implemented and is described in Section 2.4.8. Additional to clutter suppression/detection deconvolution (Wiener filtering) has been implemented to improve the time resolution, which is described in Section 2.4.9.

2.4.2 Ultrasonic Data

The investigations presented in this section have mainly been performed on US data from the CAN1 block. The reason is that this block is well documented and that it is easier to evaluate results from known defects, which are artificial flaws in the from of drilled holes in this case. Figure 2.34 shows a C-scan from a part of the CAN1 block containing flat bottom holes (FBH) and round bottom holes (RBH).

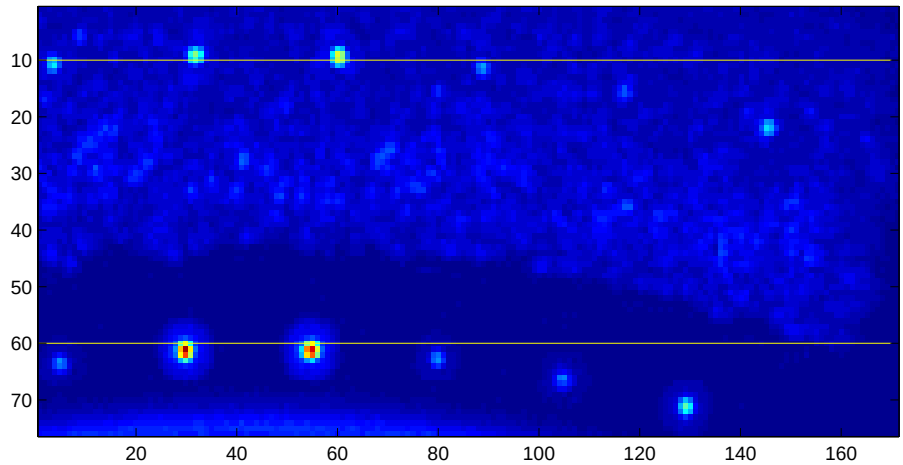

Figure 2.34. Original C-scan. The vertical (*y*) and horizontal (*x*) axes are both in mm.

The horizontal lines indicates two profiles in the C-scan, one inside the weld zone and one outside the weld zone, which is used later in this section when the different algorithms are evaluated.

2.4.3 Harmonic Filtering

The use of two transducers with different centre frequencies reveals that the transmitting transducer is generating a substantial amount of harmonic components outside the fundamental frequency range of the transducer. Thus, by using the measurement set up described in Section 2.2-2.3, a broad band system is obtained. In this subsection an attempt to utilise the harmonic components is made. The hypotheses is that the harmonic components contain the same information as the fundamental frequency band but with different noise properties. Thus, by using more frequency bands in the processing more information should be gained about the flaw signals resulting in an improved signal-to-noise ratio (SNR).

Using the hypotheses that the spectrum is harmonic it is reasonable to use a filter with similar characteristics for optimising the SNR. Here, we have utilised a filter with a Gaussian amplitude distribution in the frequency domain as a prototype and then ‘‘multiplied” the filter to the second and third harmonic. This filter has two parameters to tune: the centre frequency f_0 and the bandwidth B of the fundamental component. Figure 2.35 shows two examples of the Gaussian comb filter with different band widths and centre frequencies.

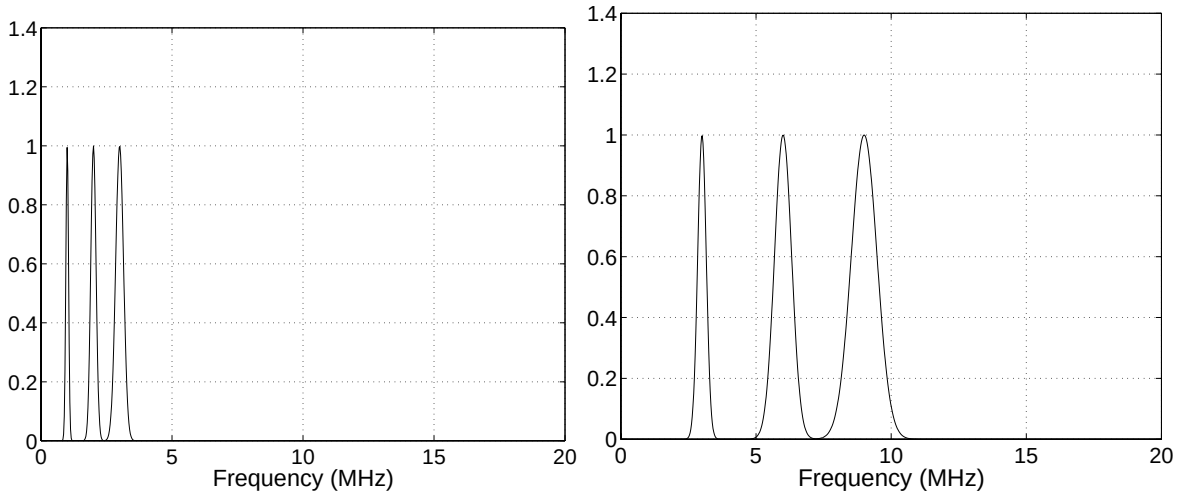

Figure 2.35. Two examples of the frequency response of the Gaussian comb filter.

The idea is then to tune the centre frequency and bandwidth to obtain processed data with an improved SNR. The filter tuning has been performed manually and the parameters were chosen to give the best

possible SNR. The result is shown in Figure 2.36 as a C-scan image and profiles selected as described above.

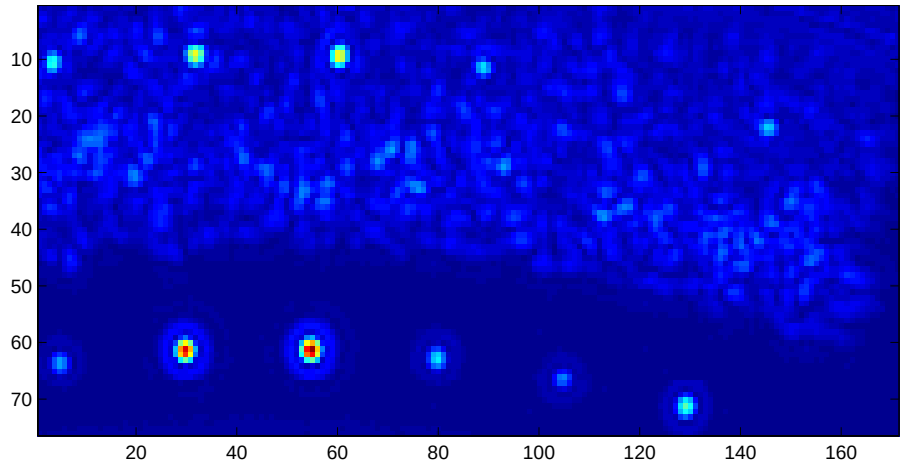

(a) C-scan. The vertical (y) and horizontal (x) axes are both in mm.

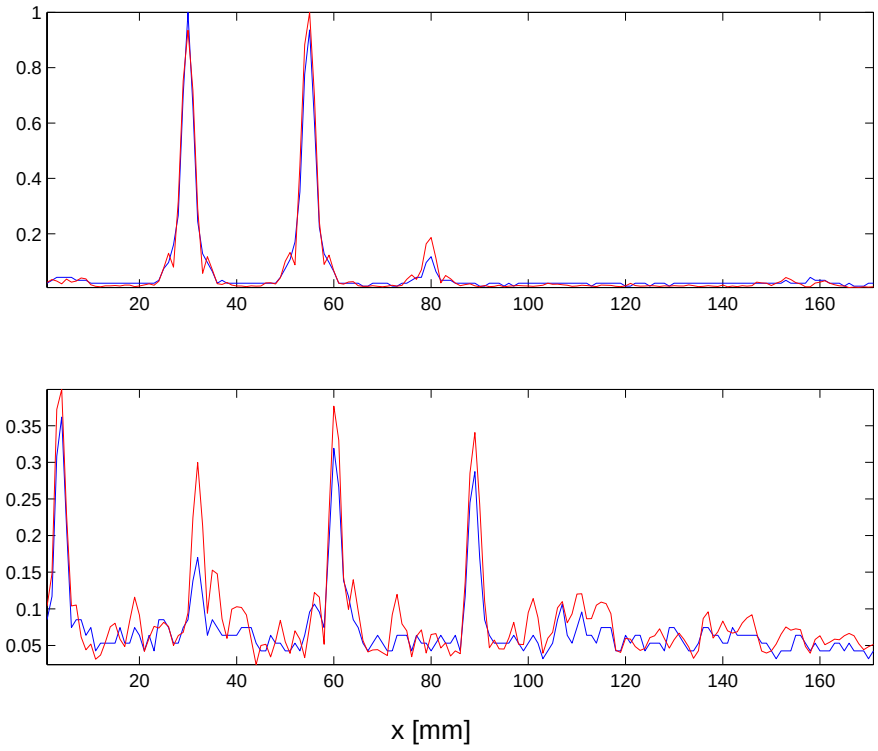

(b) Upper panel – outside the weld zone, lower panel – inside the weld zone.

Figure 2.36. (a) C-scan and (b) C-scan profiles from data filtered with a harmonic filter, blue – unprocessed, red – processed.

As one can see the performance gain, in terms of better SNR in the C-scan image, is rather limited.

2.4.4 Matched Filter Processing

If a known signal is to be detected in white Gaussian noise the optimal detector is simply a correlation between the known prototype $\mathbf{s}$ and the input vector $\mathbf{x}$ which is known as the *matched filter* [36,37]. If the noise (e.g. the weld clutter) is not white the matched filter can be generalised with the formula

$$\tilde{\mathbf{s}} = \mathbf{C}^{-1}\mathbf{s} \qquad (2.1)$$

where $\mathbf{C}$ is the noise covariance matrix [36]. The effect of $\mathbf{C}^{-1}$ is both whitening of the coloured noise and a compensation of the prototype $\mathbf{s}$ for the whitening. If the noise is white, that is, $\mathbf{C} = \delta^2\mathbf{I}$ the matched filter becomes $\tilde{\mathbf{s}} = \mathbf{s}/\delta^2$ where δ^2 is the noise variance. Note that if the noise variance is increasing the matched filter will become more restrictive (lower the gain) to avoid false alarms. The prototypes used here are simply responses from flat and round-bottomed holes in the unwelded region. The covariance matrix is estimated using the standard formula

$$\hat{\mathbf{C}} = \frac{1}{N-1}\sum_{n=1}^{N}\mathbf{x}_n\mathbf{x}_n^T \qquad (2.2)$$

where the $\mathbf{x}_n$ are measurements from regions in the weld zone not showing the presence of any defects (zero mean is assumed). The assumption that the prototype is known is somewhat unrealistic when real defects are considered, but it is used here to investigate the performance of the optimal detector when the defects are known (drilled holes). A more realistic assumption is to consider a family of transients rather than a fixed one. This can, for example, be implemented as a filter bank of matched filters.

Two experiments have been performed with the matched filter from data on the CAN1 bock, one with noise compensation and one without noise compensation. The prototype used was a FBH from the unwelded region. Figures 2.37 and 2.38 show the resulting C-scan images and profiles.

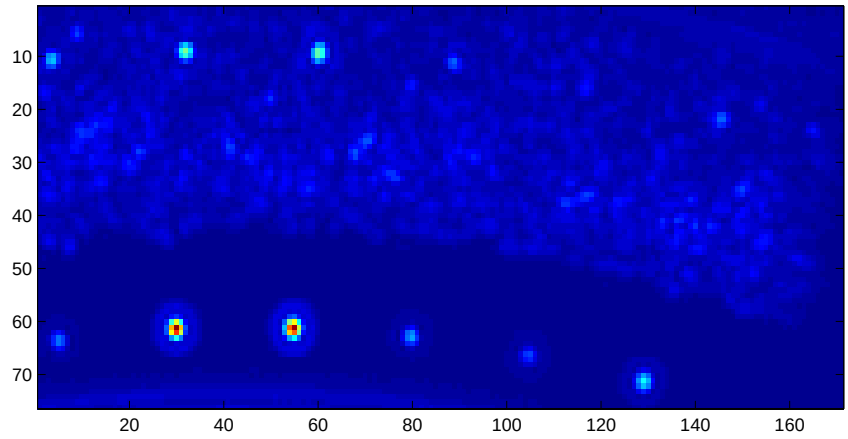

(a) C-scan. The vertical (*y*) and horizontal (*x*) axes are both in mm.

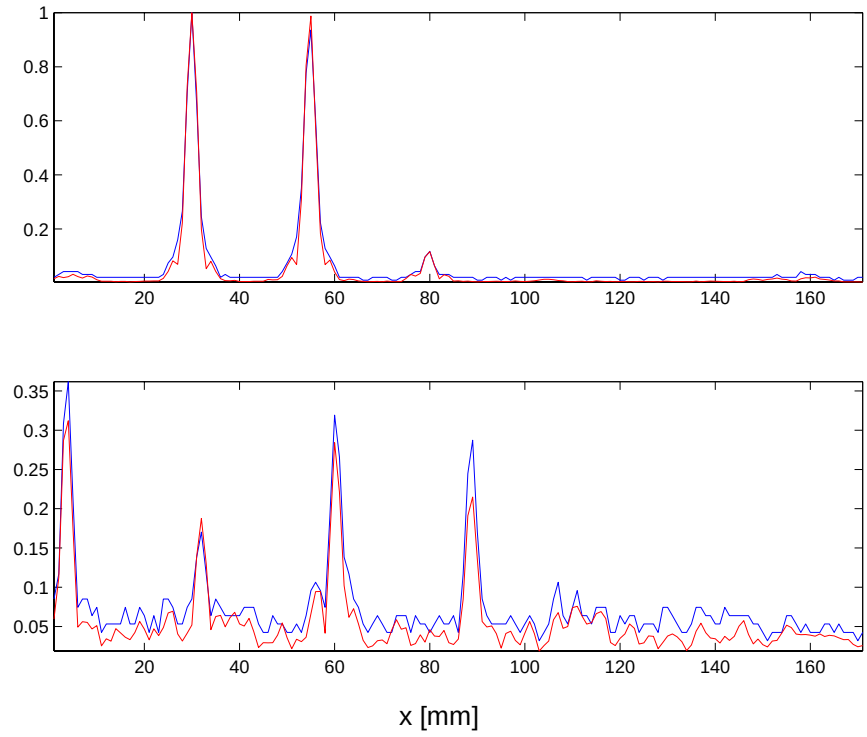

(b) Upper panel – outside the weld zone, lower panel – inside the weld zone.

Figure 2.37. (a) C-scan and (b) C-scan profiles from data filtered with the 1D uncompensated matched filter, blue – unprocessed, red – processed.

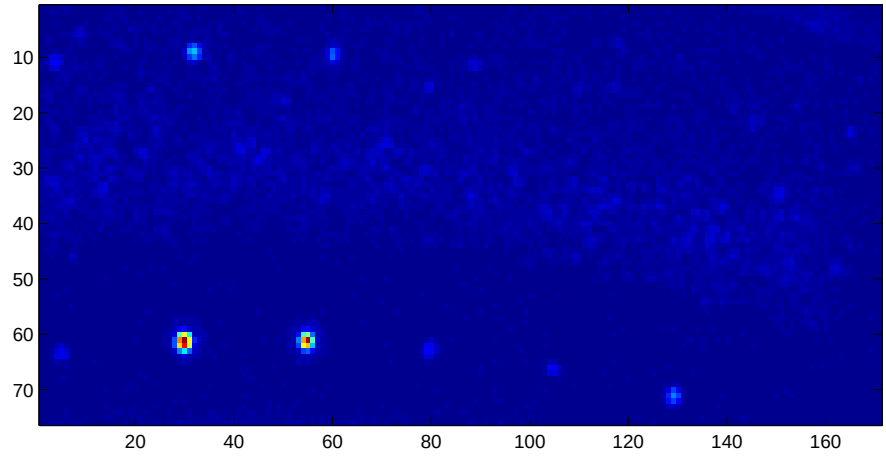

(a) C-scan. The vertical (*y*) and horizontal (*x*) axes are both in mm.

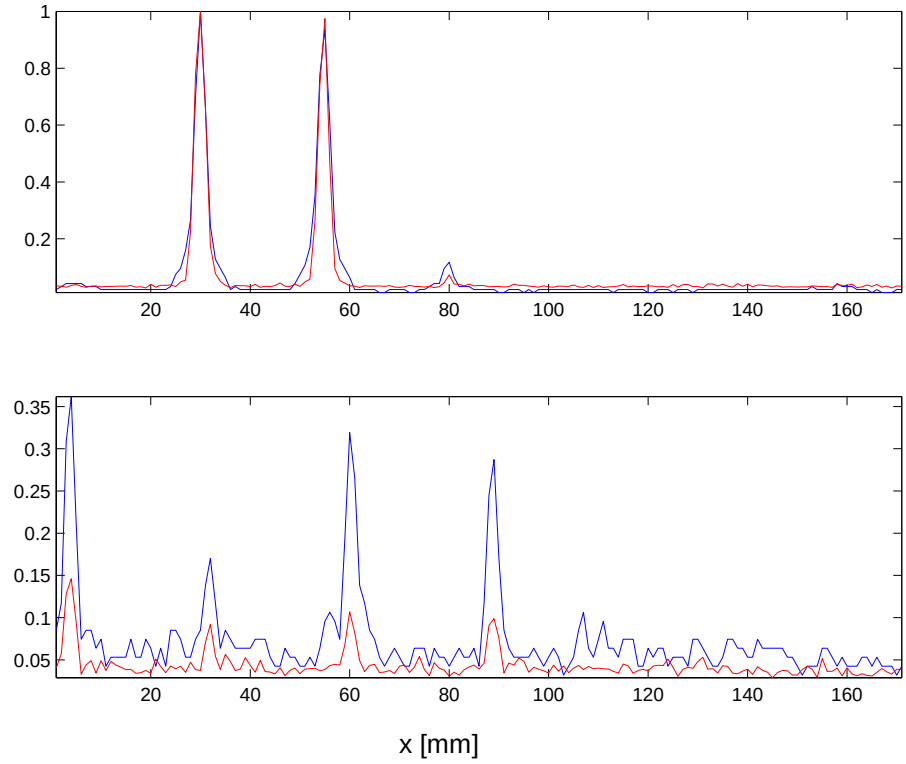

(b) Upper panel – outside the weld zone, lower panel – inside the weld zone.

Figure 2.38. (a) C-scan and (b) C-scan profiles from data filtered with the 1D noise compensated (generalized) matched filter, blue – unprocessed, red – processed.

One can see that the uncompensated matched filter has a similar performance as the harmoninc filter in the previous subsection, that is the SNR is rather unaffected by the filtering. The noise compensated matched filter has, though, lower gain in weld region (see the profiles in Figure 2.38(b)). The SNR in the weld region is, however, similar before and after the filtering. That is, both the clutter response and the FBH/RBH responses have been attenuated by the same amount in the weld region.

The rather poor performance of the matched filter can have several explanations. First, the prototype signal and the clutter signal may be too similar to be distinguished, and second, the

scattering in the weld zone acts as a filter that will change the response from defects in the weld zone. Since the weld is not a homogeneous medium the scattering effect is very difficult to compensate for.

The matched filter described above takes only temporal correlations into account. One can also extend the matched filter including spatial correlations as well to obtain a two or three dimensional matched filter in this way. The advantage of using higher dimensional matched filters is that, by also including spatial information, the detection performance can be improved. One drawback is that more filters are needed to take defects of different sizes into account.

A simple 2-D matched filter, was proposed for the filtering ultrasonic data in both temporal and spatial frequency domains simultaneously [23]. This means that the filter acts both as a band-pass filter (BP filter) extracting the respective harmonic component and also as a spatial filter suppressing the ultrasonic responses in directions other than those of the ones defined in the prototype. The matched 2-D filter requires a prototype, a small matrix that is used as a finite impulse response (FIR) 2-D filter. In our case this matrix is chosen by manually selecting a part of B-scan that is representing the interesting echoes. A B-scan from the block CAN1 was selected to illustrate performance of 2-D matched filter. A rectangular B-scan section corresponding to the response of the hole #11 (SDH) was used as a prototype for the filter (see Fig. 2.39). This matrix was first inverted with 180° and than convoluted with the processed B-scan using a 2-D convolution operation. To avoid artifacts the prototype can be windowed by an appropriate windowing function. The result of filtering is illustrated in Fig. 2.39. It is easy to see that the filter has suppressed the vertical lines and limited the spectrum (corresponding to the first harmonic in this case).

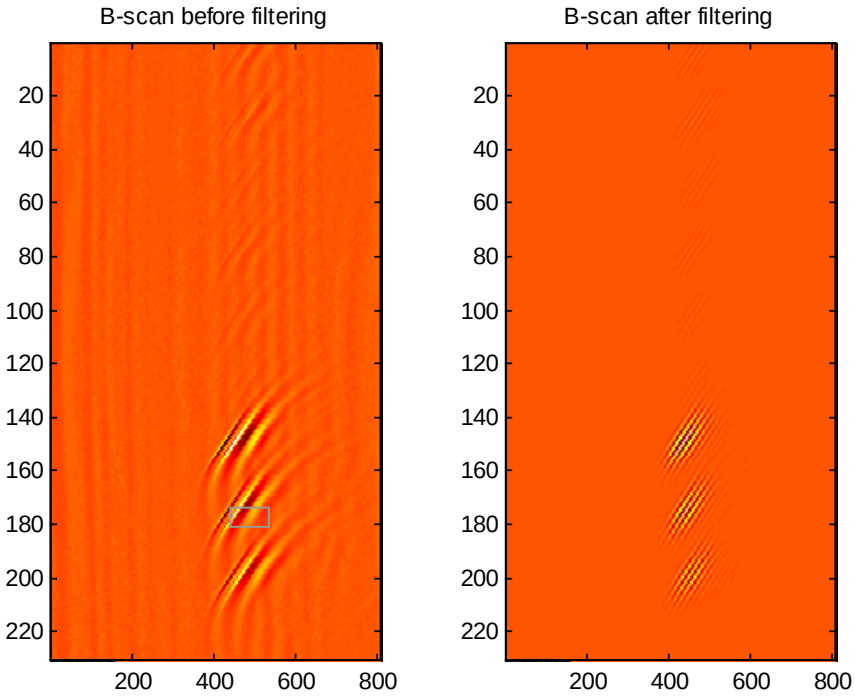

Figure 2.39. B-scan of the upper holes before (left panel) and after (right panel) 2-D matched filtering. The vertical axis is in mm, and the horizontal axis is in samples.

2.4.5 Wavelet Filtering

The wavelet filter, which previously was applied to data from the phased linear array, has also been applied to the new data from the two-element transducer. Preliminary, this filter showed a promising ability to suppress clutter in presence of (at least) strong scatterers using linear array data. The wavelet filter is simply a linear phase, FIR, band-pass filter shown in Figure 2.40.

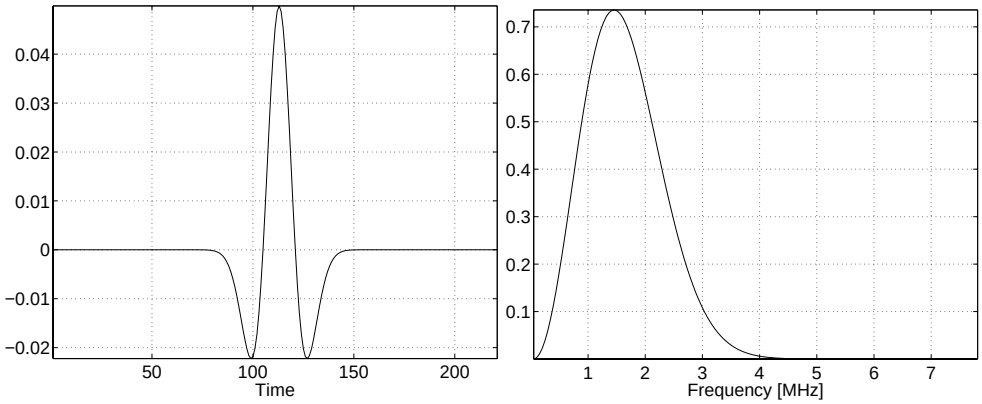

(a) Sombrero wavelet filter (b) Amplitude Spectrum

Figure 2.40. The wavelet filter.

The center frequency has been increased slightly comparing to the filter used on the linear array data in the previous report [4]. The scale (i.e. bandwidth) of the wavelet filter was chosen manually in a similar manner as the parameters for the harmonic filter. The performance is also similar to the harmonic filter with the difference that the gain for scattering in the weld zone is higher than for the harmonic filter (this depends of course of the chosen scale). The resulting SNR is however similar (see Fig 2.41).

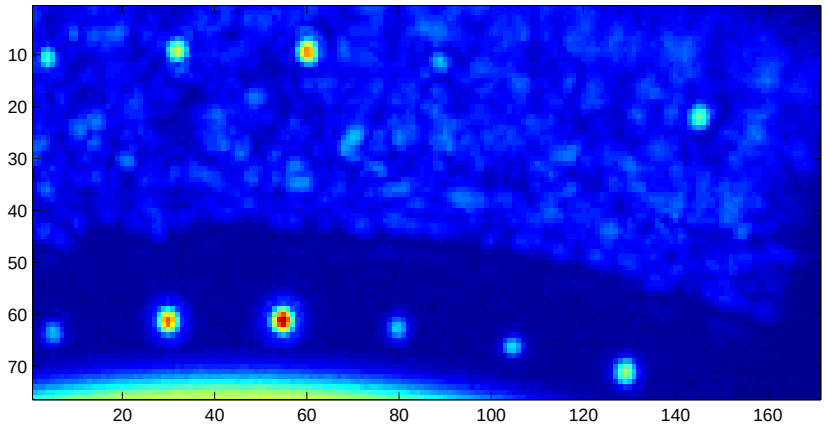

(a) C-scan image. The vertical (*y*) and horizontal (*x*) axes are both in mm.

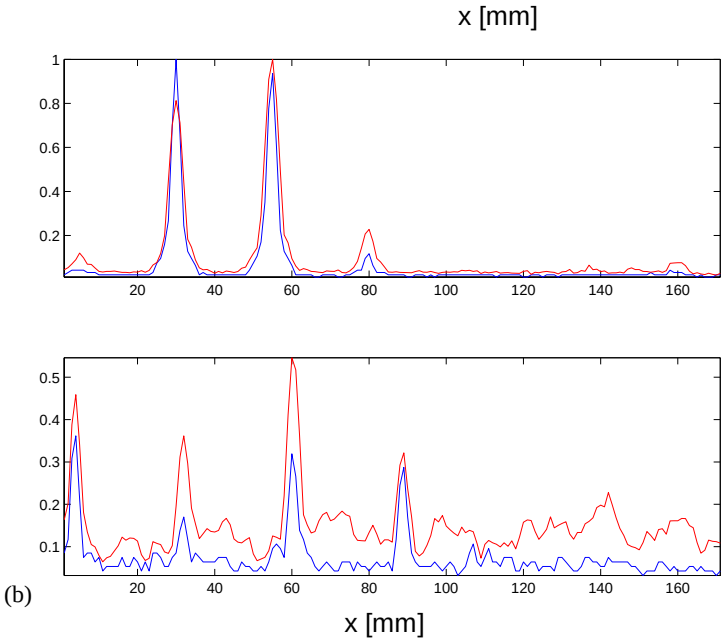

Figure 2.41. (a) C-scan and (b) C-scan profiles from data filtered with the wavelet filter, blue – unprocessed, red – processed.

2.4.6 Summary of Filtering Experiments

The filters discussed above all showed a similar performance. The gain in SNR is not substantial for any of the filters. All C-scans look rather similar to the original unprocessed C-scan shown in Figure 2.34. There may be several explanations for this behavior. Consider the following, our objective is to detect ultrasonic signals coming from defects in additive noise. Since defects vary in shape it does not seem feasible to assume a fixed prototype. However, it is reasonable to assume that the defects signals have common features, that is, they belong to the same family. The task is then to detect signals from the defect family in presence of noise, or clutter, which belongs to another signal family. Detection performance will, of course, be poor if the clutter family and the defect family

coincide or overlap. Another problem in this particular application is that the weld will change the response from defects in the weld zone due to scattering effects, that is the response from a FBH will to some extent look different in the weld compared to FBH:s outside the weld. The task becomes even more complicated since the scattering from the weld varies with both spatial position and depth. From our experiments appears that the matched filters with prototypes from SBH:s and FBH:s also respond strongly to weld clutter which indicates that the clutter and the artificial defect families may overlap.

2.4.7 Weld Clutter Properties

The theoretical results for the matched filter above are valid only if the clutter amplitude probability density is Gaussian. Gaussian nature of disturbances is usually assumed when little is known about the noise properties, and a matched filter is applied even though it may be sub-optimal. In order to examine the properties of the weld clutter further, histograms where taken at various depths in the weld from an ensemble of approximately 4000 A-scans. The mean back-scattered energy from the weld (i.e. the variance of the weld clutter histograms) is plotted in Figure 2.42 as a function of depth.

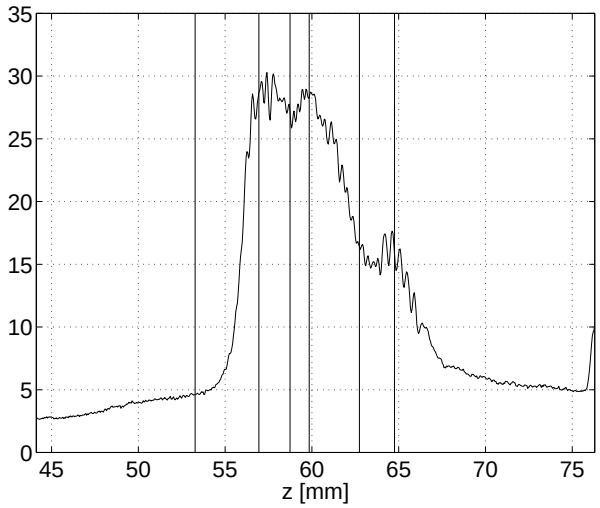

Figure 2.42. Mean back-scattered energy variance (variance) from the weld in the CAN1 block as a function of depth *z*.

Clearly, the back-scattered energy is non-stationary and very much dependent on depth. The five vertical lines in Figure 2.42 indicate the depths where the histograms, shown in Figure 2.43, are taken. The first line is in the heat affected zone (HAZ), the second in the top of the weld, the third is in its centre, the fourth is at the bottom of the weld, and finally, the last one corresponds to scattering from the wall-lid interface.

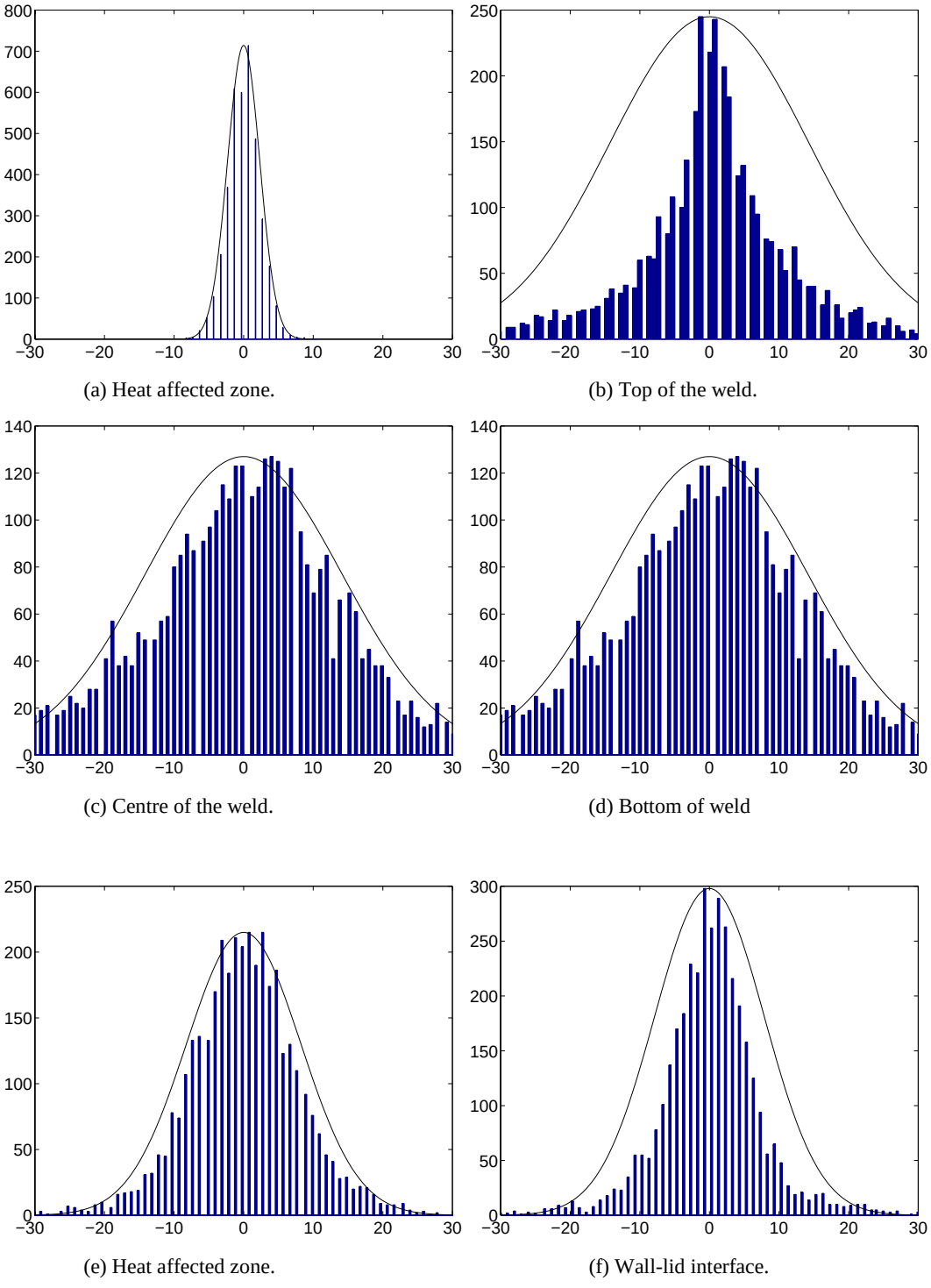

Figure 2.43. Histograms of weld clutter at different depths. Overlaid are also Gaussian bell functions with mean and variance estimated from the same data as the histogram. (a) HAZ, (b) top of the fusion zone (FZ), (c) centre of the FZ, (d) bottom of FZ, (e) HAZ, and (f) wall-lid interface. The horizontal axis is the amplitude and the vertical is the number of occurrences.

For reference Gaussian bell functions are overlaid in the histograms with mean and variances estimated from the same data as the histograms. Thus, if the histogram and the Gaussian bell functions match well the weld clutter fits a Gaussian distribution well, otherwise, the clutter belongs to some

other distribution. It can be seen the Gaussian assumption is a reasonable approximation in the heat affected zones and perhaps in the lover parts of the weld, but not in the upper parts. An explanation for this is that the grains in the fusion zone are relatively large and by using focused transducers we get very little averaging of scattering from different grains. The distributions in the lower parts of the weld are more Gaussian-like due to multiple scattering effects.

2.4.8 Non-stationary filtering

Since the distribution of the weld clutter varies strongly with depth it is reasonable to use different filters at different depths. One simple method of to accomplish this is to modify the (generalised) matched filter (2.1) by using a covariance matrix $\mathbf{C}_t$ which is a function of depth. This filter will still be sub-optimal since the clutter is not strictly Gaussian, but it should suppress the grain noise better than the corresponding stationary filter. Figure 2.44a shows a time frequency plot of the non-stationary matched filter impulse response. In Fig. 2.44b filter gain for four different frequencies is also shown as a function of depth (time). Note how the filter gain decreases in the fusion zone of the weld. That is, the filter becomes more “restrictive” in the fusion zone both for weld clutter and the prototype signal. The reason for this strong attenuation is probably that both the clutter and the prototype have very similar characteristics. Even though, this approach is optimal in a sense that the probability of detection is maximised subject to a fixed probability of false alarm, it is not suitable for our application. Since our main concern is detecting defects (voids) in the fusion zone it does not seem reasonable to attenuate all information there. One interpretation of the results is that the information in the 1D A-scan measurements is probably insufficient to distinguish between the two types of scatterers. This hypothesis is, however, not completely confirmed at this stage of the research.

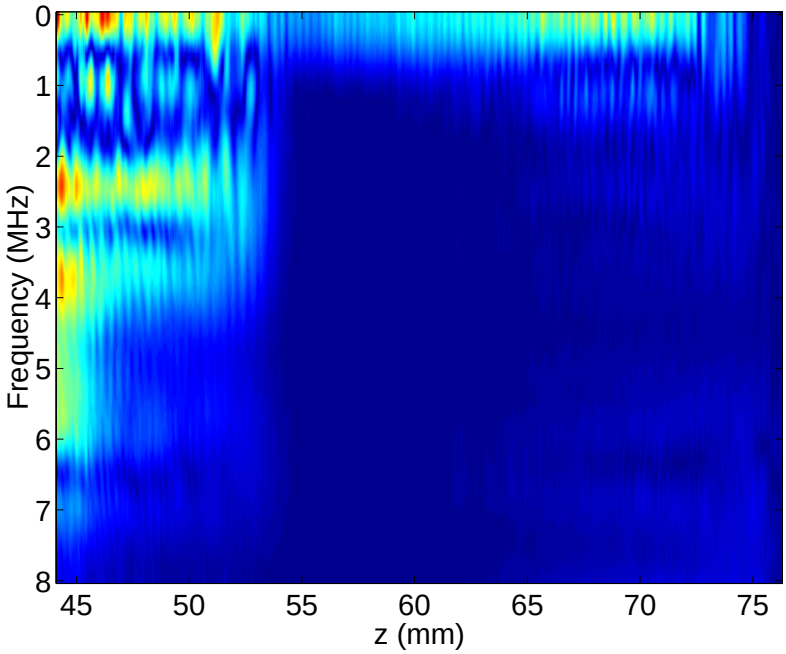

(a) Time-frequency plot.

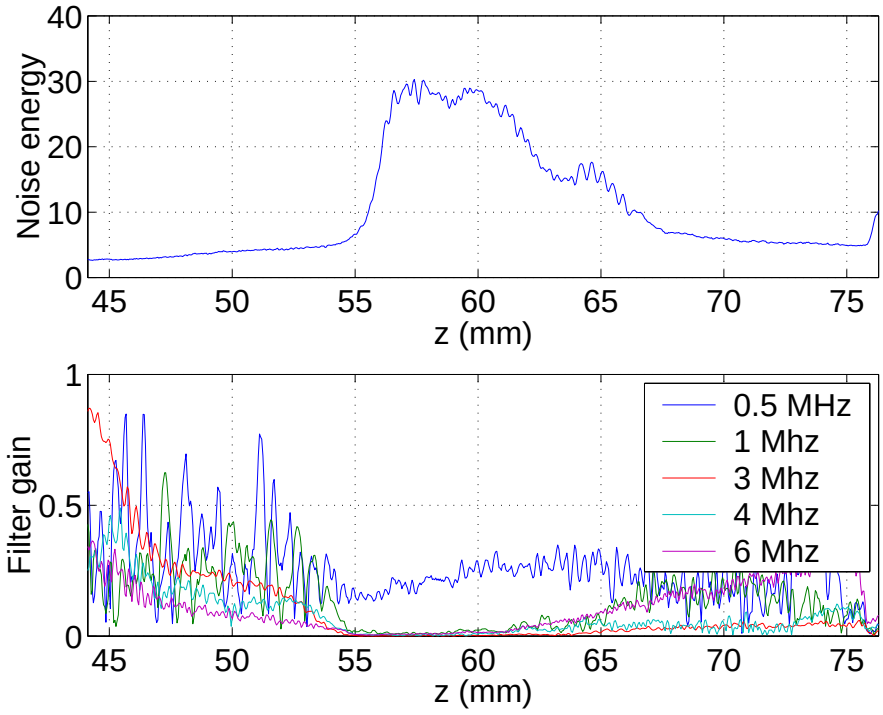

(b) Filter response for few frequencies as a function of depth.

Figure 2.44. Frequency response of the non-stationary matched filter as a function of depth. Fig. (a) shows the depth (time)-frequency plot and Fig. (b) shows the energy distribution as a function of depth in the upper plot and the filter gain for five different frequencies in the lower plot.

2.4.9 Enhancing temporal resolution

As can be seen from the results above the ultrasonic properties of the weld clutter and the properties of the artificial defects (FBH:s and RBH:s) seems very similar, at least if only one dimensional processing is considered. Due to this, for example, matched filters give similar output for clutter and artificial defects.[1] Another problem, which also makes ultrasonic examination more difficult, is that the measurement system (e.g. the transducer transfer function) smears out the ultrasonic responses. This can, however, be alleviated by means of inverse filtering of the ultrasonic data to remove, or at least decrease, the influence of the measurement system. The classical method for inverse filtering, or *deconvolution*, is the Wiener filter [35]. The following model is assumed for the measurements

$$\mathbf{x} = \mathbf{H}\mathbf{r} + \mathbf{n}\,. \qquad (2.3)$$

The matrix $\mathbf{H}$ is a Toeplitz matrix containing the system impulse responses, $\mathbf{r}$ is the so-called material signature (or material impulse response), and $\mathbf{n}$ is the measurement noise, which is assumed Gaussian. The minimum mean square estimator (MMSE) of $\mathbf{r}$, also known as the Wiener filter, is

$$\hat{\mathbf{r}} = \mathbf{C}_r\mathbf{H}^T(\mathbf{H}\mathbf{C}_r\mathbf{H}^T + \mathbf{C})^{-1}\mathbf{x} \qquad (2.4)$$

where, $\mathbf{C}_r$ is the covariance matrix of the material signature, and $\mathbf{C}_n$ is the covariance matrix of the measurement noise [35]. Both $\mathbf{r}$ and $\mathbf{n}$ are considered white, that is, the covariance matrices can be expressed as $\mathbf{C}_r = \delta_r^2\mathbf{I}$ and $\mathbf{C}_n = \delta_n^2\mathbf{I}$. Three measurement combinations has been performed with the two-element transducer: the 2.26 MHz element was used as both transmitter and receiver, the 4.83 MHz element was used as both transmitter and receiver, and the 2.26 MHz element was used as a transmitter and the 4.83 MHz element as a receiver. Thus, the three measurements differ in both centre frequency and bandwidth.[2] Figure 2.45 shows one A-scan before (upper panel) and after Wiener filtering (lower panel) containing weld clutter only, where the responses from a FBH has been used as the impulse responses in Eq. (2.3). The three A-scans have been taken as close to the same position as possible (which is determined by the mechanical tolerances of the ALLIN scanner). The corresponding impulse responses are shown in Figure 2.46.

[1] The clutter considered is from experimental data from the CAN1 block. We have considered the clutter to contain no real defects (voids). The radiographic examination did not reveal any such defects besides the artificial ones (see Section 1 in this report). However, radiographic examination is only sensitive to defects, which are aligned along the ray paths. ‘‘Flat defects” which are orientated perpendicular to the ray paths would not be seen in the radiograms. Hence, the strong reflections from the weld in the CAN1 block may, though not so probable, arise from flat voids aligned along the weld (perpendicular to the ray paths).

[2] Note also that the 2.26 MHz element has larger aperture than the 4.83 MHz element and is thus better focused.

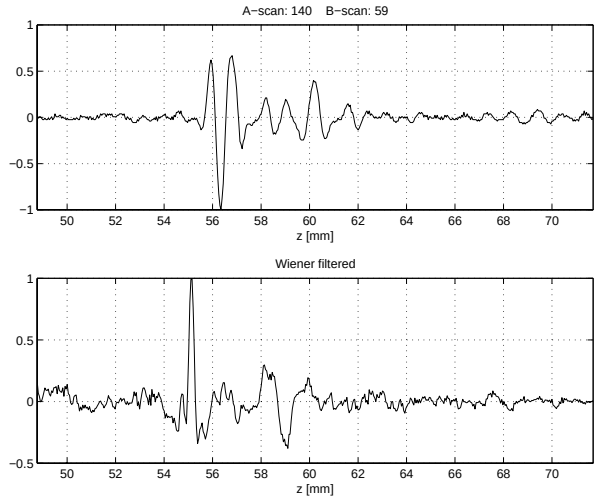

(a) 2.26 MHz Transmitter and receiver

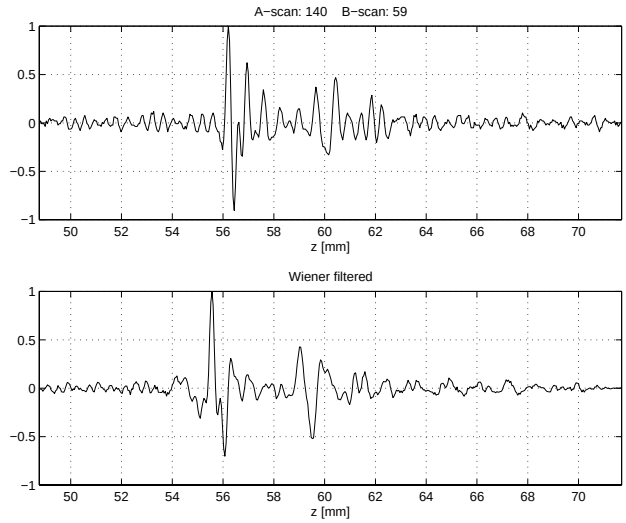

(b) 4.83 MHz Transmitter and receiver

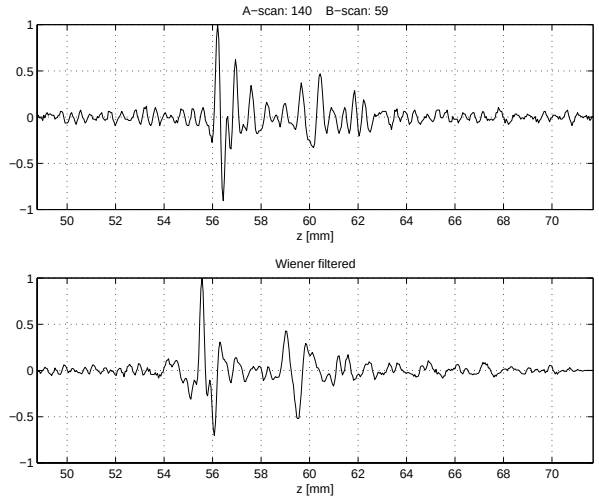

(c) 2.26 MHz Transmitter and 4.83 MHz receiver

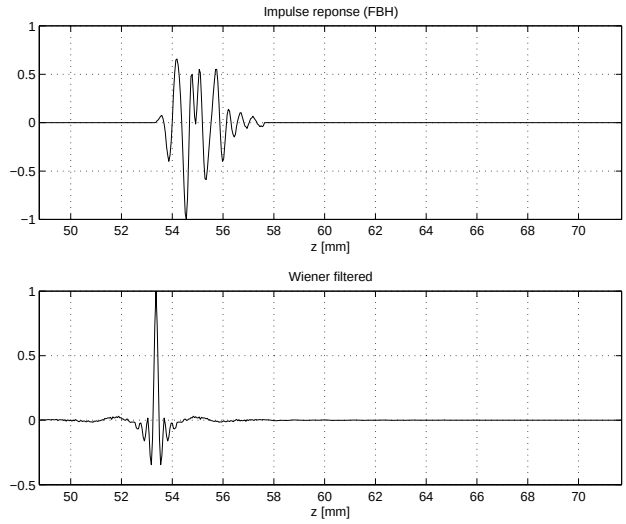

(c) FBH response deconvolved with 2.26 MHz - 4.83 MHz pair

Figure 2.45. A-scans from weld clutter using the two-element transducer taken at the same position in the CAN1 block.

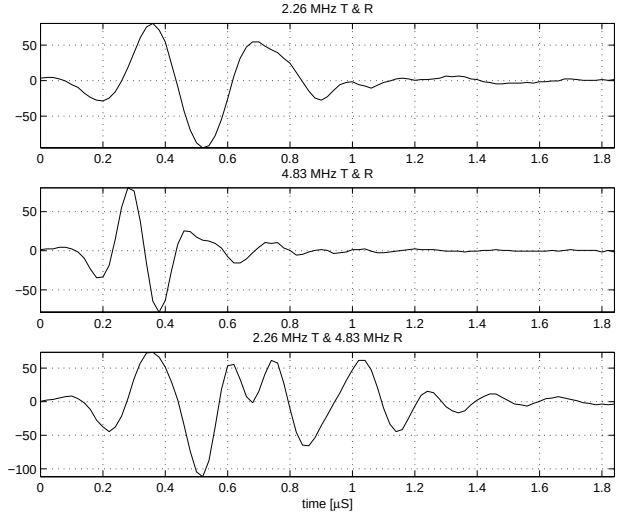

Figure 2.46. Responses from a FBH used as system impulse responses in the Wiener filter.

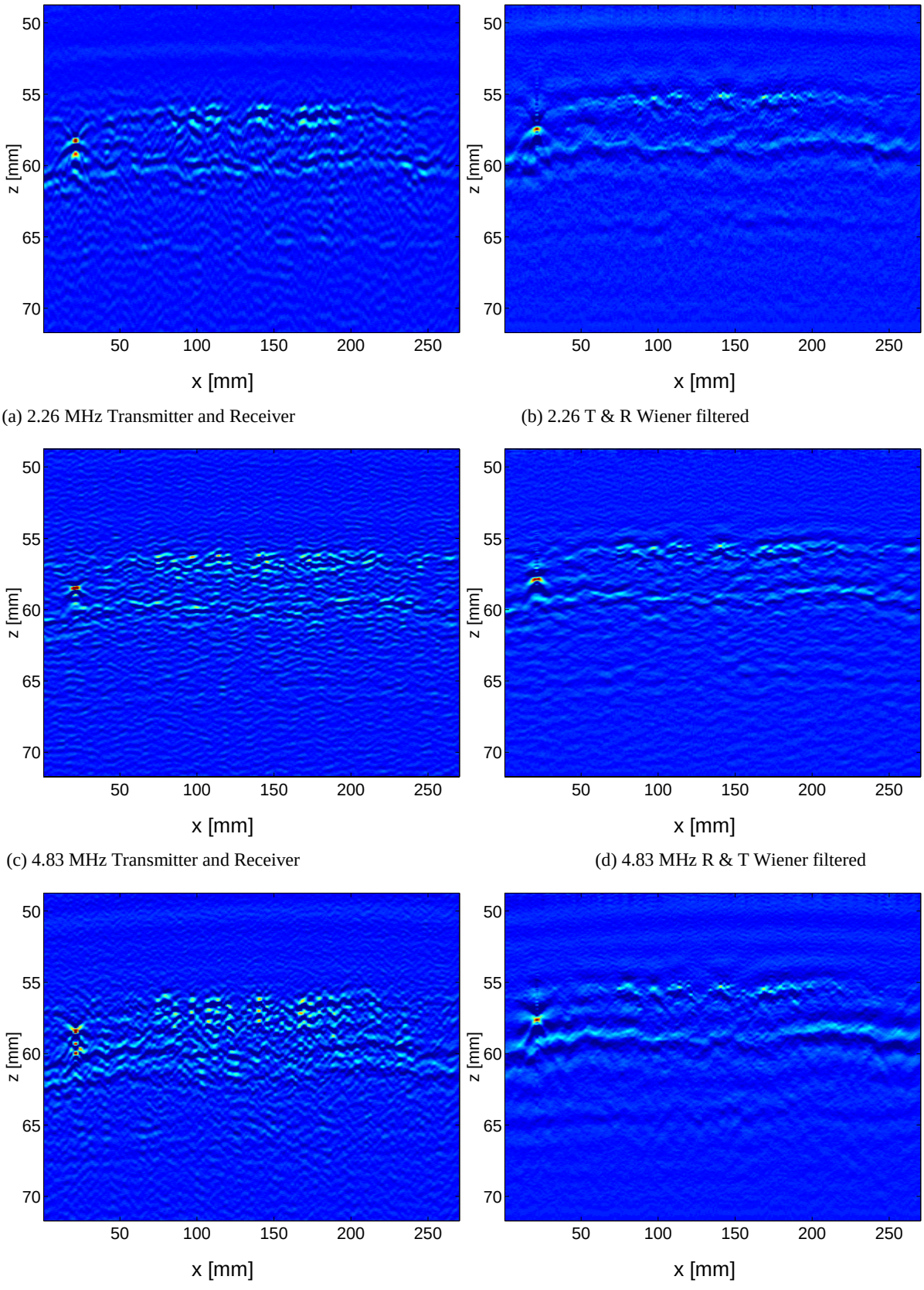

(a) 2.26 MHz Transmitter and Receiver

(b) 2.26 T & R Wiener filtered

(c) 4.83 MHz Transmitter and Receiver

(d) 4.83 MHz R & T Wiener filtered

(e) 2.26 MHz T, 4.83 MHz R

(f) 2.26 MHz T, 4.83 MHz R Wiener filtered

Figure. 2.47 B-scan images from the CAN1 block before (left column) and after Wiener filtering (right column). Note that the B-scans are taken perpendicular of the to the ones in Figure 2.6 (along the y-axis instead of the x-axis).

Note that the 2.26-4.83 MHz combination has the longest impulse response and, thus has the largest difference before and after processing with the Wiener filter. Examples of B-scan images of Wiener filtering are also shown in Figure 2.47.

The B-scans in Figure 2.47 also come from the CAN1 and they show mostly reflections from the weld structure. The response from one SDH is visible in the left part of the B-scans at approx. x =25, z=58 mm).

As can be seen from Figures 2.45 and 2.47 the resolution has been increased after Wiener filtering and different layers in the weld appears rather clearly. The 2.26-4.83 MHz pair results in the highest bandwidth which yields a "richer" frequency content also after deconvolution (i.e. sharper images), see Figure 2.45(c). The increased sharpness can be utilized, for example, in C-scan imaging. That is, after sharpening the US data by means of Wiener filtering, C-scans can be extracted at more distinct depths in the weld (i.e., resolution of the gate used for C-scan extraction can be increased) yielding more precise information about the location of scatterers. An illustration of the effect of Wiener filtering is shown in Figure 2.48. Here the mean energy of the A-scans is plotted as a function of depth both before and after processing.

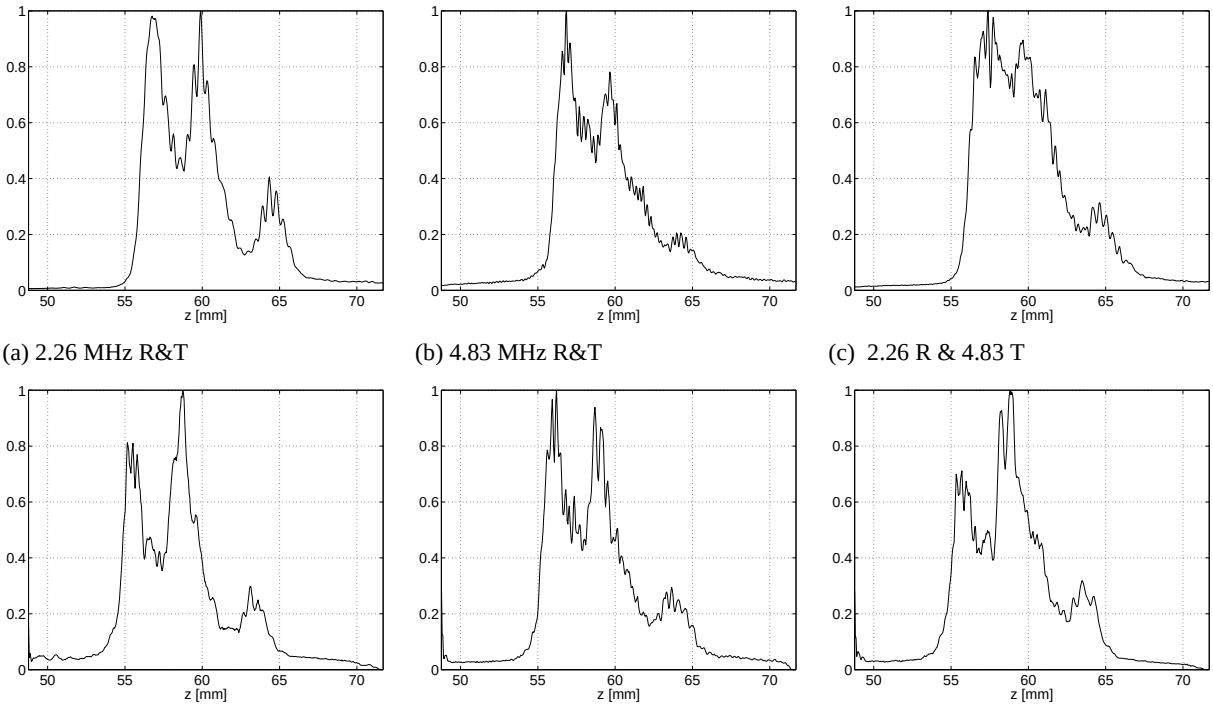

(a) 2.26 MHz R&T (b) 4.83 MHz R&T (c) 2.26 R & 4.83 T

(d) 2.26 MHz R&T Wiener (e) 4.83 MHz R&T Wiener (f) 2.26 R & 4.83 T Wiener

Figure 2.48. Mean A-scan energy (variance) as a function of depth. Responses from weld clutter from the CAN1 block, were used for averaging (the artificial defects has been excluded).

From Fig. 2.48 is clear that the largest energy difference is observed for the 2.26-4.83 MHz pair, and as it can be seen, the boundaries of the weld can be clearly distinguished as the two strong peaks in Figure 2.48 (d)-(f). This is due to the longest impulse response for this combination. The peaks from the weld boundaries should be even more distinct after processing but there will be some spread due mechanical errors (variations) both during welding and US inspection, as well as statistical variations of the grains in boundary zones of the weld.[3] This can be seen in the B-scans in Figure 2.47 above, where the "boundary lines" are not really straight horizontal lines (they are slightly curved). However, the boundaries are much better pronounced and easier to detect after Wiener filtering. One can also think of using an adaptive estimator to estimate the weld boundaries after Wiener filtering and use this information for setting adaptive gates when generating C-scans.

[3] The peak corresponding to the lower weld boundary will have some additionally spread due to multiple scattering as well.

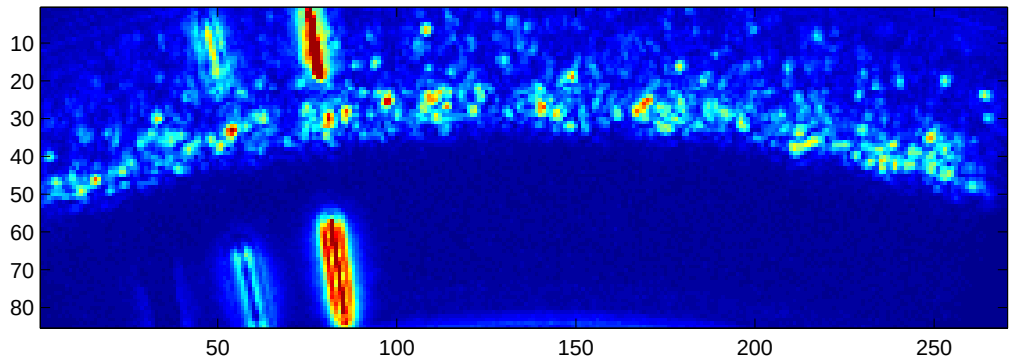

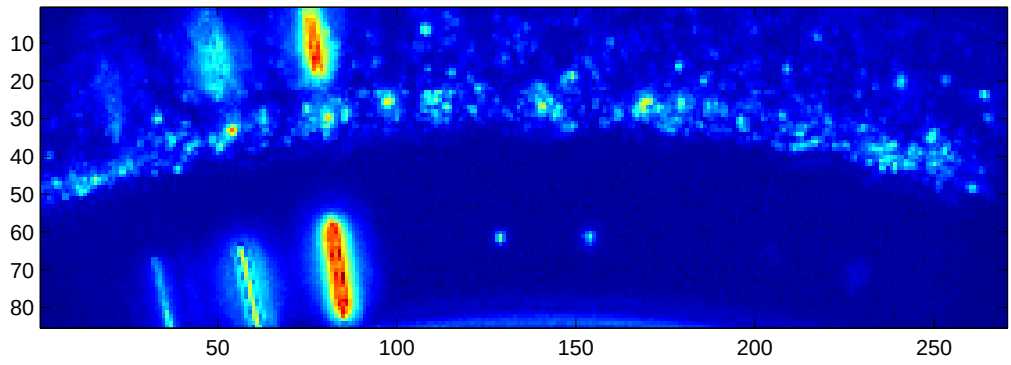

(a) C-scans from the top of the weld.

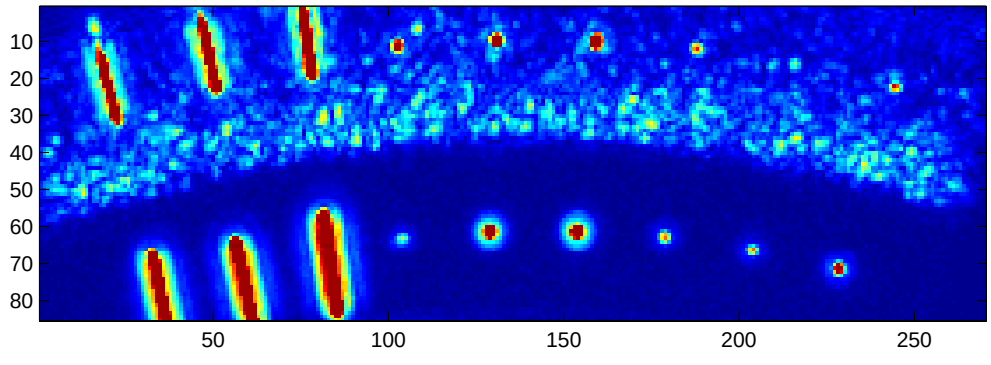

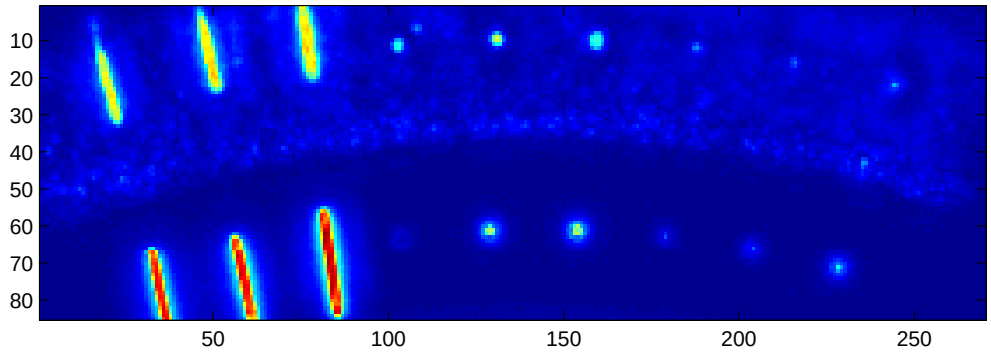

(b) C-scans from the middle part of the weld.

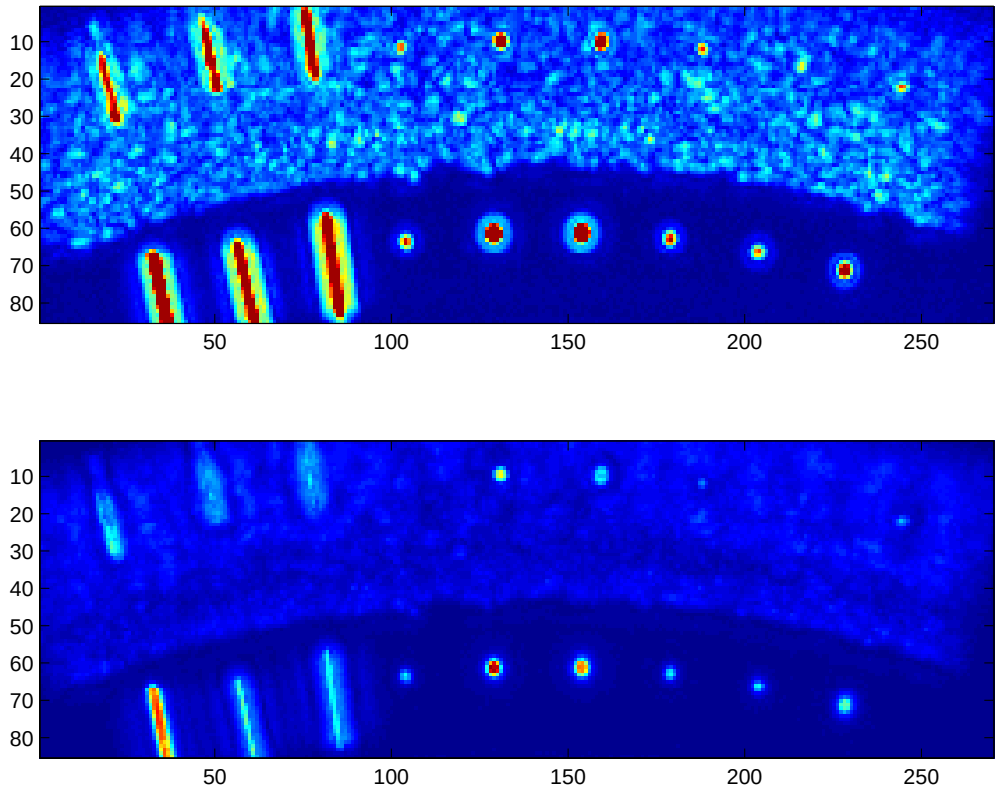

(c) C-scan from bottom of the weld.

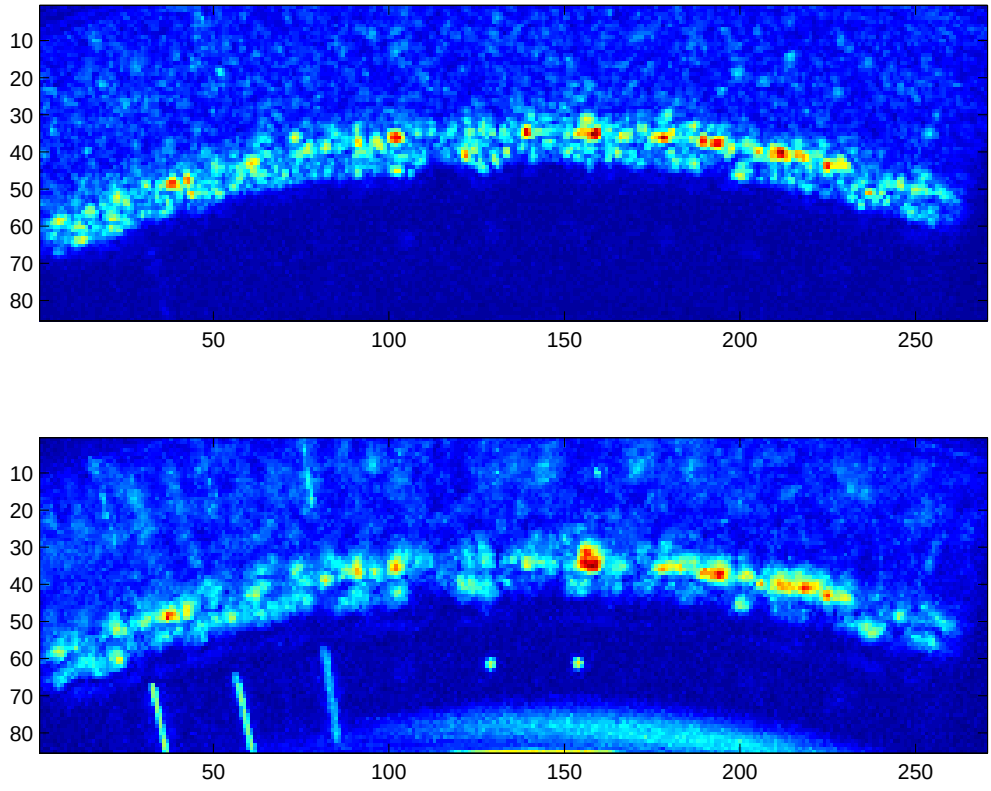

(d) C-scan from the wall-lid interface parts of the weld.

Figure 2.49. C-scans examples from the different parts of the weld before and after Wiener filtering in the CAN1 block using the 2.36-4.83 combination (upper panels – unprocessed, lower panels Wiener filtered). The vertical (*y*) and horizontal (*x*) axes are both in mm.

Four examples of C-scans are shown in Fig. 2.49. The same time-gates have been used for both the Wiener filtered and the unprocessed C-scans. Since the resolution has increased the weld clutter has decreased in some time-gates, which is perhaps most easily seen for the middle part of the fusion zone in Fig. 2.49(b).

The general conclusion from signal processing investigations is that it seems difficult to increase the SNR in C-scan imaging by means of filtering since the defect- and clutter responses seem very similar. The quality of the C-scans can however be improved by increasing the resolution, by means of Wiener filtering. By using this technique, more precise determination of the flaw depth is possible which is vital information for flaw characterization.

2.5 Conclusions

In this chapter, evaluation of EB welds has been presented. The evaluation was focused on three different aspects: ultrasonic properties of EB welds (such as scattering, sound velocity and attenuation), harmonic imaging of EB welds, and grain noise suppression aimed at flaw detection enhancement.

Scattering from EB weld has been investigated using three broadband, spherically focused transducers with different center frequencies, 2.26, 4.83, and 8.65 MHz. The study have shown that using transducers covering different successive frequency bands provides richer information on scattering and attenuation and thus yields better ultrasonic characterization of EB welds. The results indicate that the best frequency range for characterizing weld structure is between 2 and 5 MHz.

Two types of harmonic imaging of EB welds have been considered using different sources of harmonics. The first source, referred to as transducer harmonics, originates from the high-order resonant modes of transmitters excited by a broadband pulse. The second source, material harmonics, stems from the nonlinear distortion of waves propagating in materials.

In the study of transducer harmonic imaging, a broadband transducer with a higher center frequency received harmonics from a transducer with a low center frequency. The transducer harmonic imaging technique exploits additional information due to transducer harmonics. The results from the study show that the spatial resolution increases with the order of harmonic component, i.e., the higher order harmonic gives the better spatial resolution. The observed resolution improvement agrees with the theory since the higher harmonic components correspond to the shorter wavelengths.

The material harmonic imaging has been conducted in a systematical way. The tone burst for exciting the transmitter was first appropriately adjusted to guarantee that the fundamental resonant mode was excited and the higher resonant modes' excitations were limited to a very small level. Then harmonic generation has been made in water. Strong nonlinear waves in water have been observed and

the harmonics up to fifth order showed up. The experiments conducted in copper block have shown presence of harmonics up to fourth order. Finally, the harmonic generation was made in a copper canister CAN 1 with an EB weld. The harmonics up to third order from the EB weld have been clearly seen, and the fourth harmonic from some artificial defects were also visible. The ultrasonic images (C-scans) of the fundamental, and the higher harmonics have been extracted. From this preliminary experimental study, we can conclude that the spatial resolution becomes better and the grain noise pattern becomes finer for the higher-order harmonic image. Further exploration of nonlinear elastic waves and advancing the materials harmonic imaging technique for ultrasonic NDE seem be promising and stimulating, similarly as the tissue harmonic imaging technique in medical ultrasonography has resulted in significant improvement in image quality.

The signal processing investigations have been continued with the aim to refine ultrasonic imaging and to perform better clutter suppression. Various filters have been designed to improve detectabilty of defects in EB weld zones. Techniques such as standard matched filtering, wavelet filters and a special harmonic filter that utilizes harmonic components in ultrasonic signals have been investigated. A common requirement for success of these approaches is the presence of a significant difference in ultrasonic responses from defects (voids) and weld clutter. This means that spectral and/or phase difference between the signals due to detects and clutter should exist, otherwise detection is not possible. The results from the filtering experiments indicate that this is actually not the case. That is, it does not seem to be enough difference between the responses from artificial defects and welds to construct a good clutter suppression/detection algorithm of the form used here, and the gain in terms of signal-to-noise ratio is, therefore, not dramatic after processing. Note that this is specific to the measurement setup that is used here. If the measurement setup is changed the possibilities for clutter suppression may also change.

However, filtering had some positive effects, for example, applying 2-D matched filters to the images removed the unwanted, low frequency oscillations coming from the transmitter and smoothened the images. Even the C-scan image quality could be slightly improved without losing spatial resolution.

The time resolution is another important issue in US evaluation of EB welds. Poor resolution means that the US responses to different scatterers are smeared and, hence may overlap. This impairs the quality of, for example, C-scan imaging. Therefore, classical Wiener filtering has been implemented in order to remove, or at least decrease, the smearing that the measurement system induces. The results, after processing (or deconvolving) the US data with a Wiener filter, show a substantial improvement in temporal resolution. It is much easier to see the layered structure in the weld after processing, which eases the interpretation of the measured data. The C-scans extracted from the decovolved US data exhibit a significantly improved SNR. The improvement depends on the flaw location, the best success is observed for flaws located in the upper part of EB weld, above the strong scattering layer.

2.6 References

[1] T. Stepinski, and P. Wu, *Ultrasonic Inspection of Nuclear Fuel Copper Canisters,* SKB Projektrapport 97-01, December 1996.

[2] T. Stepinski, and P. Wu, *Inspection of Copper Canisters for Spent Nuclear Fuel by Means of Ultrasonic Array System,* SKB Projektrapport 97-06, Augusti 1997.

[3] P. Wu, and T. Stepinski, *Inspection of Copper Canisters for Spent Nuclear Fuel by Means of Ultrasonic Array System - Modelling, Defect Detection and Grain Noise Estimation,* SKB Technical Report TR-99-12, July 1998.

[4] P. Wu, Fredrik Lingvall, and T. Stepinski, *Inspection of Copper Canisters for Spent Nuclear Fuel by Means of Ultrasonic Array System – Electron Beam Evaluation, Modelling and Materials Characterization*, SKB Technical Report TR-99-43, December 1999.

[5] H. Schultz, *Electron Beam Welding* (Abington Publishing, Cambridge, 1993).

[6] E.P. DeGarmo, J.T. Black, and R. A. Kohser, *Materials and Processes in Manufacturing* (Macmillan Publishing Company, New York, 1990), 7th Edition, Chap. 36, p. 911-928, and Chap. 39, p. 951-961.

[7] J.F. Lancaster, *Metallurgy of Welding* (Chapman & Hall, London, 1993), 5th ed.

[8] K.R. Nightingale, A. Sanderson, J.M. Kell, C.R. Ribton, and A.B. Day, *Electron beam welding of copper canister lids in reduced pressure demonstration facility*, SKB Projektraport 96-01, April 1995.

[9] P. H. Chang, K. K. Shung, S.-J. Wu, and H. B. Levene, "Second harmonic imaging and harmonic Doppler measurements with Albunex®," *IEEE Trans. Ultrason. Ferroelec. Freq. Contr.*, vol. 42, no. 6, pp. 1020-1027, 1995.

[10] S. Krishnan, and M. O'Donnell, "Transmit aperture processing for nonlinear contrast agent imaging," *Ultrason.Imag.*, vol. 18, pp. 77-105, 1996.

[11] F. Forsberg, D. A. Mertom, J. B. Liu, L. Needleman and B. B. Goldberg, "Clinical applications of ultrasonic contrast agents," *Ultrasonics*, vol. 36, pp. 695-701, 1998.

[12] W. T. Shi, F. Forsberg, A. L. Hall, R. Y. Chiao, J. B. Liu, S. Miller, K. E. Thomenius, M. A. Wheatley, and B. B. Goldberg, "Subharmonic imaging with microbubble contrast agents: initial results," *Ultrason. Imaging*, vol. 21, no. 2, pp. 79-94, 1999.

[13] P. D. Krishna, P. M. Shankar and V. L. Newhouse, "Subharmonic generation from ultrasonic contrast agents," *Phys. Med. Biol.*, vol. 44, pp. 681-694, 1999.

[14] R. S. Shapiro, J, Wagreich, R. B. Parsons, A. Stancato-Pasik, H.-C. Yeh, and R. Lao, "Tissue harmonic imaging sonography," *AJR*, vol. 171, pp. 1203-1206, Nov. 1998.

[15] F. Tranquart, N. Grenier, V. Eder, and L. Pourcelot, "Clinical use of ultrasound tissue harmonic imaging," *Ultrasound in Med. & Biol.*, vol. 25, no.6, pp. 889-894, 1999.

[16] B. Ward, A. C. Baker, and V. F. Humphrey, "Nonlinear propagation applied to the improvement of resolution in diagnostic medical ultrasound," *J. Acoust. Soc. Amer.*, vol. 101, no. 1, pp. 143-154, 1997.

[17] T. Christopher, "Finite amplitude distribution-based inhomogeneous pulse echo ultrasonic imaging," *IEEE Trans. Ultrason. Ferroelec. Freq. Contr.*, vol. 44, no. 1, pp. 125-139, 1997.

[18] T. Christopher, "Experimental investigation of finite amplitude distribution-based, second harmonic pulse echo ultrasonic imaging," *IEEE Trans. Ultrason. Ferroelec. Freq. Contr.*, vol. 45, no. 1, pp. 158-162, 1998.

[19] P.-C. Li, "Pulse compression for finite amplitude distortion based harmonic imaging using coded waveforms," *Ultrason. Imaging*, vol. 21, no. 1, pp. 1-16, 1999.

[20] R. A. Smith, B. Zeqiri, L. D. Jones, and M. Hodnett, "Nonlinear propagation in water and its effect on ultrasonic C-scanning," *Insight*, vol. 40, no. 1, pp. 12-19, 1998.

[21] R. A. Smith, "Diffraction and nonlinear propagation in wide-band ultrasonic spectroscopy," *Insight*, vol. 41, no. 3, pp. 142-150, 1999.

[22] J. A. Slotwinski, "Measurement interpretation and uncertainty resulting from nonlinear ultrasonic wave propagation," *Res. Nondestr. Eval.*, vol. 11, pp. 213-234, 1999.

[23] T. Stepinski, and P. Wu, "Ultrasonic imaging of copper material using harmonic components," presented at *the 2nd International Conference on NDE in relation to Structural Integrity for Nuclear and Pressurized Components* in New Orleans, Louisiana, USA, May 24-26, 2000.

[24] M. A. Breazeale, and J. Ford, "Ultrasonic studies of the nonlinear behavior of solids," *J. Appl. Phys.*, vol. 36, pp. 3486-3490, 1965.

[25] M. A. Breazeale, "Ultrasonic studies of the nonlinear properties of solids," *Int J. Nondestr. Test.*, vol. 4, pp. 149-166, 1972.

[26] M. A. Breazeale, and J. Philip, "Determination of third-order elastic constants from ultrasonic harmonic generation measurements," *Phys. Acoust.*, vol. 17, pp. 1-60, 1984.

[27] I. Yu. Solodov, "Ultrasonics of non-linear contacts: propagation, reflection and NDE-applications," *Ultrasonics*, vol. 36, pp. 383-390, 1998.

[28] R. G. Maev, and I. Yu. Solodov, "Acoustic reflectivity enhancement using higher-order nonlinear reflection mode," in *1998 IEEE Ultrason. Symp.*, pp. 707-710, 1998.

[29] P. B. Nagy, "Fatigue damage assessment by nonlinear ultrasonic material characterization," *Ultrasonics*, vol. 36, pp. 375-381, 1998.

[30] K.-Y. Jhong, and K.-C. Kim, "Evaluation of material degradation using nonlinear acoustic effect," *Ultrasonics*, vol. 37, pp. 39-44, 1999.

[31] K.-Y. Jhong, "Application of nonlinear ultrasonics to the NDE of material degradation," *IEEE Trans. Ultrason. Ferroelectr.Freq. Contr.*, vol. 47, no. 3, pp. 540-548, 2000.

[32] S. I. Aanonsen, and T. Barkve, "Distortion and harmonic generation in the nearfield of a finite amplitude sound beam," *J. Acoust. Soc. Am.*, vol. 75, no. 3, pp. 749-768, 1984.

[33] M. A. Averkiou, and M. F. Hamilton, "Measurements of harmonic generation in a focused finite-amplitude sound beam," *J. Acoust. Soc. Am.*, vol. 98, no. 6, pp. 3439-3442, 1995.

[34] M. A. Averkiou, and M. F. Hamilton, "Nonlinear distortion of short pulses radiated by plane and focused circular pistons," *J. Acoust. Soc. Am.*, vol. 102, no. 5, pp. 2539-2548, 1997.

[35] S.M. Kay, "Fundamentals of Statistical Signal Processing Vol. I – Estimation Theory", 1993.

[36] S.M. Kay, "Fundamentals of Statistical Signal Processing Vol. II – Detection Theory", 1998.

[37] S. Haykin, "Adaptive Filter Theory", 2:nd ed., 1991.

3 Quantitative Evaluation of Attenuation in Copper

3.1 Introduction

Evaluation of attenuation is one of the important issues in materials characterization as well as in weld evaluation. In our previous work [1, 2], a method for quantitative evaluation of attenuation in solids had been developed for the ALLIN ultrasonic array. The quantitative evaluation was accomplished by determining the effective geometrical parameters for the array [3] and then correcting for the diffraction effects of the array. This procedure for quantitative evaluation of attenuation is applicable to not only arrays but also to transducers with different geometries (curved and planar), and, thus, it is rather general. The method used for calculating the diffraction was based on the model, the extended angular spectrum method (ASA) that was developed in our early work [3] and applicable to both curved and planar transducers. Due to the limited frequency bandwidth (nearly 60%) of the 3-MHz array, however, the frequency range of the attenuation evaluation was very limited. In the present work, we have extended the frequency range of the attenuation evaluation by using transducers with different center frequencies and covering different frequency ranges. To achieve the quantitative evaluation, the transducers have been calibrated, and the diffraction effects have been corrected. The whole work has been conducted in the following three tasks:

(i) characterization of spherically focused circular, and annular transducers,

(ii) modeling elastic fields radiated by the focused transducers into immersed copper,

(iii) evaluating attenuation in copper blocks using the transducers.

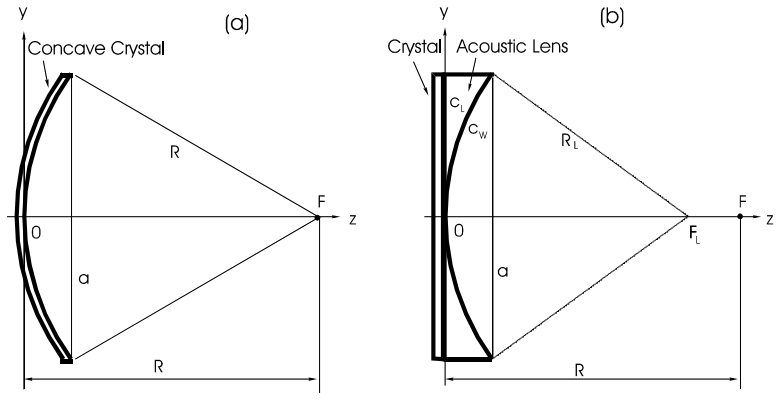

Fig. 3.1. Two types of the commonly used structures of the spherically focused transducers.

Spherically focused transducers are among the most commonly used transducers for focusing sound beams. Most often seen in practice are the structures of two types shown in Fig. 3.1. One is made up of a concave crystal (see Fig. 3.1(a)), and the other consists of a plane crystal coupled with

an plano-concave acoustic lens in front (see Fig. 3.1(b)). Originally, we intended to use three PANAMETRICS transducers (V392, V307 and V315) from our laboratory for the evaluation of attenuation. They have nominal center frequencies of 1, 5 and 10 MHz, and nominal diameters of 38, 25 and 19 mm, respectively. They are all spherically focused and the focal lengths, measured using steel ball targets in water were found to be, respectively, 190.0, and 191.1, and 181.3 mm. The 5 and 10-MHz transducers are of the latter type, as in Fig. 3.1(b). Unfortunately, the structure and some important transducer parameters necessary for our model (like sound speed and shape: spherical or parabolic, and radius of curvature if it is spherical of the lenses) are proprietary, and thus not available. Therefore, we used instead a spherically focused two-element transducer that had been designed and used for material harmonic imaging (see Chap. 2 of this report). The outer and inner elements have different center frequencies, namely, 2.26 and 4.83 MHz, respectively. This means that the focused transducers of the first type are of our interest (Fig. 3.1(a)).

Various theories for calculating the radiations from spherically concave transducers have been developed since 1940s [4, 5], and based on these theories a number of methods for characterizing transducers from measurements have also been established. A large amount of literature is available concerning the theories (see [4–10] and also the references in [2, 3]) but quite a few references is concerned with the characterization methods [11-14, 3]. Comprehensive reviews of the literature on the theories and methods have been made in our recent reports, [2] and [3]. However, since the existing characterization methods (cf. [11-14]) are developed in frequency domain (for continuous wave) their implementation requires optimization of experimental procedures (see [12-13]). In the present work, we have proposed a new method for characterizing spherically focused transducers. The characterizing method is based on the spatial impulse response method, and thus implemented in pulse mode, i.e., in time domain. Although the method is proposed for the case of spherically focused transducers, it is also applicable to other transducers of different geometries, both curved and planar, such as cylindrically-concave, planar-circular, and planar-rectangular transducers. Simplicity is the main advantage of the proposed method comparing to the others, known from literature.

After the transducer characterization, elastic waves in immersed solids have been calculated based on the extended angular spectrum approach in [3]. Since the transducers are axisymmetric, the fields need be calculated in two dimensions only. However, the transducers are curved and the Hankel transform does not apply (it is only usable for planar transducers with axisymmetry or for one-dimensional transducers). The idea of the extended angular spectrum approach in [3] has been employed in the present work, and a new algorithm with increased efficiency has been developed for calculating angular spectra of such transducers. Elastic fields in copper block immersed in water were computed using a procedure as proposed earlier in [3, 2].

Experimentally evaluated transducer parameters and simulated elastic fields in the immersed copper block were used for calculating pulse echoes from the front and back surfaces of the solid.

Finally, attenuation of the solid was evaluated with the log spectral difference method, presented in our recent report [2].

3.2 Characterization of spherically focused transducers

It is well known that the geometric parameters, e.g., radius (or diameter) and focal length, of a transducer given in a specification are just nominal, and they result in some error when they are used in a theory of calculating acoustic fields [3, 11-15]. Therefore, determination of the effective geometric parameters of a transducer, referred to as transducer characterization [14], is required for obtaining accurate calculated results that fit the measured results. The number of geometric parameters specifying a transducer varies with the transducer' geometry. For a planar circular transducer, one parameter, i.e., radius, needs to be characterized [15]. For a spherical circular transducer, two parameters: radius and focal length (or radius of curvature) are to be characterized [11-14]. For a spherical annular transducer, three parameters, inner and outer radii and focal length, are to be characterized. A characterization method is established based on a certain theory of acoustic calculation. The theory used in the present work is the spatial impulse response method, which is one of the commonly-used theories for acoustic calculations [6-9, 20] and has been verified for curved transducers both numerically [10] and experimentally [16-20].

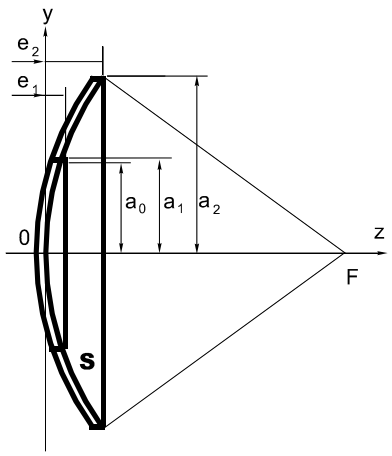

Fig. 3.2. Geometry of the spherically focused transducer with two concentric elements.

3.2.1 Characterization method and its theory

We will characterize a two-element annular array transducer, shown in Fig. 3.2. It consists of two concentric elements with radius of curvature of 210 mm (that is the focal length, denoted by *F* in the figure). The inner element is spherically circular with a 10-mm radius (denoted by a_0), and the outer

is spherically annular with a 10-mm inner radius (represented by a_1, with negligence of the gap between the elements) and a 19-mm outer radius (represented by a_2). The outer and inner elements have the center frequencies of 2.26 and 4.83 MHz, respectively.

The method for characterizing such transducers is established based on the spatial impulse response method (SIRM). Pressure field $p(\mathbf{r}, t)$ at any point $\mathbf{r}$ is calculated using SIRM by convolving the normal velocity $v_n(t)$ on a transducer surface with the derivative of the transducer's spatial impulse response (SIR) $h(\mathbf{r}, t)$ [20],

$$p(\mathbf{r},t) = \rho_0 v_n(t) * \frac{\partial h(\mathbf{r},t)}{\partial t} = v_n(t) * h_p(\mathbf{r},t), \tag{3.1}$$

where ρ_0 is the density of the medium,

$$h_p(\mathbf{r},t) = \rho_0 \frac{\partial h(\mathbf{r},t)}{\partial t}, \tag{3.2}$$

which is usually referred to as the pressure spatial impulse response.

In pulse-echo mode (echo from a point scatterer) the output of a transducer can be calculated by [20]

$$V(t) = V_0 v_n(t) * h_p(\mathbf{r},t) * h_p(\mathbf{r},t) = V_0 v_n(t) * h_{pe}(\mathbf{r},t) \tag{3.3}$$

where V_0 is a proportional constant, and

$$h_{pe}(\mathbf{r},t) = h_p(\mathbf{r},t) * h_p(\mathbf{r},t) \tag{3.4}$$

is called echo pressure SIR.

For both spherically circular [6-8] and spherically annular transducers [7], their SIRs are available in analytic form that is given in Appendix 3-A.

To work out the characterization method for the spherically circular and annular transducers, we first look at the procedure of the SIRM for calculating a pulse echo from a point scatterer for the transducers of both types, respectively. For this study, the coordinates are arranged in such a way that the *z*-axis is just coincident with the transducer's axis and the *y*-axis is in the radial direction of the transducer (Fig. 3.2). The point scatter is positioned on the axis at *z* = 40 mm.

In the case of a spherically circular transducer with a 4.83-MHz center frequency, we obtained a normal velocity pulse $v_n(t)$ on the transducer surface from a measurement (Fig. 3.3(a)). The duration of the pulse is 0.87 μs. The SIR $h(\mathbf{r}, t)$ can be calculated analytically (see Appendix 3-A), and at the position, y=0 and z=40 mm, and with the nominal radius (10 mm) and focal length (210 mm). The calculated SIR is shown in Fig. 3.3(b). $h(\mathbf{r}, t)$ is rectangular, starting from t_0 (=26.936 μs) and ending at t_1 (=27.609 μs), which makes $t_1 - t_0$ =0.673 μs.

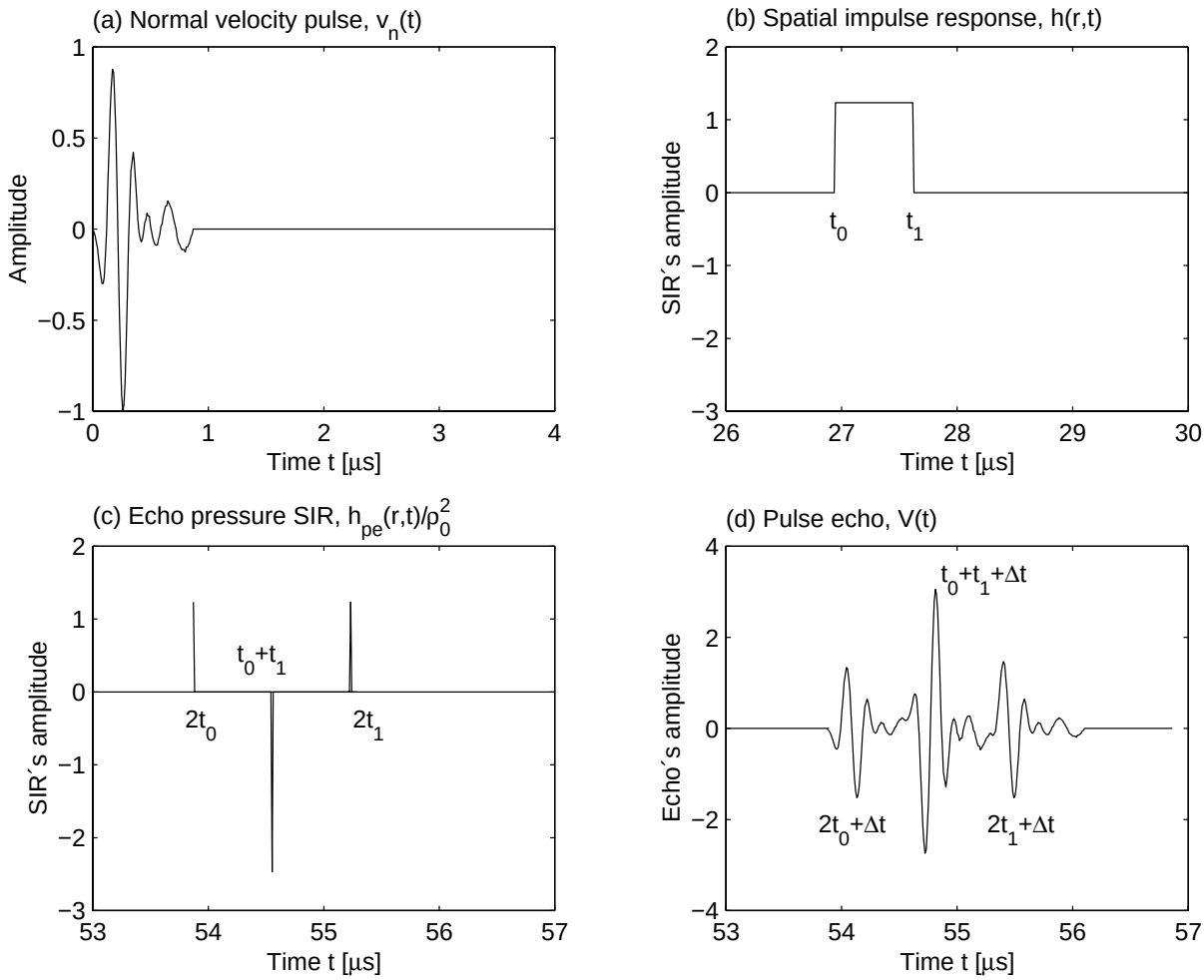

Fig. 3.3. (a) The normal velocity pulse on the spherically circular transducer, (b) the spatial impulse response (SIR) on the axis at z=40 mm, (c) the echo pressure SIR, and (d) the output of the transducer, the pulse-echo from the point scatterer.

The time instants t_0 and t_1 are calculated in the following manner (see Appendix 3-A)

$$t_0 = z/c\,, \tag{3.5a}$$

$$t_1 = \sqrt{a^2 + (z-e)^2}\,/c\,, \tag{3.5b}$$

where

$$e = F - \sqrt{F^2 - a^2} \ . \qquad (3.6).$$

At t_0 and t_1 where the derivatives of $h(\mathbf{r}, t)$ are two pulses (two $\delta(t)$ functions) with the same amplitude. In the forward field radiated by the transducer, the first one is positive and results in the direct wave, and the second is negative (the inverted replica of the first) and results in the edge wave.

The echo pressure SIR $h_{pe}(\mathbf{r},t)$ can be further obtained by convolution (Eq. (3.4)), as displayed in Fig. 3.3(c). Unlike $h(\mathbf{r}, t)$, $h_{pe}(\mathbf{r},t)$ has three spikes, three $\delta(t)$'s at time instants $2t_0$, t_0+t_1 and $2t_1$, which are separated by the time difference of $(t_1 - t_0)$. The first impulse $\delta_1(t)$ is the echo impulse of the direct wave, the second $\delta_2(t)$ with two times as large amplitude as $\delta_1(t)$ and a time delay $(t_1 - t_0)$ is the inverted replica of the first one, and the third impulse $\delta_3(t)$ with the same amplitude as $\delta_1(t)$ and a time delay $2(t_1 - t_0)$ is just the replica of the first one. The output of the transducer, a pulse echo from the point scatterer, is proportional to the result of convolution of the normal velocity pulse $v_n(t)$ with the echo pressure SIR $h_{pe}(\mathbf{r},t)$ (c.f., Eq. (3.3)), and shown in Fig. 3.3(d). The three pulses in the received signal $V(t)$ start at time instants $2t_0$, t_0+t_1 and $2t_1$, respectively. Since $t_1 - t_0 = 0.673\ \mu s$ is smaller than $0.87\ \mu s$, the pulse duration of the normal velocity $v_n(t)$, the starting instants of the second and third pulses overlap with the ending instants of the second and third pulses. Therefore, the two time instants, t_0+t_1 and $2t_1$ cannot be distinguished from this received signal $V(t)$ of the transducer. However, if all three time instants are measured with a time delay Δt (e.g., at the second negative peaks of the first and third pulses and the second positive peak of the second pulse) then the first and second pulses do not overlap with the second and third one, respectively, at the delayed instants ($t_0 + t_1 + \Delta t$ and $2t_1 + \Delta t$). Therefore, the time differences of the three successively measured instants ($2t_0 + \Delta t$, $t_0 + t_1 + \Delta t$ and $2t_1 + \Delta t$) are the same, that is $t_1 - t_0 = \Delta t_{10}$.

Based on the above analysis, we can now develop a method for characterizing spherically circular transducers. Making a measurement in such a way that the transducer and the point scatterer are put close enough and on the axis, we can, from the measurement, obtain a time difference Δt_{10} equal to the time separations of the spikes of the echo pressure SIR $h_{pe}(\mathbf{r},t)$. Then from Eq. (3.5) we have

$$\Delta t_{10} = t_1 - t_0 = \left(\sqrt{a^2 + (z-e)^2} - z \right) \Big/ c \ . \qquad (3.7)$$

Since two parameters, *a* and *F*, are to be determined, we need two measurements at two distances. Assuming that the two time differences Δt_{10}^{I} and Δt_{10}^{II} are obtained from two measurements at z_I and z_{II}, then we can determine the effective radius and focal length,

$$a_{eff} = \sqrt{\left(c\Delta t_{10}^{I} + z_I\right)^2 - (z_I - e)^2}\,, \tag{3.8}$$

$$F_{eff} = \left(a_{eff}^2 + e^2\right)\big/2e\,, \tag{3.9}$$

where

$$e = \frac{\left(c\Delta t_{10}^{I}\right)^2 - \left(c\Delta t_{10}^{II}\right)^2 + 2c\left(\Delta t_{10}^{I} z_I - \Delta t_{10}^{II} z_{II}\right)}{2\left(z_{II} - z_I\right)}. \tag{3.10}$$

Two approaches can be used to measure the time difference. The first approach consists in direct measuring corresponding peaks of the pulses. For example, in Fig. 3.3, the second negative peaks of the first and third pulses, and the second positive peak of the second pulse. The time difference between the first and the second pulses and the one between the second and third pulses are identical, i.e., $t_1 + t_0$. The second approach is to shift the traces of the same pulse echo signal; when the first pulse is completely overlapped with second one, we obtain the time difference between the first and second pulse; and when the second is completely overlapped with the third, we get the time difference between the second and third pulses. In comparison, the first approach is simple and straightforward but vulnerable to noise, and the second approach needs a little more manipulation, but is more accurate and much less sensitive to noise influence.

To characterize a spherically annular transducer, we have to determine three geometrical parameters, inner and outer radii, and focal length. Using a similar way, we obtain procedure of the SIRM for calculating a pulse echo from a point scatterer for the annular transducer, shown in Fig. 3.4. The annular transducer has the lower center frequency and thus the fundamental frequency of its normal velocity pulse 2.26 MHz (Fig. 3.4(a)). The pulse duration is 1.74 μs. In the forward field from an annular transducer there is no direct wave present but there are two edge waves from the edges of the inner and outer circles, respectively. Thus, in the pulse-echo case, the echo pressure SIR, shown in Fig. 3.4(c) , which looks similar to the one of the spherically circular transducer shown in Fig. 3.3(c), has three spikes at different time instants determined by $2t_1^{a1}$, $t_1^{a1} + t_1^{a2}$ and $2t_1^{a2}$, respectively. Here t_1^{a1} and t_1^{a2} are expressed by

$$t_1^{a1} = \sqrt{a_1^2 + (z - e_1)^2}\,\big/c\,, \tag{3.11a}$$

$$t_1^{a2} = \sqrt{a_2^2 + (z - e_2)^2}\,\Big/ c\,, \tag{3.11b}$$

where

$$e_1 = F - \sqrt{F^2 - a_1^2}\,, \tag{3.12a}$$

$$e_2 = F - \sqrt{F^2 - a_2^2}\,. \tag{3.12b}$$

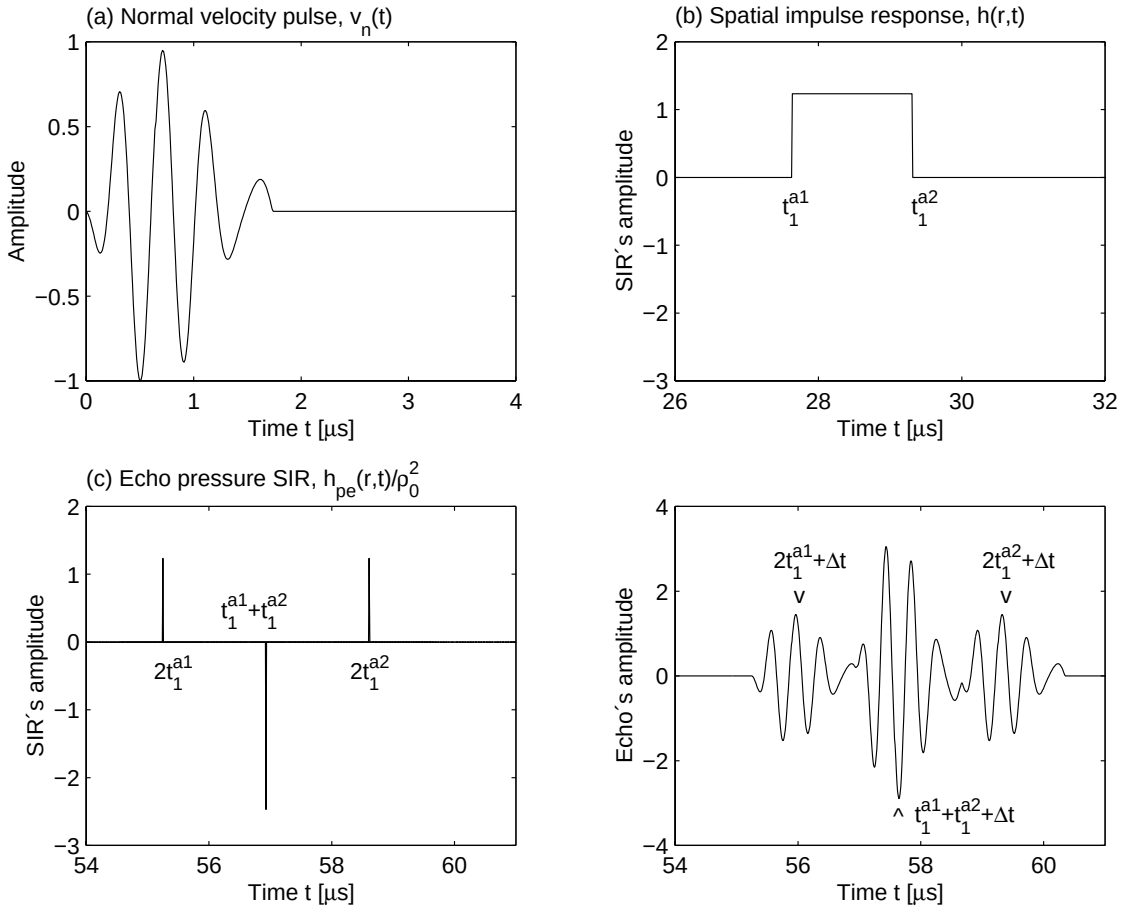

Fig. 3.4. (a) The normal velocity pulse on the spherically annular transducer, (b) the spatial impulse response (SIR) on the axis at *z*=40 mm, (c) the echo pressure SIR, and (d) the output of the transducer, the pulse-echo from the point scatterer.

If using a similar approach as for the spherically circular transducer, we have

$$\Delta t_{11} = t_1^{a2} - t_1^{a1} = \left[\sqrt{a_2^2 + (z - e_2)^2} - \sqrt{a_1^2 + (z - e_1)^2}\right]\Big/ c\,. \tag{3.13}$$

From three on-axis measurements at three different distances, z_I, z_{II} and z_{III}, we can find the effective inner and outer radii, and the focal length. However, it is tedious and difficult to solve the set of three equations Eq. (3.13). Therefore, we circumvent this difficulty using an alternative means, that is, using the time differences between the corresponding time instants obtained from different

measurements. For instance, from the measurements made at z_I, z_{II} and z_{III}, we can obtain the time differences

$$\Delta t_1^{a1,II,I} = t_1^{a1,II} - t_1^{a1,I} = \left[\sqrt{a_1^2 + (z_{II} - e_1)^2} - \sqrt{a_1^2 + (z_I - e_1)^2}\right] \Big/ c\,, \tag{3.14a}$$

$$\Delta t_1^{a1,III,I} = t_1^{a1,III} - t_1^{a1,I} = \left[\sqrt{a_1^2 + (z_{III} - e_1)^2} - \sqrt{a_1^2 + (z_I - e_1)^2}\right] \Big/ c\,, \tag{3.14b}$$

for the inner radius, and the time differences

$$\Delta t_1^{a2,II,I} = t_1^{a2,II} - t_1^{a2,I} = \left[\sqrt{a_2^2 + (z_{II} - e_2)^2} - \sqrt{a_2^2 + (z_I - e_2)^2}\right] \Big/ c\,, \tag{3.15a}$$

$$\Delta t_1^{a2,III,I} = t_1^{a2,III} - t_1^{a2,I} = \left[\sqrt{a_2^2 + (z_{III} - e_2)^2} - \sqrt{a_2^2 + (z_I - e_2)^2}\right] \Big/ c\,, \tag{3.15b}$$

for the outer radius.

From Eqs. (3.14) and (3.15), we can find the three effective geometrical parameters in the following way,

$$a_{1eff} = \sqrt{\beta_{a1}^2 - (z_I - e_1)^2}\,, \tag{3.16}$$

$$a_{2eff} = \sqrt{\beta_{a2}^2 - (z_I - e_2)^2}\,, \tag{3.17}$$

$$F_{eff} = \left(a_{1eff}^2 + e_1^2\right) \Big/ 2e_1\,, \text{ or } F_{eff} = \left(a_{2eff}^2 + e_2^2\right) \Big/ 2e_2\,, \tag{3.18}$$

where

$$\beta_{a1} = \frac{z_{II}^2 - z_I^2 - 2(z_{II} - z_I)e_1 - \left(c\Delta t_1^{a1,II,I}\right)^2}{2c\Delta t_1^{a1,II,I}}\,, \tag{3.19}$$

$$\beta_{a2} = \frac{z_{II}^2 - z_I^2 - 2(z_{II} - z_I)e_2 - \left(c\Delta t_1^{a2,II,I}\right)^2}{2c\Delta t_1^{a2,II,I}}\,, \tag{3.20}$$

$$e_1 = \left\{\frac{z_{III}^2 - z_I^2 - \left(c\Delta t_1^{a1,III,I}\right)^2}{c\Delta t_1^{a1,III,I}} - \frac{z_{II}^2 - z_I^2 - \left(c\Delta t_1^{a1,II,I}\right)^2}{c\Delta t_1^{a1,II,I}}\right\} \Bigg/ \left\{\frac{2(z_{III} - z_I)}{c\Delta t_1^{a1,III,I}} - \frac{2(z_{II} - z_I)}{c\Delta t_1^{a1,II,I}}\right\}, \tag{3.21}$$

$$e_2 = \left\{\frac{z_{III}^2 - z_I^2 - \left(c\Delta t_1^{a2,III,I}\right)^2}{c\Delta t_1^{a2,III,I}} - \frac{z_{II}^2 - z_I^2 - \left(c\Delta t_1^{a2,II,I}\right)^2}{c\Delta t_1^{a2,II,I}}\right\} \Bigg/ \left\{\frac{2(z_{III} - z_I)}{c\Delta t_1^{a2,III,I}} - \frac{2(z_{II} - z_I)}{c\Delta t_1^{a2,II,I}}\right\}. \tag{3.22}$$

Methods for characterizing both the spherically circular and annular transducers based on the SIRM have been developed above. In sequel, these methods will be referred to as *spatial impulse response characterization methods* (SIRCM).

3.2.2 Measurements and transducer characterizations

Transducer characterization requires some measurements of its field, for instance, the measurement of field scattered from a rigid point scatterer in pulse-echo mode. Since a point scatterer is a theoretical concept, unavailable in practice, a small drill (0.3-mm in diameter) with a flat end directed towards the transducer was used as its approximation.

Care must be taken when measuring some parameters, like sound velocity and distances of transducer movements. The sound velocity in water was measured using a step-like steel plate with each step hight 2-mm. Since the sound velocity in water varies with temperature and we do not have a room with stabilized temperature for our measurement system, it had to be measured each time when acoustic field measurements were conducted. The measured value of sound velocity was 1485 m/s in the room temperature.

Another important thing is to find the transducer axis precisely. As mentioned above, the on-axis SIR is needed for transducer characterization. If the axis is missed in a measurement, the off-axis SIR is obtained, and this will cause some errors in transducer characterization. Smaller spatial sampling intervals (small steps of the scanner step motor) yield smaller error and a more accurate characterization. To achieve this, we tried different sampling intervals (e.g., 0.25, 0.1 and 0.05 mm) and finally, a 0.05-mm sampling interval was chosen for the measurements. Fig. 3.5 shows two cross-sectional images of fields from the small scatterer located at z = 35 and 40 mm, respectively. The scanning area was only 2x2 mm. From such cross-sectional images we located the pulse echo signals that were as close to the transducer axis as possible (the signals at the origins of the images). In this case, the maximum possible displacement error was $0.05/\sqrt{2}$ mm if the transducer axis was just in the middle of the two sampling positions in both the *x*- and *y*-directions.

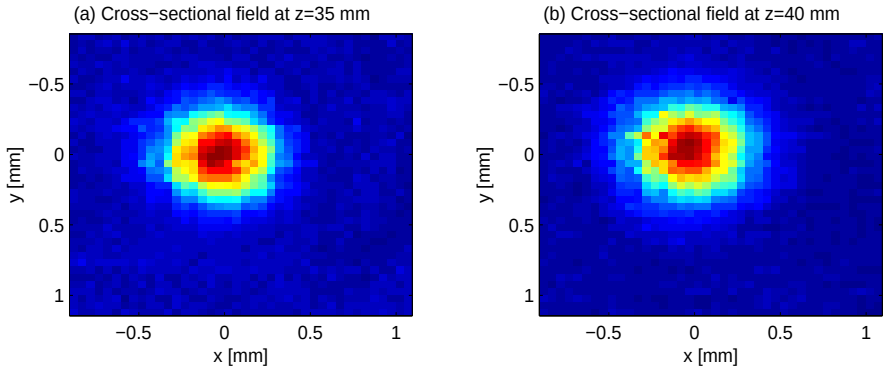

Fig. 3.5. Cross-sectional images of pulse-echo field for the spherical annular transducer from the small scatterer located at (a) *z*=35 mm and (b) *z*=40 mm.

For a spherically

concave transducer, two geometrical parameters, radius and focal length, need to be determined. Two measurements were made at two different distances z=35 and 40 mm, and the pulse-echo signals that were closest to the transducer axis, are shown in Fig. 3.6(a) and (b), respectively. Time differences obtained from Fig. 3.6 are: Δt_{10} =0.7759 and 0.6636 μs for z=35 and 40 mm, respectively. Inserting these parameters into Eqs. (3.8)-(3.10) resulted in a_{eff} = 9.86 mm and F_{eff} =223.5 mm. Inserting the nominal parameters, a= 10 mm and F = 210 mm, yielded respective values: Δt_{10} =0.7889 for z=35 and 0.6734 μs for 40 mm.

For a spherically annular transducer, three geometrical parameters, inner and outer radii and focal length, had to be determined. We chose three measurements made at z=33, 35 and 37 mm, and selected the pulse-echo signals that were closest to the transducer axis (Fig. 3.7). The values obtained from the figure and measuring the corresponding time instants in the way as shown in Fig. 3.4(d), were respectively: $\Delta t_1^{a1,II,I}$ =1.2838 μs, $\Delta t_1^{a1,III,I}$ =2.5740 μs, $\Delta t_1^{a2,II,I}$ =1.1800 μs, and $\Delta t_1^{a2,III,I}$ =2.3755 μs. Putting these data in Eqs. (3.16) – (3.18) yields: a_{1eff} =10.7 mm, a_{2eff} =18.3 mm, and F_{eff} =232 mm.

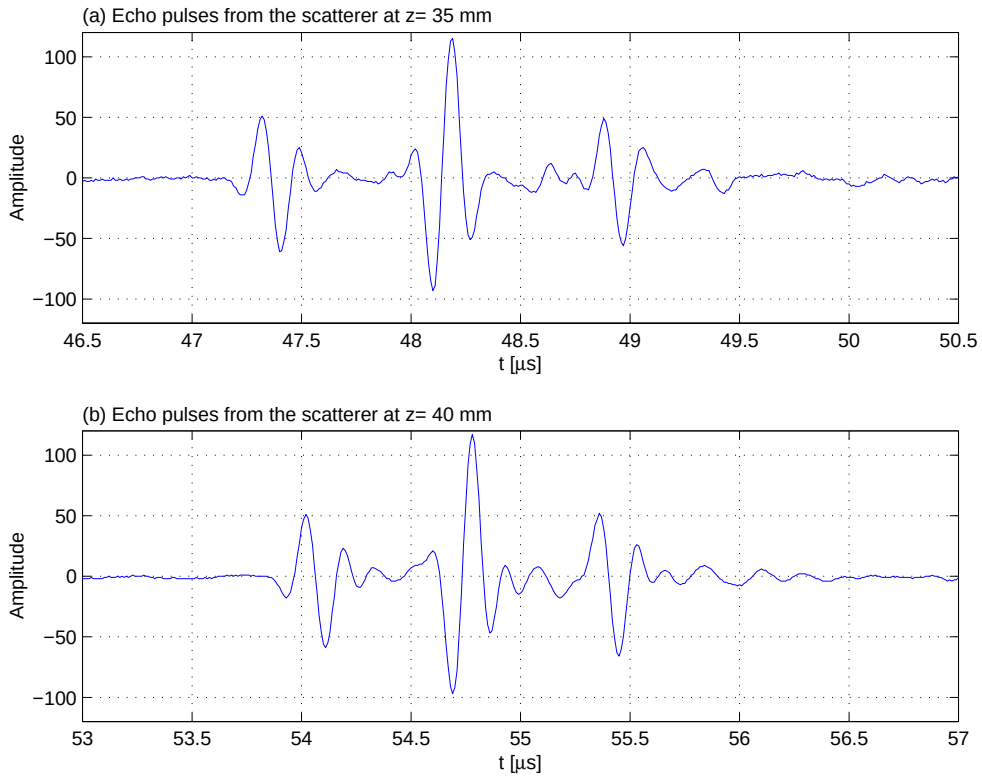

Fig. 3.6. Echo pulses of the spherical circular transducer that come from the small scatterer located at (a) z=35 mm and (b) z=40 mm.

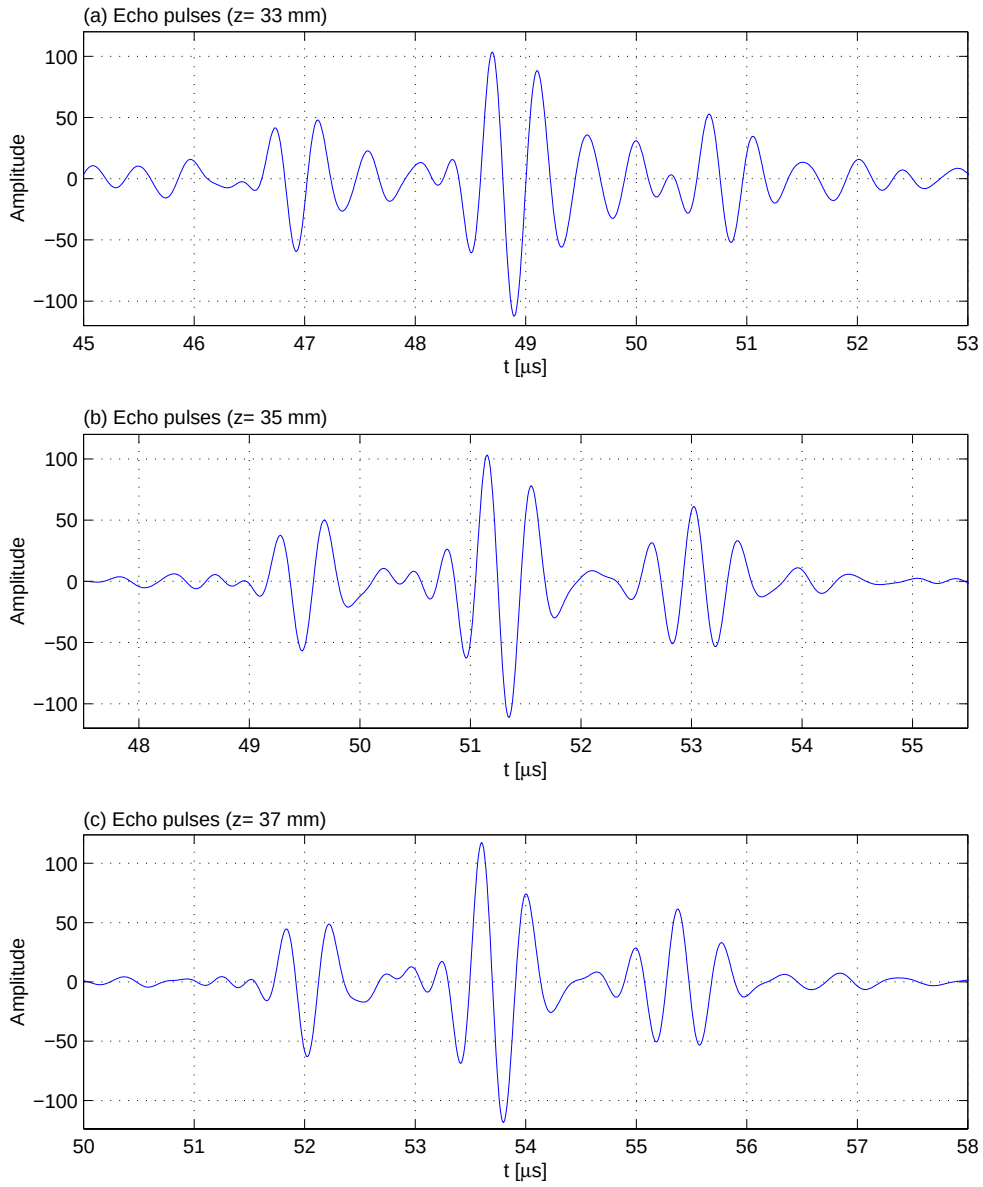

Fig. 3.7. Echo pulses of the spherical annular transducer that come from the small scatterer located at (a) z=33 mm, (b) z=35 mm, and (c) z=37 mm.

It should be pointed out that all the effective geometrical parameters were determined directly from measurements using simple calculations; for example, by using the measured time difference defined by Eq. (3.7) in Eqs. (3.8) – (3.10) for the spherically circular transducer, and those defined by Eqs. (3.14) and (3.15) in Eqs. (3.16) – (3.22) for the spherically annular transducer.

To verify the obtained effective geometrical parameters, we will put them into the SIRM-based model, then calculate the respective pulse-echo fields and, finally, compare with the measured ones. However, we need normal velocity pulse excitations $v_n(t)$ for the transducers of both types to achieve this. We deconvolved the measured data with the calculated SIR at z=40 mm using the method presented in our previous work [2,20] (simplified Wiener filter). However, we could not

obtain satisfactory results since even a tiny deviation of the measurement position from the position of the calculated SIR may cause a large error that in turn results in the failure of the deconvolution. To circumvent the problem we used acoustical knowledge concerning transducer radiation. Let us conside as an example the measured data at z=40 mm for the spherically circular transducer (Fig. 3.5(b)) to show how the normal velocity pulse $v_n(t)$ was obtained. We take the part of the first pulse from the starting instant to the instant of the second positive peak, then take the part of the third pulse from its second positive peak, and connect these two parts in serial. As a result we obtain the $v_n(t)$ shown in Fig. 3.3(a). Similarly, we used the measured data at z=35mm and obtained the $v_n(t)$ for the spherically annular transducer (Fig. 3.4(a)).). Using the effective geometrical parameters to calculate the SIR, and using the normal velocities, we have, from Eq. (3.3), calculated the pulse-echo fields for both transducers. The calculated results for both transducers are shown Figs. 3.8 and 3.9, respectively, together with the corresponding measurements. Comparison of the results in these figure demonstrates that using the effective geometrical parameters obtained using the SIRCM in the SIRM-based model provides a good prediction.

To depict the difference between the results calculated using the nominal geometrical parameters with the measured results, we show comparison of the measured and calculated results for the spherically circular and annular transducers in Figs. 3.10 and 3.11, respectively. For the spherically circular transducer, a minor difference between the measured and calculated results appears (Fig. 3.10) but for the spherically annular transducer, the difference is quite large (see Fig. 3.11).

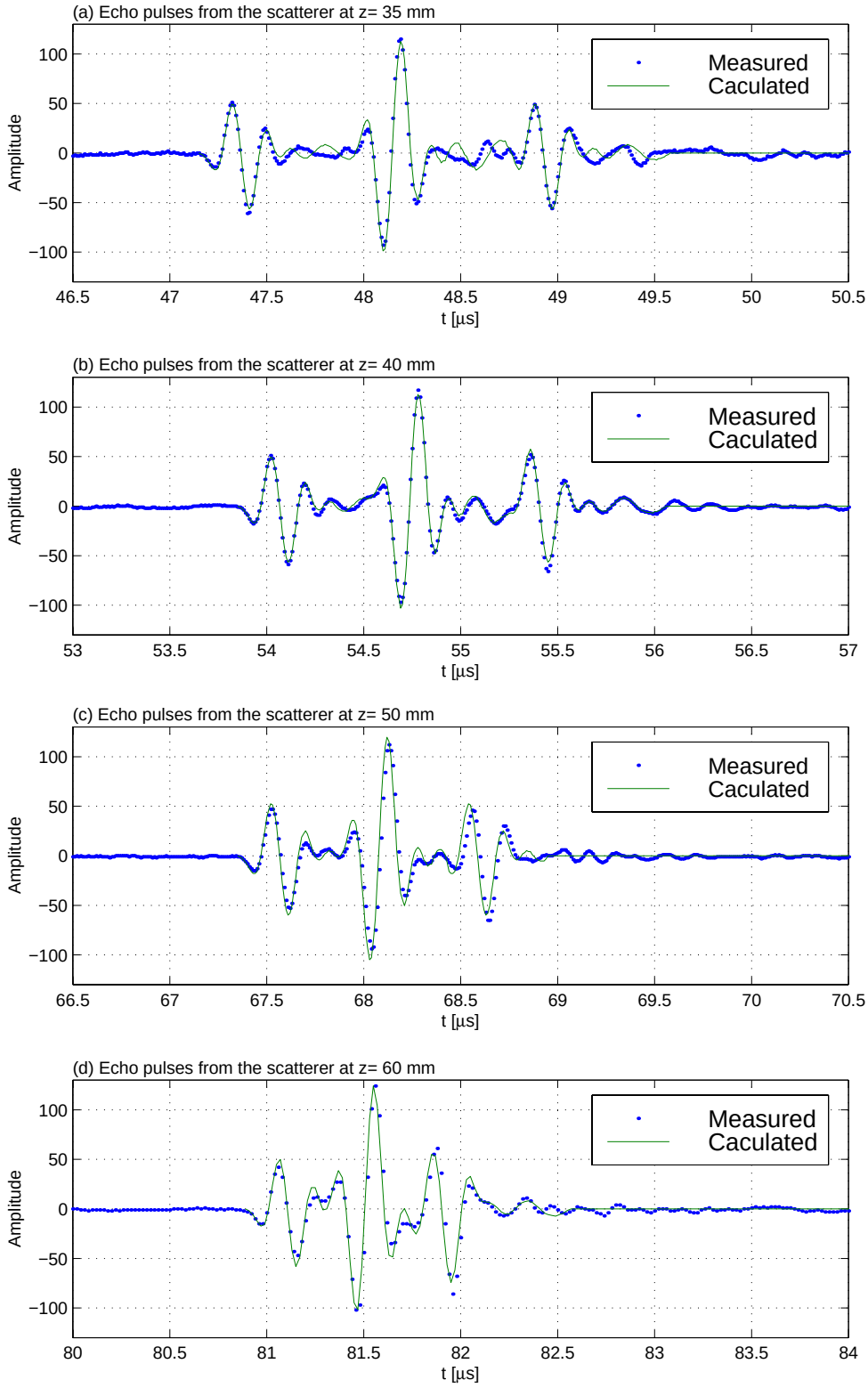

Fig. 3.8. Comparison of the measured and calculated results for the spherical circular transducer when the small scatterer is located at (a) z=35 mm, (b) z=40 mm, (c) z=50, and (d) z=60. The *effective* radius and focal length are used in the calculations.

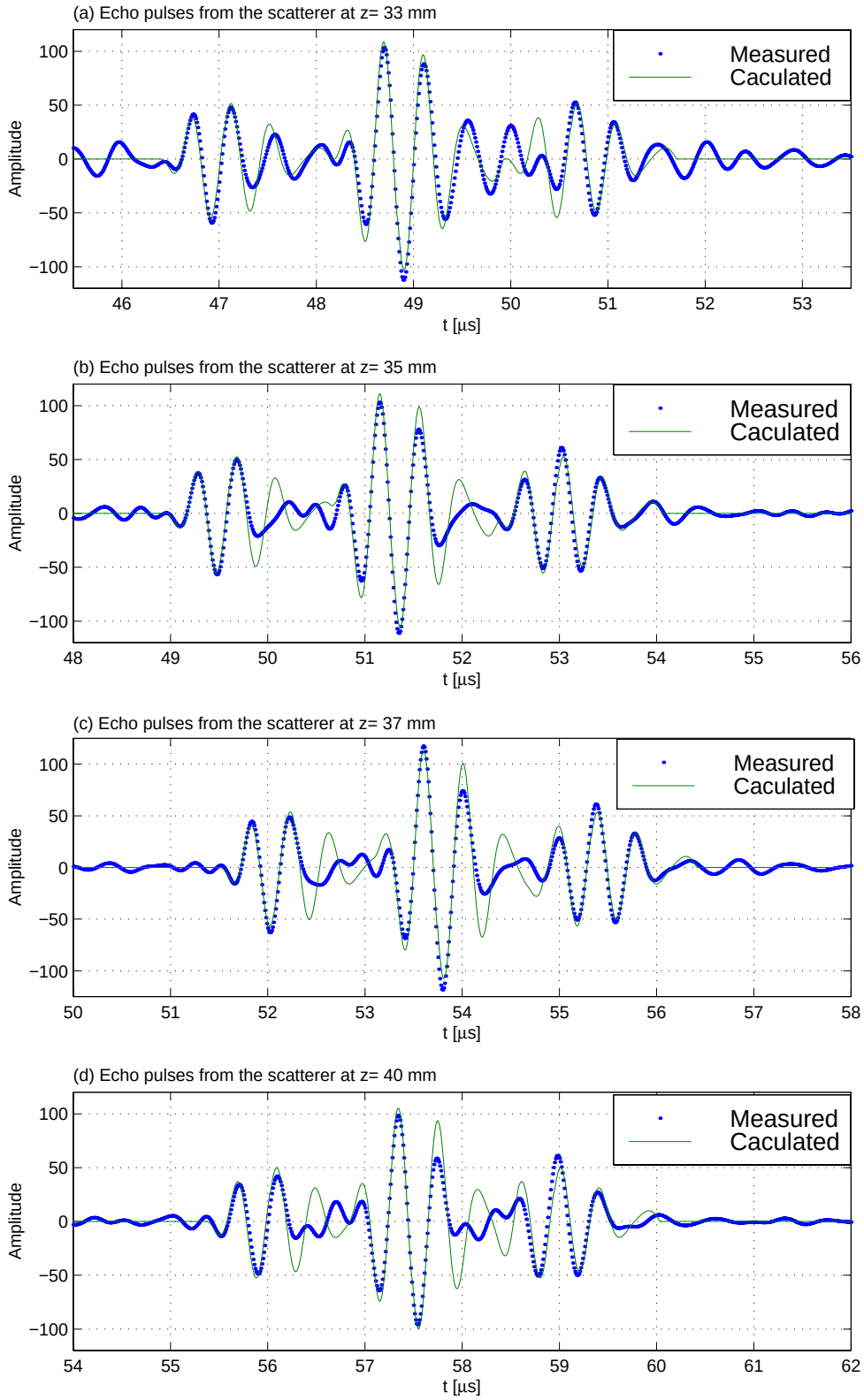

Fig. 3.9. Comparison of the measured and calculated results for the spherical annular transducer when the small scatterer is located at (a) *z*=33 mm, (b) *z*=35 mm, (c) *z*=37, and (d) *z*=40. The *effective* inner and outer radii, and focal length are used in the calculations.

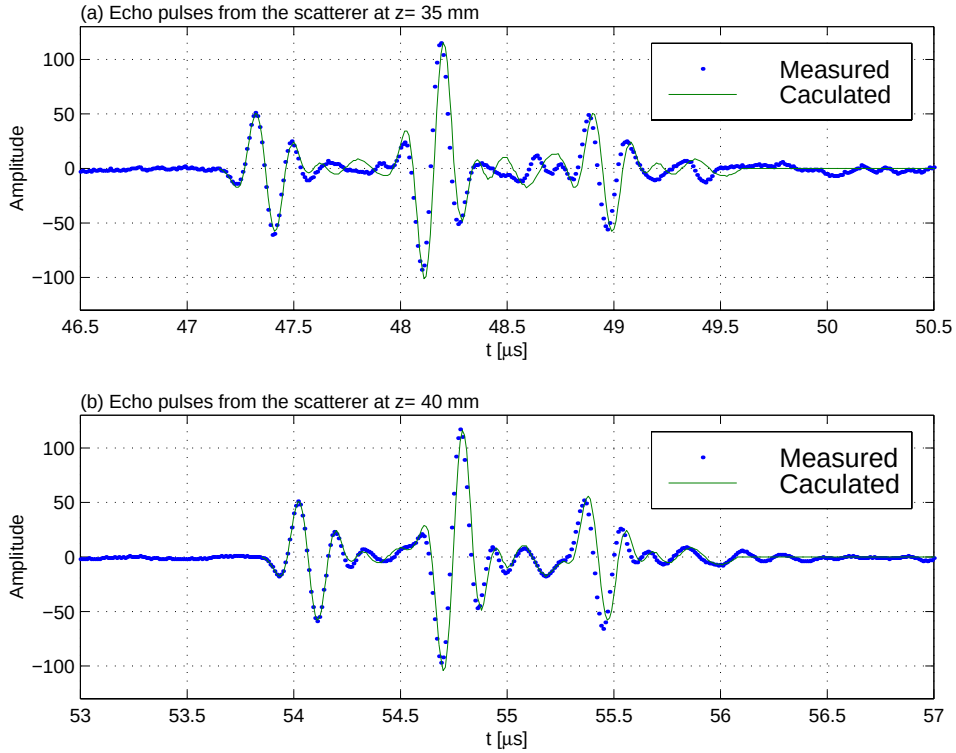

Fig. 3.10. Comparison of the measured and calculated results for the spherical circular transducer when the small scatterer is located at (a) *z*=35 mm, (b) *z*=40 mm. The *nominal* radius, and focal length are used in the calculations.

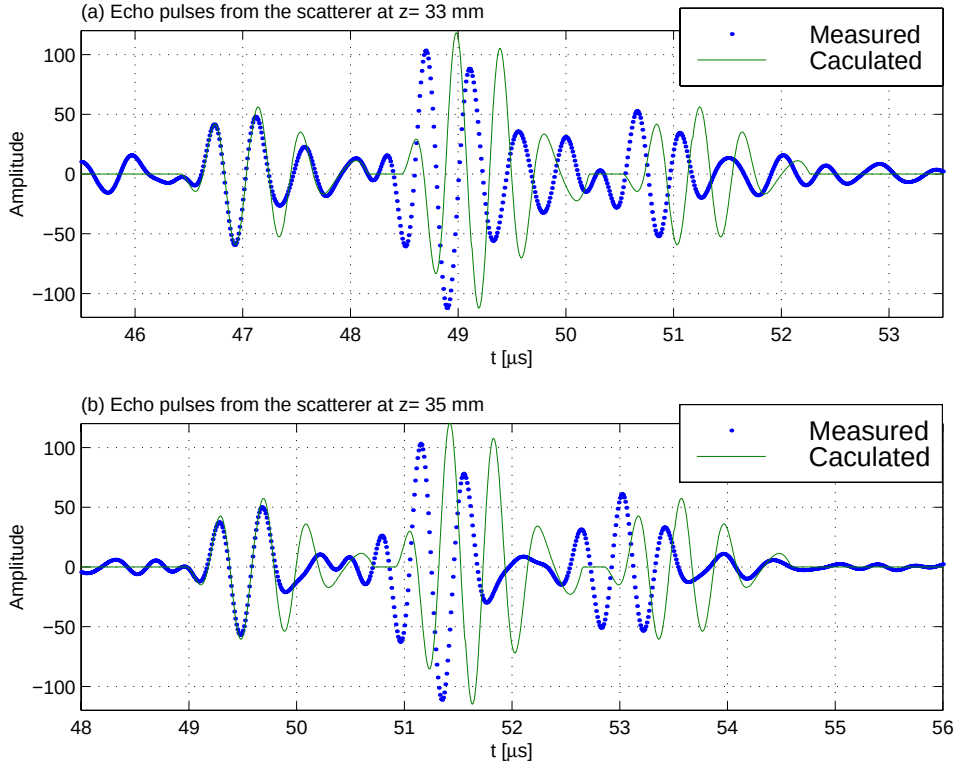

Fig. 3.11. Comparison of the measured and calculated results for the spherical annular transducer when the small scatterer is located at (a) *z*=33 mm, (b) *z*=35 mm. The *nominal* inner and outer radii, and focal length are used in the calculations.

3.3 Modeling of ultrasonic fields radiated by spherically focused transducers

It has been demonstrated in Sect. 3.2 that the acoustic fields radiated by spherically focused circular and annular transducers into homogeneous fluid media can be calculated by the SIRM and the transducers of the two types can be characterized by the SIRCM. Now, in this section we will calculate the elastic fields radiated by the transducers into immersed solids. In this case, the SIRM is not applicable. In our early work, we used the angular spectrum approach (ASA) to calculate elastic fields from planar transducers and arrays [21,22], and developed the extended ASA for curved transducers with the application to cylindrically curved arrays [3]. The extended ASA will be applied here to the case of spherically focused transducers. Since spherically focused transducers are axisymmetric the 2-D integral for calculating the angular spectra can be reduced to 1-D integral. For a planar circular transducer, the integral is the well-known Hankel transform [23]. However, the Hankel transform does not apply to a spherically circular or annular transducer. In this work, we have developed a new algorithm to calculate the angular spectra for spherically focused transducers, and applied it to modeling elastic fields in immersed solids. Full description of the new algorithm can be found in Appendix 3-B. This section is focused on the modeling of the elastic fields in immersed solids. The theories of the ASA for the case of axisymmetric transducers are presented in detail in Appendix 3-C.

From Appendix 3-B (Eq. (3-B.22)) it follows that the angular spectrum (in the $z= z_1$ plane) of a spherically focused (annular) transducer (with inner and outer radii, a_1 and a_2, and focal length F) in a fluid can be calculated from

$$V(\theta, z_1) = 2\pi F \int_{a_1}^{a_2} \frac{J_0(\rho k \sin\theta)}{\sqrt{F^2 - \rho^2}} \exp\left[j\left(z_1 - F + \sqrt{F^2 - \rho^2} \right) k \cos\theta \right] \rho d\rho \,. \tag{3.23}$$

A spherically circular transducer can be thought of as a special case of the annular transducer with a_1=0 and a_2=a.

The acoustic field in the fluid can be obtained by superimposing the decomposed plane waves in Eq. (3-23),

$$\tilde{p}(\rho, z) = \frac{k^2 \rho_0 c}{2\pi} \int_0^{\pi/2} V(\theta, z_1) J_0(\rho k \sin\theta) \sin\theta \exp\left[j(z - z_1) k \cos\theta \right] d\theta \,. \tag{3.24}$$

The (longitudinal wave) LW elastic field radiated by the transducer into the immersed solid can be constructed by superimposing all the decomposed plane waves in Eq. (3-23) that propagate into the solid, in the following way (c.f., Eqs. (3-C.4) and (3-C.7)),

$$\tilde{\mathbf{v}}_L(\rho,z)=\frac{1}{2\pi}\int_0^{\pi/2}V_L(\theta,\rho,z)d\theta$$

$$=\frac{k_L k}{2\pi}\int_0^{\pi/2}\hat{\mathbf{L}}T_{fs}(\theta)V\left(k\sin\theta,z_1\right)J_0(\rho k\sin\theta)\sin\theta\exp\left[j(z_{fs}-z_1)k\cos\theta+j(z-z_{fs})k_L\cos\theta_L\right]d\theta\,,$$

$$(z\geq z_{fs}). \qquad (3\text{-}25)$$

Consider a specific case where a copper block is immersed in water with a 30-mm water path length. The calculated acoustic fields (in water without the block) from the 4.83-MHz circular and 2.26-MHz annular transducers are shown in Figs. 3.12 and 3.13, respectively. The elastic fields from both transducers in the block are shown in Figs. 3.14 and 3.15, respectively. Note that the elastic fields start from z=30 mm because the water layer ranges from z=0~30 mm.

The upper panels of the figures show the fields in color scale and in the area of y= –16~16 mm and z=10~270 mm for the circular transducer and of y= –25~25 mm and z=10~270 mm for the annular transducer, and the lower ones show their on-axis fields.

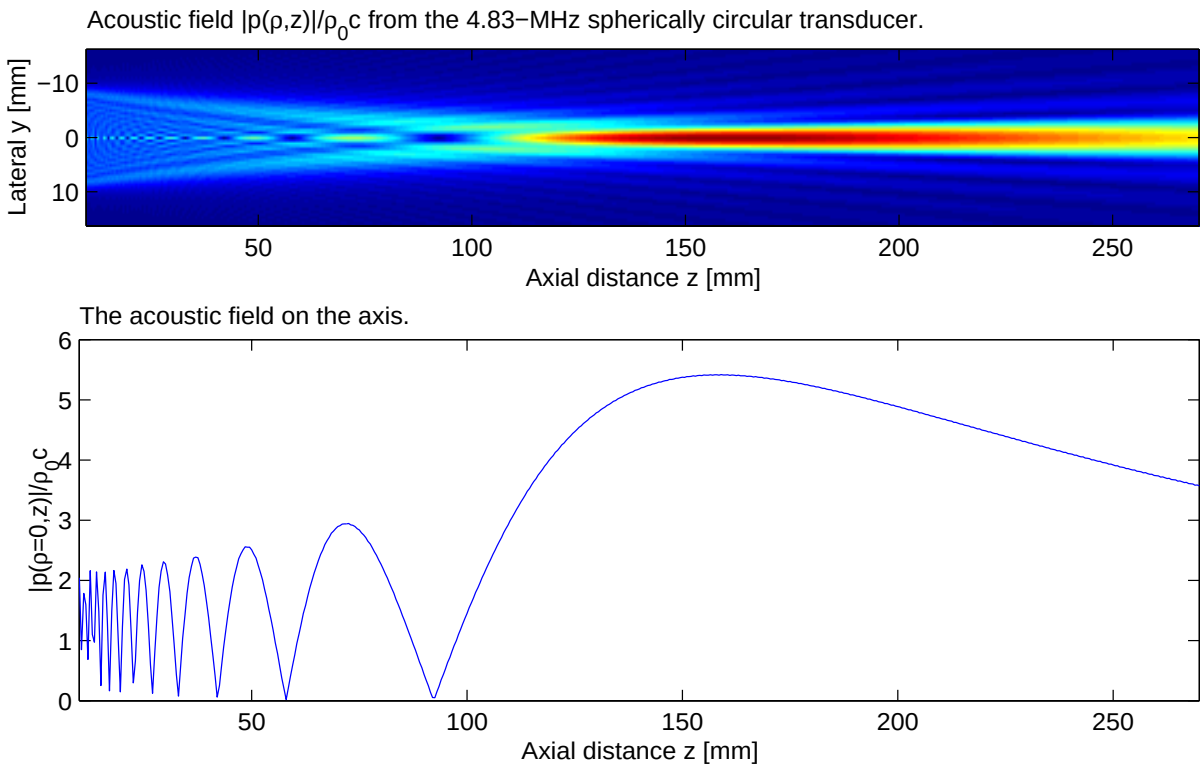

Fig. 3.12. Acoustic field from the 4.83-MHz spherically circular transducer.

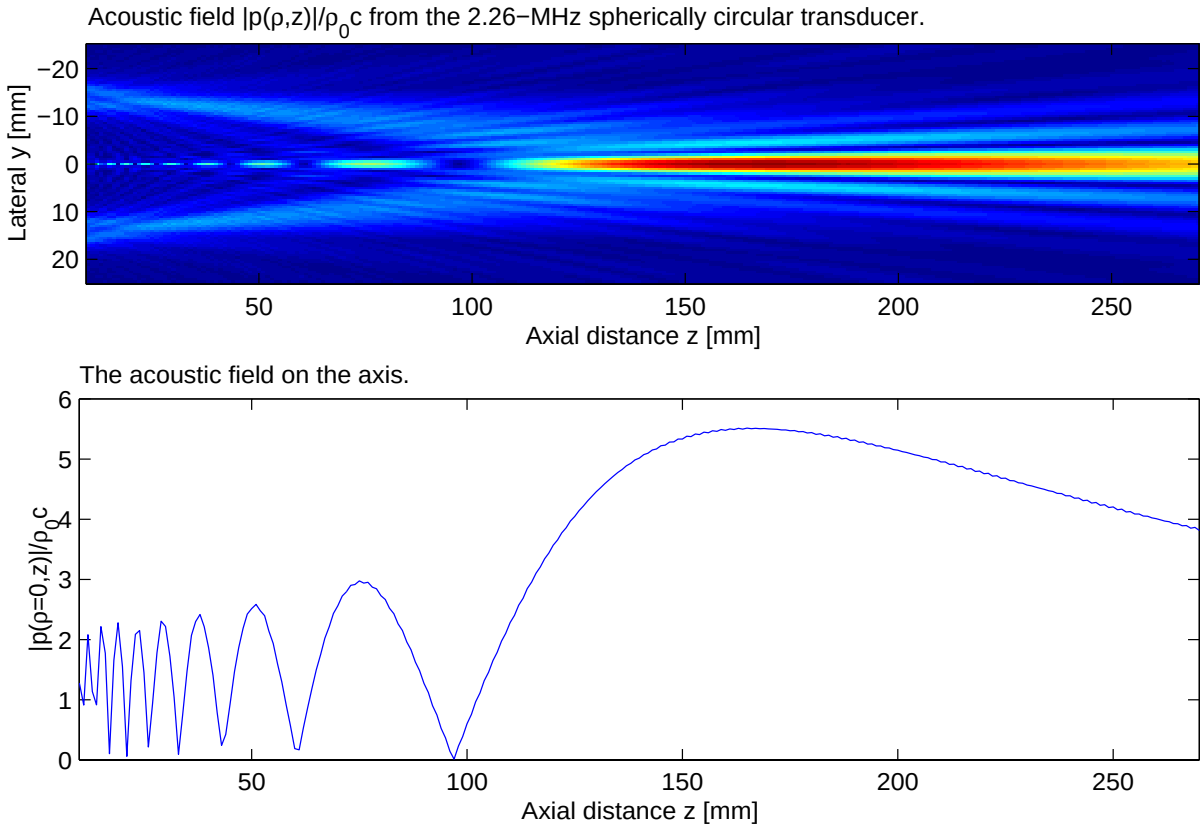

Fig. 3.13. Acoustic field from the 2.26-MHz spherically annular transducer.

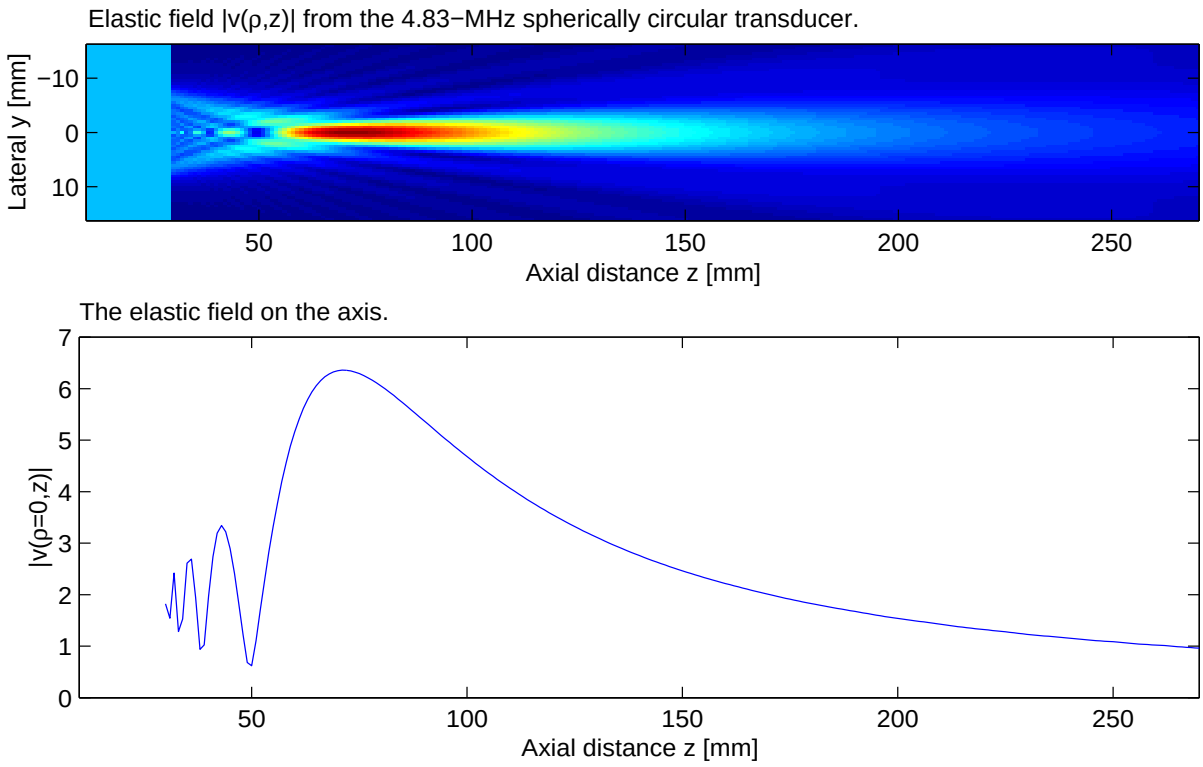

Fig. 3.14. Elastic field from the 4.83-MHz spherically circular transducer.

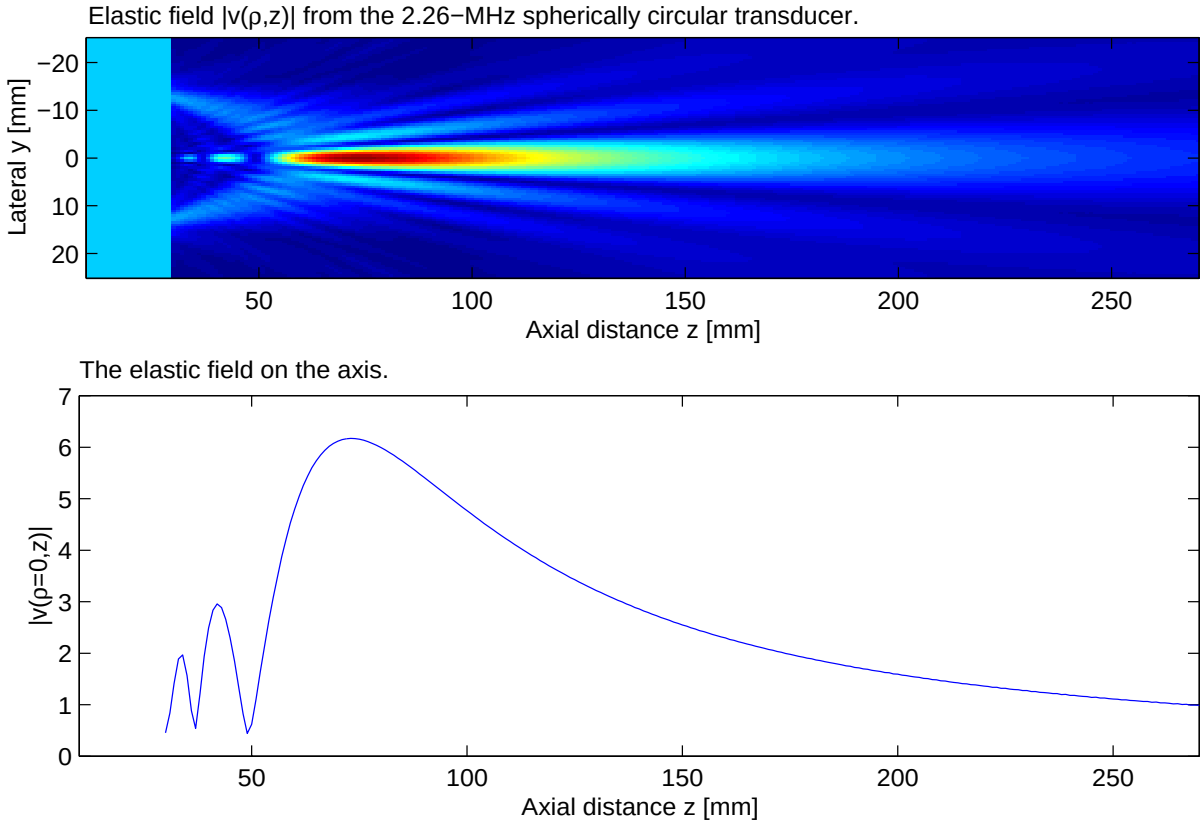

Fig. 3.15. Elastic field from the 2.26-MHz spherically annular transducer.

3.4 Evaluation of attenuation in copper blocks

Ultrasonic attenuation of a material is one of the important parameters related to the material's macro- and microstructure. Thus quantitative evaluation of attenuation provides the information about mechanical properties of the material. Quantitative evaluation of attenuation requires correction for transducer diffraction effects. To achieve this we have developed the tools for calibrating the transducers used for the evaluation (Sect. 3.2), and calculating their ultrasonic fields (Sect. 3.3, Appendices 3-B and 3-C).

Attenuation evaluation is conducted in the immersion-pulse-echo scheme as shown in Fig. 3.16. In this scheme the pulse echoes from the front and back surfaces of the copper plate are used. When the plate is not thin, the diffraction effect cannot be neglected and it will cause significant error in the evaluation, or in some situations it may even result in an unreasonable evaluation. This has been demonstrated in our previous work [2].

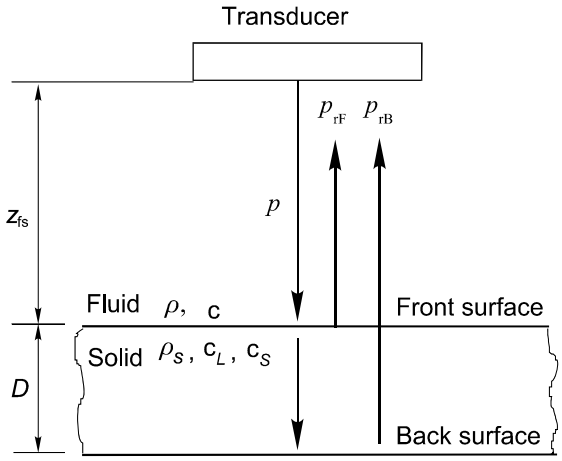

Fig. 3.16. Immersion-pulse-echo scheme for attenuation evaluation.

Assuming that the pulse-echoes from the front and back surfaces are $\langle p_{rF}(t)\rangle$ and $\langle p_{rB}(t)\rangle$, and their spectra (or the continuous wave component at frequency ω) are $\langle \tilde{p}_{rF}(\omega)\rangle$ and $\langle \tilde{p}_{rB}(\omega)\rangle$, the LW attenuation coefficient is evaluated with diffraction correction in the manner [2],

$$\alpha_L(\omega) = \frac{1}{2D}\ln\frac{\left|\langle \tilde{p}_{rF}(\omega)\rangle / \langle \tilde{p}_{0rF}(\omega)\rangle\right|}{\left|\langle \tilde{p}_{rB}(\omega)\rangle / \langle \tilde{p}_{0rB}(\omega)\rangle\right|}, \tag{3.26}$$

where $\left\langle \tilde{p}_{0rq}(\omega) \right\rangle$ are the fields from the front (q=F) and back (q=F) surfaces (usually calculated) with $\alpha_L = 0$. As the attenuation in a fluid (usually water) is very small and neglected, the echoes from the front surface are the same, i.e., $\left\langle \tilde{p}_{rF}(\omega) \right\rangle = \left\langle \tilde{p}_{0rF}(\omega) \right\rangle$. We get a simpler alternative,

$$\alpha_L(\omega) = \frac{1}{2D} \ln \frac{\left| \left\langle \tilde{p}_{0rB}(\omega) \right\rangle \right|}{\left| \left\langle \tilde{p}_{rB}(\omega) \right\rangle \right|}. \tag{3.27}$$

α_L in Eqs. (3.26) or (3.27) is in NP/m, and for dB/m, use the conversion, 1 NP = 8.686 dB. $\left\langle \tilde{p}_{rq}(\omega) \right\rangle$ are obtained from measurements, and $\left\langle \tilde{p}_{0rq}(\omega) \right\rangle$ from calculations. We will work out the calculating of $\left\langle \tilde{p}_{0rq}(\omega) \right\rangle$ below.

Using the work presented in Sect. 3.3 and Appendix 3-C, we can calculate the reflected fields from the front (q=F) and back (q=B) surfaces at frequency ω,

$$\tilde{p}_{rq}(\rho, z; \omega) = \frac{1}{2\pi} \int_0^{\pi/2} P_{rq}(\theta, \rho, z; \omega) d\theta. \tag{3.28}$$

In pulse-echo mode, a transducer is used both as transmitter and receiver. The reflected fields are measured by the same transducer as it is used for transmitting. For a spherically focused transducer the measured pressures can be expressed as (c.f., [2])

$$\left\langle \tilde{p}_{rq}(\omega) \right\rangle = \frac{1}{S} \int\int_S \tilde{p}_{rq}(\rho', \varphi', z'; \omega) \rho' d\rho' d\varphi' = \frac{2\pi}{S} \int_{a_1}^{a_2} \tilde{p}_{rq}(\rho', z'; \omega) \frac{F\rho' d\rho'}{\sqrt{F^2 - \rho'^2}}, \tag{3.29}$$

where $z = f(\rho) = F - \sqrt{F^2 - \rho^2}$, $a_1 \le \rho \le a_2$ defines the surface of the spherically focused transducer. It should be noted that, when Eq. (3.29) is numerically implemented for the case of $a_1 = 0$ and $a_2 = a$, the axisymmetry makes its numerical form be,

$$\left\langle \tilde{p}_{rq}(\omega) \right\rangle = \frac{2\pi}{S} \left\{ \tilde{p}_{rq}(0, f(0); \omega) \frac{(\Delta a)^2}{8} + \sum_{m=1}^{M} \frac{F \tilde{p}_{rq}(\rho_m, f(\rho_m); \omega)}{\sqrt{F^2 - \rho_m^2}} \rho_m \Delta a \right\}, \ (\rho_m = m\Delta a), \tag{3.30}$$

where M is determined from Eq. (3-B.25) in Appendix 3-B so that the aliasing error can be minimized.

The pulse-echoes from the front and back surfaces, namely, the pressures measured by the receiver can be obtained by inverse Fourier transform of Eq. (3.29),

$$\left\langle p_{rq}(t)\right\rangle = \int_{-\infty}^{\infty} \left\langle \tilde{p}_{rq}(\omega)\right\rangle e^{-j\omega t} d\omega . \tag{3.31}$$

The evaluation of attenuation was made for copper canister CAN 1 using both the spherically circular (4.83 MHz) and annular (2.26 MHz) transducers (characterized above) in the experimental setup shown in Fig. 3.16. The measured and calculated back surface echos were used for the attenuation evaluation using Eq. (3.27).

The ultrasonic signal from the 4.83-MHz transducer is illustrated in Fig. 3.17, and the calculated results, the front and back surface echoes corresponding to those in 3.17 (b) and (c), are shown in Fig. 3.18. The evaluated attenuation versus frequency is plotted in Fig. 3.19, in which a reference line $\alpha_L = 0.025 f$ (dashed) is given and the attenuation is in expressed dB/mm.

Similarly, , the ultrasonic signal measured for the 2.26-MHz transducer is shown in Fig. 3.20, and the calculated results, the front and back surface echoes corresponding to those in 3.20 (b) and (c), are presented in Fig. 3.21. The evaluated attenuation in function of frequency is shown in Fig. 3.22, where a reference line $\alpha_L = 0.017 f - 0.018$ was plotted and the attenuation was also expressed in dB/mm.

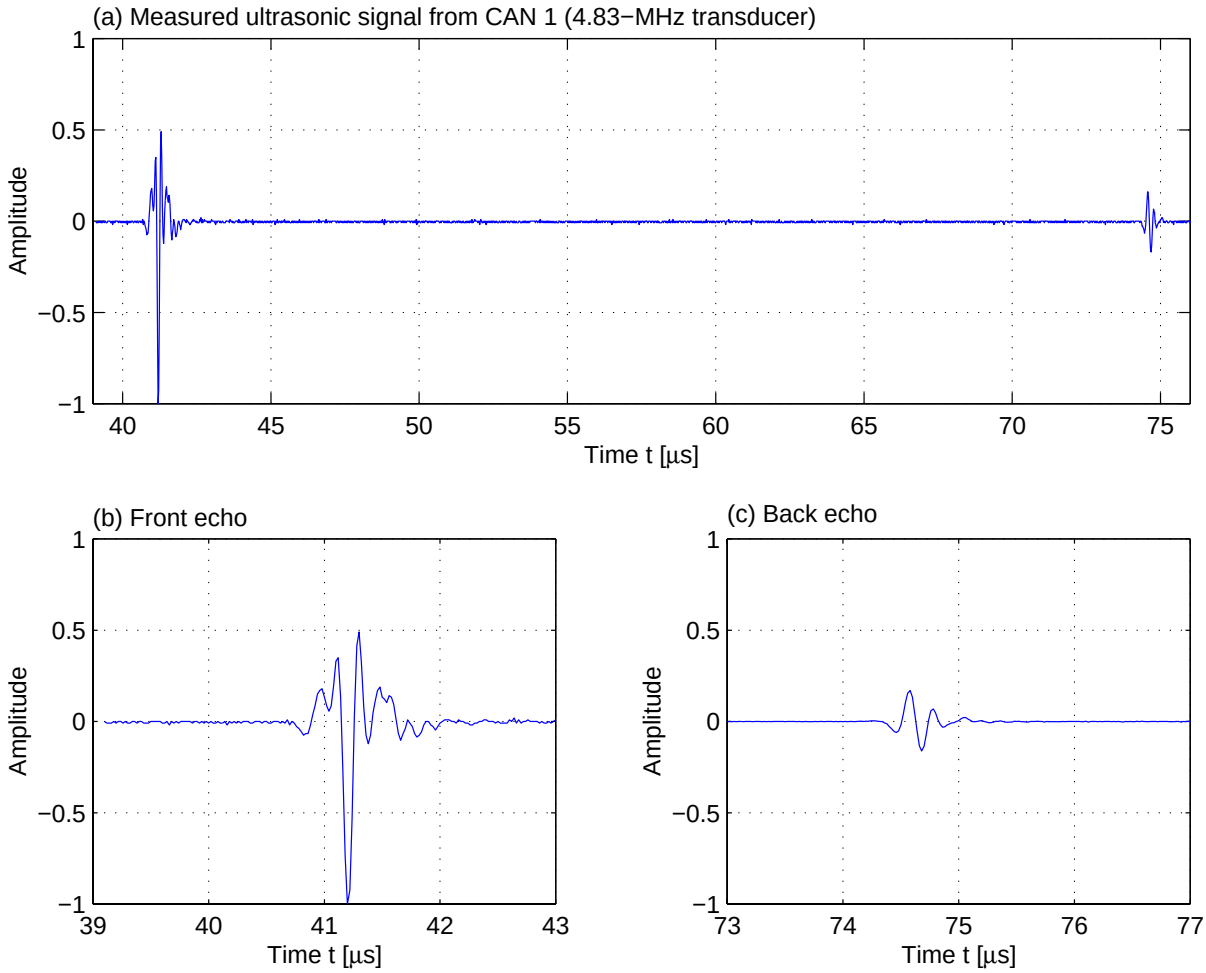

Fig. 3.17. Ultrasonic signal measured using the 4.83-MHz spherically circular transducer on copper block CAN 1. The signal is from the non-welded zone. (a) The overall signal, (b) the front surface echo, and (c) the back surface echo.

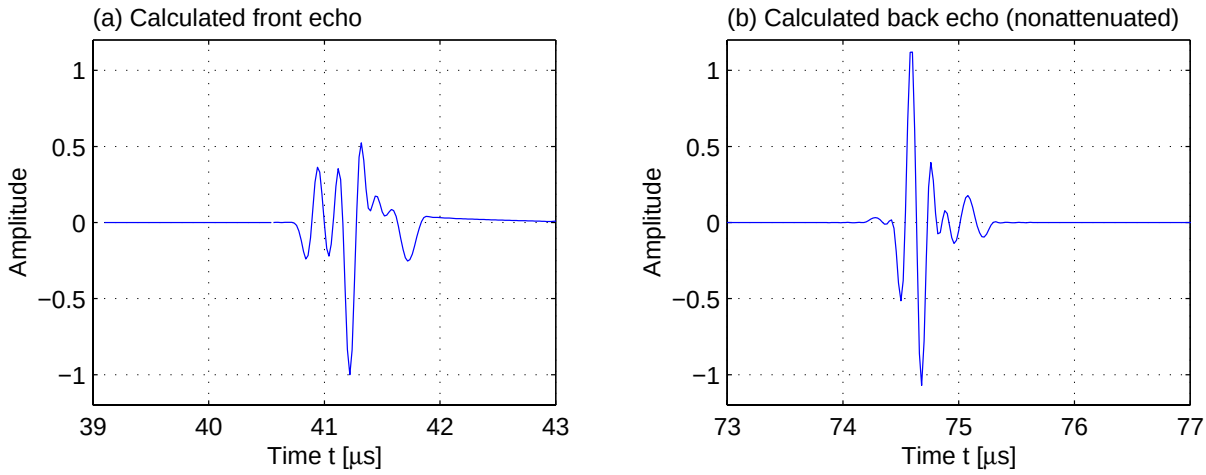

Fig. 3.18. Calculated ultrasonic signals corresponding to those shown in Fig. 3.17. (a) the front surface echo, and (b) the back surface echo.

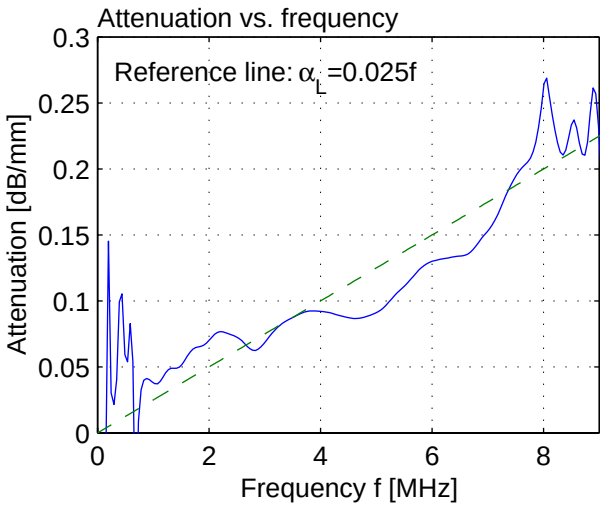

Fig. 3.19. Attenuation versus frequency evaluated using the 4.83 -MHz transducer. Measured and calculated back surface echoes shown in Figs. 3.17(c) and 3.18(b), respectively, were used for the evaluation.

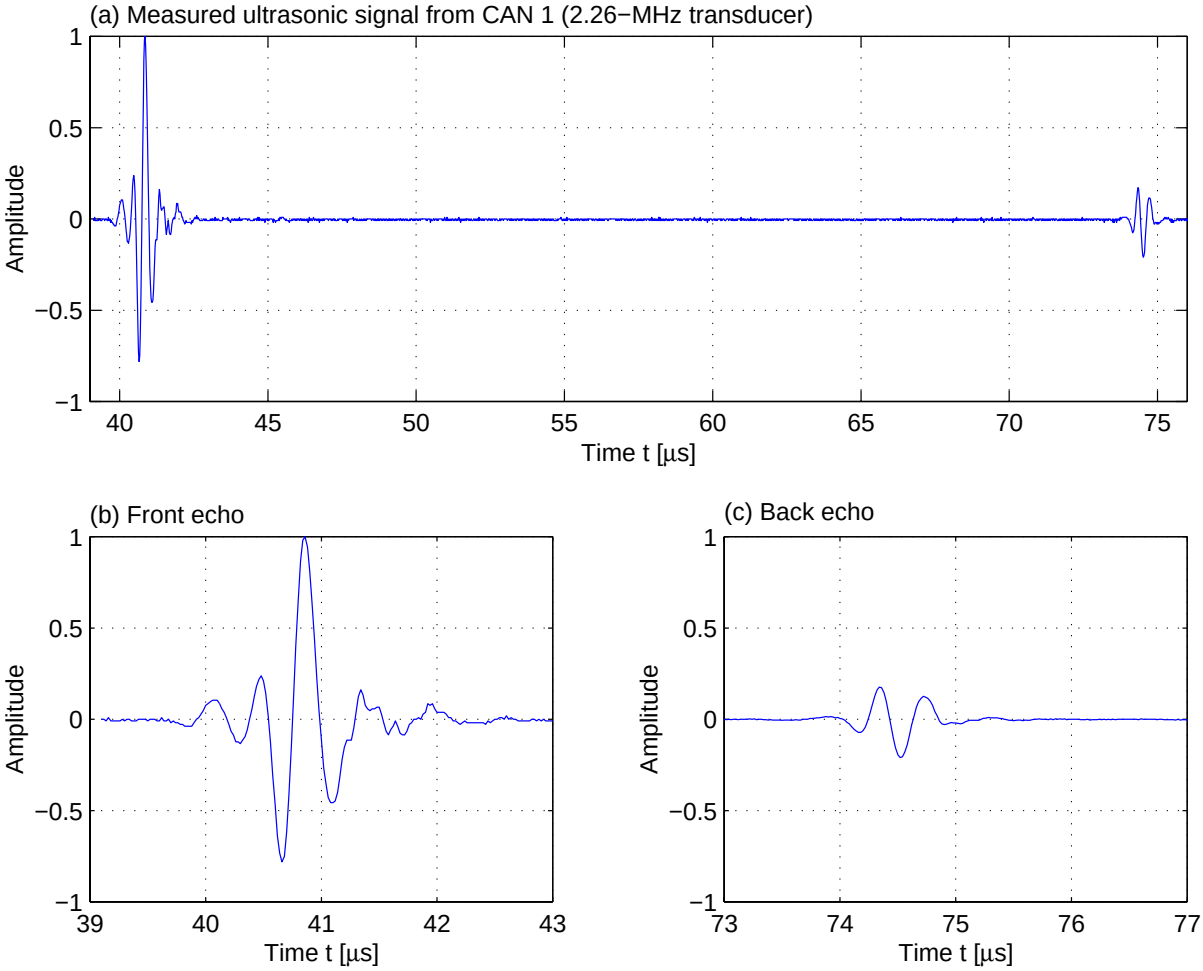

Fig. 3.20. Ultrasonic signal measured using the 2.26-MHz spherically annular transducer on copper block CAN 1. The signal is from the non-welded zone. (a) The overall signal, (b) the front surface echo, and (c) the back surface echo.

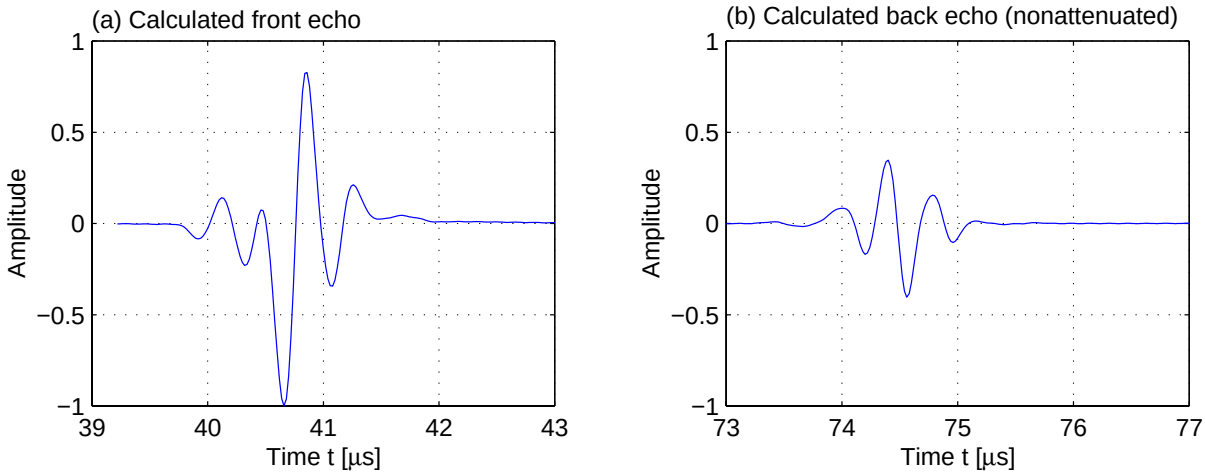

Fig. 3.21. Calculated ultrasonic signals corresponding to those shown in Fig. 3.17. (a) the front surface echo, and (b) the back surface echo.

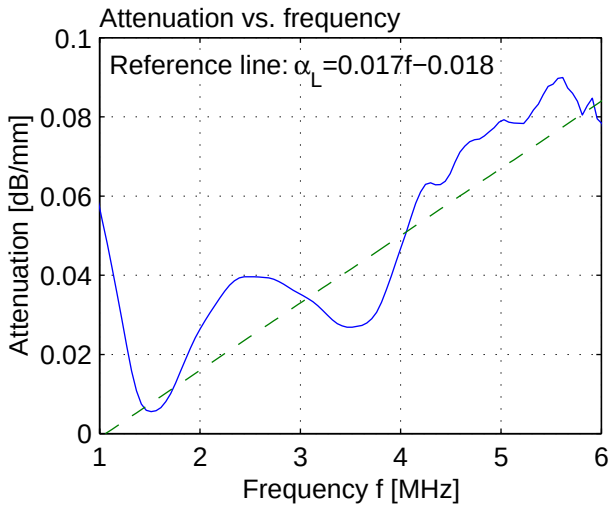

Fig. 3.22. Attenuation versus frequency evaluated using the 2.26 -MHz transducer. Measured and calculated back surface echoes shown in Figs. 3.17(c) and 3.18(b), respectively, were used for the evaluation.

3.4 Conclusions

Quantitative evaluation of attenuation has been performed in pulse-echo mode using two spherically focused transducers with center frequencies of 2.26 and 4.83 MHz. Accurate attenuation evaluation requires correction of transducer diffraction effects. The accurate correction required effective transducer parameters. To achieve this a new method for determining effective geometrical parameters of the transducers was developed. The characterization method is based on the spatial impulse response method used for computing acoustical fields. It is easy to use and requires a simple calculation only. Two transducers have been calibrated using this method so that their effective geometrical parameters, radii and focal lengths, have been determined.

Then a new algorithm, the θ*-space* algorithm, for the ASA has been developed for axisymmetric transducers. It is both efficient and accurate compared to the existing *k-space* algorithm used in the ASA. Acoustic and elastic fields radiated by the spherically focused transducers have been calculated using this algorithm and the effective geometrical parameters.

Attenuation evaluation was carried out in the immersion-pulse-echo scheme in which the pulse echoes from the front and back surfaces were used. By further applying the θ*-space* ASA, the pulse echoes from the copper block CAN 1 immersed in water were calculated so that the diffraction effects were corrected in the calculated results. Using the calculated and measured echoes for the two spherically focused transducers the attenuation in CAN 1 was evaluated. The obtained results show that the attenuation in copper canister is realtively small, its value is in the range of 0.1 dB/mm at 4 MHz.

3.5 References

[1] P. Wu, and T. Stepinski, "Quantitative estimation of ultrasonic attenuation in a solid in the immersion case with correction of diffraction effects," *Ultrasonics*, vol. 38, pp. 481-485, 2000.

[2] P. Wu, and T. Stepinski, *Inspection of Copper Canisters for Spent Nuclear Fuel by Means of Ultrasonic Array System – Electron Beam Evaluation, Modelling, and Materials Characterization*, SKB Technical Report TR-99-43, December 1999.

[3] P. Wu, and T. Stepinski, *Inspection of Copper Canisters for Spent Nuclear Fuel by Means of Ultrasonic Array System - Modelling, Defect Detection and Grain Noise Estimation*, SKB Technical Report TR-99-12, July 1998.

[4] A. O. Williams, "Acoustic intensity distribution from a 'piston' source. – II. The concave piston," *J Acoust. Soc. Am.*, vol. 17, pp. 219-227, 1946.

[5] H.T. O'Neil, "Theory of focusing radiators," *J Acoust. Soc. Am.*, vol. 21(5), pp. 516-526, 1949.

[6] A. Penttinen and M Luukkala, "The impulse response and pressure nearfield of a curved radiator," *J. Phys D, Appl. Phys.* vol. 9, pp. 1547-1557, 1976.

[7] M. Arditi, F.S. Foster, and J.M. Hunt, "Transient fields of concave annular arrays," *Ultrason. Imag.*, vol. 3, pp. 37-61, 1981.

[8] M.A. Fink, and J.-F. Cardoso, "Diffraction effects in pulse-echo measurement," *IEEE Trans Sonics &Ultrason.*, vol. SU-31, pp. 313-329, 1984.

[9] W.A. Verhoef, M.J.T.M. Cloostermans, and J.M. Thijssen, "The impulse response of a focused transducer with an arbitrary axisymmetric surface velocity distribution," *J. Acoust. Soc. Am.*, vol. 75, pp.1716-1721, 1984.

[10] F. Coulouvrat, "Continuous field radiated by a geometrically focused transducer: Numerical investigation and comparison with an approximate model," *J. Acoust. Soc. Am.*, Vol. 94, pp. 1663-1657, 1993.

[11] J. Adach, and R.C. Chivers, "Effective geometrical parameters for a spherical cap transducer," *Acustica*, Vol. 62, pp. 66-74, 1986.

[12] J. Adach, and R.C. Chivers, "A detailed investigation of effective geometrical parameters for weakly focussed ultrasonic transducers. Part I: optimisation of experimental procedures," *Acustica*, Vol. 70, pp. 12-22, 1990.

[13] J. Adach, and R.C. Chivers, "A detailed investigation of effective geometrical parameters for weakly focussed ultrasonic transducers. Part II: a systematic study including an absorbing medium," *Acustica*, Vol. 70, pp. 135-145, 1990.

[14] T.P. Lerch, L.W. Schmerr, and A. Sedov, "Characterization of spherically focused transducers using an ultrasonic measurement model approach," *Res. Nondestr. Eval.*, Vol. 8, pp. 1-12, 1996.

[15] R.C. Chivers, L. Bosselaar, and P. R. Filmore, "Effective area to be used in diffraction corrections," *J. Acoust. Soc. Am.*, vol. 68, no. 1, pp. 80-84, 1980.

[16] J.P. Weight and A.J. Hayman, "Observations of the propagation of very short ultrasonic pulses and their reflection by small targets," *J. Acoust. Soc. Am.* **63:** 396-404 (1978).

[17] A.J. Hayman and J.P. Weight, "Transmission and reception of short ultrasonic pulses by circular and square transducers," *J. Acoust. Soc. Am.* **66:** 945-951 (1979).

[18] A. Lhemery, "Impulse-response method to predict echo-responses from targets of complex geometry. Part I: Theory," *J. Acoust. Soc. Am.* **90:** 2799-2807 (1991).

[19] A. Lhemery, "Impulse-response method to predict echo-responses from targets of complex geometry. Part II: Computer implementation and experimental validation," *J. Acoust. Soc. Am.* **95:** 1790-1800 (1994).

[20] P. Wu, and T. Stepinski, " Spatial impulse response method for predicting pulse-echo fields from a linear array with cylindrically concave surface," *IEEE Ultrason. Ferroelec. Freq. Contr.*, vol. 46, no. 5, pp. 1283-1297, 1999.

[21] T. Stepinski, and P. Wu, *Ultrasonic Inspection of Nuclear Fuel Copper Canisters*, SKB Projektrapport 97-01, December 1996.

[22] T. Stepinski, and P. Wu, *Inspection of Copper Canisters for Spent Nuclear Fuel by Means of Ultrasonic Array System*, SKB Projektrapport 97-06, Augusti 1997.

[23] J.W. Goodman, *Introduction to Fourier Optics*. McGraw-Hill Book Company, New York, (1968).

[24] P. Wu, R. Kazys and T. Stepinski, "Analysis of the numerically implemented angular spectrum approach based on the evaluation of two-dimensional acoustic fields--Part I: Errors due to the discrete Fourier transform and discretization," *J. Acoust. Soc. Am.* **99:** 1339-1348 (1996).

[25] P. Wu, R. Kazys and T. Stepinski, "Analysis of the numerically implemented angular spectrum approach based on the evaluation of two-dimensional acoustic fields--Part II: Characteristics as a function of angular range," *J. Acoust. Soc. Am*. **99:** 1349-1359 (1996).

[26] P. Wu, R. Kazys and T. Stepinski, "Optimal selection of parameters for the angular spectrum approach to numerically evaluate acoustic fields," *J. Acoust. Soc. Am.,* **101**, pp. 125-134, (1997).

[27] P. Wu, and T. Stepinski, "Elastic fields in immersed isotropic solids from phased array: the time harmonic case," *Res. Nondestr. Evla.* **10**: 185-204, (1998).

[28] L.M. Brekhovskikh, *Waves in Layered Media*. 2nd Edition, Academic, New York, Chap. I, (1980).

Appendix 3-A. Spatial impulse response of spherically circular and annular transducers

The spatial impulse response of a spherically circular transducer, $h(\mathbf{r}, t)$, is given in the following table.

$h(\mathbf{r}, t)$	Region I	Region II	Region III
0	$t < t_0$	$t_0^{II} < t$	$t < t_1$
$\frac{cF}{d_F}$	$t_0 < t < t_1$	$t_2 < t < t_0^{II}$	–
$\frac{cF}{d_F}\frac{1}{\pi}\cos^{-1}\left[\frac{\eta(t)}{\sigma(t)}\right]$	$t_1 < t < t_2$	$t_1 < t < t_2$	$t_1 < t < t_2$
0	$t_2 < t$	$t < t_1$	$t_2 < t$

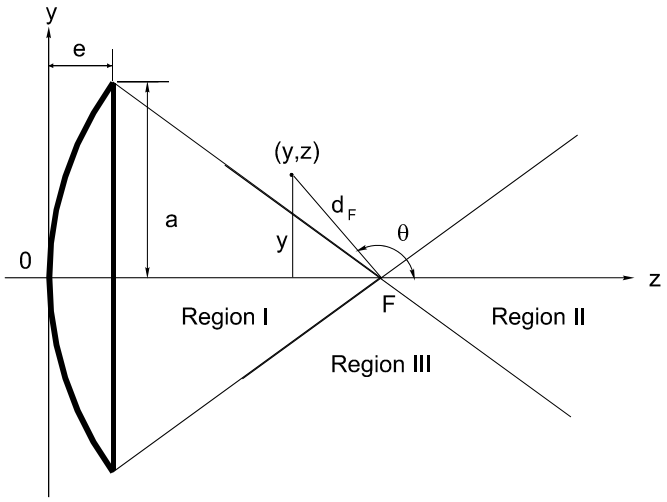

Fig. 3-A.1. Geometry of a spherically focused transducer and the regions specified for its spatial impulse response.

In the table,

$$t_0 = \left(F - d_F\right)/c\,, \tag{3-A.1a}$$

$$t_0^{II} = \left(F + d_F\right)/c\,, \tag{3-A.1b}$$

$$t_1 = \sqrt{(a-y)^2 + (z-e)^2}\,/c\,, \tag{3-A.2}$$

$$t_2 = \sqrt{(a+y)^2 + (z-e)^2}\,/c\,, \tag{3-A.3}$$

$$d_F(y,z) = \sqrt{y^2 + (F-z)^2}\,, \tag{3-A.4}$$

$$e = F - \sqrt{F^2 - a^2}\ , \tag{3-A.5}$$

$$\eta(t) = \left[\frac{F-e}{\sin\theta} + \frac{1}{\tan\theta} \frac{F^2 + d_F^2 - c^2 t^2}{2 d_F} \right], \tag{3-A.6}$$

$$\sigma(t) = \left[F - \left(\frac{F^2 + d_F^2 - c^2 t^2}{2 d_F} \right)^2 \right]^{1/2} . \tag{3-A.7}$$

The three regions specified and some relevant notations are given in Fig. 3-A.1.

The SIR of a spherically focused annular transducer with an inner radius a_1 and an outer radius a_2 can be easily found by

$$h_a(\mathbf{r}, t) = h_{a2}(\mathbf{r}, t) - h_{a1}(\mathbf{r}, t)\,, \tag{3-A.8}$$

where $h_{a1}(\mathbf{r}, t)$ and $h_{a2}(\mathbf{r}, t)$ are the SIRs of the spherically focused transducers with radii a_1 and a_2, respectively.

Appendix 3-B. A new algorithm for implementing the angular spectrum approach for axisymmetric transducers

3-B.1 General consideration

An acoustic field from a curved transducer with surface *S* represented by $z = f(x, y)$ in terms of pressure at frequency ω is expressed by the Rayleigh integral in the following manner [20],

$$\tilde{p}(\mathbf{r}) = -\frac{jk\rho_0 c}{2\pi}\iint_S \tilde{v}_n(\mathbf{r}')\frac{\exp(jkr_s)}{r_s}dS\,, \tag{3-B.1}$$

where $\tilde{v}_n(\mathbf{r}')$ is the normal velocity on the transducer surface, $r_s = |\mathbf{r} - \mathbf{r}'| = \sqrt{(x-x')^2 + (y-y')^2 + [z - f(x', y')]^2}$ is the distance from source point $\mathbf{r}'$ on surface *S* to field point $\mathbf{r}$ in the medium, ρ_0 is the density, *c* is the sound velocity, and $k = \omega / c$ is the wave number. The Rayleigh integral for the curved transducer can be solved by the extended ASA [3],

$$\tilde{p}(x, y, z) = \frac{k\rho_0 c}{(2\pi)^2}\int_{-\infty}^{\infty}\int_{-\infty}^{\infty} V(k_x, k_y; z = z_1)\frac{\exp\left[j\left(xk_x + yk_y + (z - z_1)k_z\right)\right]}{k_z}dk_x dk_y\,,\ (z \geq z_1), \tag{3-B.2}$$

$$V(k_x, k_y; z = z_1) = \iint_{S_{xy}} \frac{\tilde{v}_n(x', y', f(x', y'))}{\cos\theta_z}\exp\left[-j(x'k_x + y'k_y)\right]\exp\left[j(z_1 - f(x', y'))k_z\right]dx'dy', \tag{3-B.3}$$

where $k_x = kn_x$, $k_y = kn_y$, $k_z = \sqrt{k^2 - k_x^2 - k_y^2} = k\sqrt{1 - n_x^2 - n_y^2}$ are the spatial frequencies in the *x*-, *y*- and *z*-directions, respectively, S_{xy} is the area of the projection of the surface *S* onto the *x*-*y* plane,

$$\cos\theta_z = \frac{1}{\sqrt{(f_x(x, y))^2 + (f_y(x, y))^2 + 1}}, \tag{3-B.4}$$

where $f_x(x, y)$ and $f_y(x, y)$ are the partial derivatives with respect to *x* and *y*, respectively. In Eq. (3-B.3), the condition $z_1 \geq \max[f(x', y')]$ must be met in order to ensure that $V(k_x, k_y; z = z_1)$ is

always finite for all k_x and k_y. Eqs. (3-B.2) and (3-B.3) constitute the conventional algorithm of implementing the ASA and the extended ASA.

In the polar coordinates, using the following relations of the coordinate transform,

$$x = \rho\cos\varphi,\ y = \rho\sin\varphi, \tag{3-B.5}$$

$$k_x = k_\rho\cos\psi,\ k_y = k_\rho\sin\psi, \tag{3-B.6}$$

the transducer surface equation is of the form of $z = f(\rho,\varphi)$, and Eqs. (3-B.2) – (3-B.4) becomes,

$$\tilde{p}(\rho,\varphi,z) = \frac{k\rho_0 c}{(2\pi)^2}\int_0^{2\pi}\int_0^{\infty} V(k_\rho,\psi,z=z_1)\exp\left[j\rho k_\rho\cos(\varphi-\psi)\right]\frac{\exp\left[j(z-z_1)k_z\right]}{k_z}k_\rho dk_\rho d\psi, \tag{3-B.7}$$

$$V(k_\rho,\psi,z=z_1) = \int_0^{2\pi}\int_0^{\infty}\frac{\tilde{v}_n(\rho,\varphi,f(\rho,\varphi))}{\cos\theta_z}\exp\left[-jk_\rho\rho\cos(\varphi-\psi)\right]\exp\left[j(z_1-f(\rho,\varphi))k_z\right]\rho d\rho d\varphi, \tag{3-B.8}$$

$$\cos\theta_z = \frac{1}{\sqrt{(f_\rho(\rho,\varphi))^2+(f_\varphi(\rho,\varphi))^2+1}}, \tag{3-B.9}$$

where $k_\rho = kn_\rho$, $k_z = \sqrt{k^2-k_\rho^2} = k\sqrt{1-n_\rho^2}$, $f_\rho(\rho,\varphi)$ and $f_\varphi(\rho,\varphi)$ are the partial derivatives with respect to ρ and φ, respectively.

3-B.2 Algorithms for implementing the ASA for axisymmetric transducers

For a transducer that is axisymmetric, the surface equation $z = f(x,y)$ becomes $z = f(\sqrt{x^2+y^2}) = f(\rho)$, and Eqs. (3-B.7) – (3-B.9) becomes,

$$\tilde{p}(\rho,z) = \frac{k\rho_0 c}{2\pi}\int_0^{\infty} V(k_\rho,z=z_1)J_0(\rho k_\rho)\frac{\exp\left[j(z-z_1)k_z\right]}{k_z}k_\rho dk_\rho, \tag{3-B.10}$$

$$V(k_\rho,z=z_1) = 2\pi\int_0^{\infty}\frac{\tilde{v}_n(\rho,f(\rho))}{\cos\theta_z}J_0(k_\rho\rho)\exp\left[j(z_1-f(\rho))k_z\right]\rho d\rho, \tag{3-B.11}$$

$$\cos\theta_z = \frac{1}{\sqrt{(f_\rho(\rho))^2+1}}, \tag{3-B.12}$$

where $J_0(x)=(1/2\pi)\int_0^{2\pi} e^{jx\cos\theta}d\theta$ is the zeroth-order Bessel function. For a planar transducer located in the plane of z=0, $\cos\theta_z$ =1, $f(\rho)$ =0, and Eqs. (3-B.11) and (3-B.10) become the zeroth-order Hankel transform. Since this algorithm conducts the calculation of angular spectra and fields in the *k*-space, it is called *k-space* algorithm.

Our early research [21,22,24-26] has shown that aliasing error exists because $\exp[j(z-z_1)k_z]$ in Eq. (3-B.10) is always undersampled. Thus some optimal selection of numerical parameters is necessary to minimize the aliasing error in calculations. Here we propose another method to reduce the aliasing error and to improve the calculation accuracy.

By making a variable transformation of

$$k_\rho = k\sin\theta\,, \tag{3-B.13}$$

Eq. (3-B.10) turns out to be

$$\begin{aligned}\tilde{p}(\rho,z) &= \frac{k\rho_0 c}{2\pi}\lim_{n_\rho\to\infty}\int_0^{\arcsin(n_\rho)} V(\theta,z_1)J_0(\rho k\sin\theta)\frac{\exp[j(z-z_1)k\cos\theta]}{k\cos\theta}k\sin\theta k\cos\theta d\theta \\ &= \frac{k^2\rho_0 c}{2\pi}\left\{\int_0^{\pi/2} V(\theta,z_1)J_0(\rho k\sin\theta)\sin\theta\exp[j(z-z_1)k\cos\theta]d\theta\right. \\ &\left. + \int_0^{\infty} V(\beta,z_1)J_0(\rho k\cosh\beta)\cosh\beta\exp[-(z-z_1)k\sinh\theta]d\beta\right\}.\end{aligned} \tag{3-B.14}$$

In Eq. (3-B.14), the following things have been considered. Since the integration limits to k_ρ are from 0 to infinity, then $n_\rho = k_\rho/k = \sin\theta$ goes from 0 to infinity. Therefore, θ will be real valued for $n_\rho \le 1$ and θ becomes imaginary for n_ρ>1. When θ is real, it ranges from 0 to $\pi/2$, and in this case, θ is the angle of the propagation direction of a plane wave with respect to the *z*-axis, and θ =0 for n_ρ=0, and $\theta=\pi/2$ for n_ρ=1. When it is imaginary θ will be replaced with $j\beta$. Obviously, in Eq. (3-B.14) the first term represents the homogeneous waves and the second represents the inhomogeneous waves that attenuate very rapidly as *z* increases because of $\exp[-zk\sinh\theta]$. In Eq. (3-B.14), it can be seen that in this case the singular point at the lower limit (θ =0) is eliminated.

The angular spectrum in Eq. (3-B.11) turns out to be

$$V(\theta, z_1) = 2\pi \int_0^{\infty} \frac{\tilde{v}_n(\rho, f(\rho))}{\cos\theta_z} J_0(k \sin\theta\rho) \exp[j(z_1 - f(\rho))k\cos\theta]\rho d\rho \,. \tag{3-B.15}$$

From the variable transformation in Eq. (3-B.13), it follows that, if θ is sampled in equal angular interval $\Delta\theta$ =*constant*, then k_ρ (or n_ρ) is sampled in unequal interval. Since this algorithm conducts the calculation of angular spectra and fields in the θ-space, it is called θ*-space* algorithm. This will yield a good reduction of aliasing error, which will be shown in the following section.

It should be noted that the inhomogeneous parts, $\int_k^{\infty}(\cdot)dk_\rho$, in Eq. (3-B.10) and, $\int_0^{\infty}(\cdot)d\beta$, in Eq. (3-B.14) attenuates very rapidly as *z* increases, and thus are neglected almost without loss of accuracy when *z* is not extremely close to the transducer surface. In the present study, therefore, only the homogeneous part will be used to construct the field.

3-B.3 A special case: spherically focused transducers

A spherically focused transducer is axisymmetric. Consider the transducer that has a uniform normal velocity on its surface, has a geometry with radius *a* and focal length *F*, and is positioned in such a way as shown in Fig. 3.1. Mathematically, the normal velocity is expressed by

$$\tilde{v}_n(\rho, f(\rho)) = 1, \tag{3-B.16}$$

the surface can be represented by the equation,

$$z = f(\rho) = F - \sqrt{F^2 - \rho^2}\ , (\rho \le a). \tag{3-B.17}$$

Eqs. (3-B.12) becomes

$$\cos\theta_z = \sqrt{F^2 - \rho^2}\,/F \,. \tag{3-B.18}$$

Eqs. (3-B.10) and (3-B.11) (for the *k-space* algorithm) become

$$\tilde{p}(\rho, z) = \frac{k\rho_0 c}{2\pi} \int_0^{k} V(k_\rho, z_1) J_0(\rho k_\rho) \frac{\exp[j(z - z_1)k_z]}{k_z} k_\rho dk_\rho \,, \tag{3-B.19}$$

$$V(k_\rho, z_1) = 2\pi F \int_0^a \frac{J_0(k_\rho \rho)}{\sqrt{F^2 - \rho^2}} \exp\left[j\left(z_1 - F + \sqrt{F^2 - \rho^2} \right) k_z \right] \rho d\rho , \tag{3-B.20}$$

in which the inhomogeneous waves are neglected.

Eqs. (3-B.14) and (3-B.15) (for the θ *-space* algorithm) become

$$\tilde{p}(\rho, z) = \frac{k^2 \rho_0 c}{2\pi} \int_0^{\pi/2} V(\theta, z_1) J_0(\rho k \sin\theta) \sin\theta \exp[j(z - z_1) k \cos\theta] d\theta , \tag{3-B.21}$$

$$V(\theta, z_1) = 2\pi F \int_0^a \frac{J_0(\rho k \sin\theta)}{\sqrt{F^2 - \rho^2}} \exp\left[j\left(z_1 - F + \sqrt{F^2 - \rho^2} \right) k \cos\theta \right] \rho d\rho , \tag{3-B.22}$$

in which the inhomogeneous waves are neglected.

For a spherically annular transducer with inner and outer radii, a_1 and a_2, the algorithm only needs a small modification for the angular spectrum calculation, that is, replacing the lower limit 0 and the upper *a* in Eqs. (3-B.20) and (3-B.22) with a_1 and a_2, respectively. Actually, a spherically circular transducer can be thought of as a special case of the annular transducer with a_1=0 and a_2=*a*.

3-B.4 Efficiency and accuracy

The efficiency of the new algorithm (the θ *-space* algorithm), Eqs. (3-B.21) and (3-B.22), will be demonstrated by comparing with the *k-space* algorithm, Eqs. (3-B.19) and (3-B.20), in the case of the spherically circular transducer. The transducer is assumed to have a uniform normal velocity (v_n =constant) on the surface, a 9.86-mm radius and a 223.5-mm focal length.

To minimized the aliasing error, sampling frequency larger than or equal to Nyquist frequency should be used. For the *k-space* algorithm, it is $\exp\left[j(z - z_1)\sqrt{1 - k_\rho^2} \right]$ that should be sampled at a sufficiently fine sampling interval (i.e., a sufficiently high rate) with respect to k_ρ, but it is undersampled in most cases, and thus some optimization is necessary [24-26]. For the θ *-space* algorithm, it is $\exp[j(z - z_1) k \cos\theta]$ that needs being sufficiently sampled. Since the "instantaneous frequency" of $\exp[j(z - z_1) k \cos\theta]$ is [25]

$$f_I(\theta) = \frac{1}{2\pi} \frac{d}{d\theta} [(z - z_1) k \cos\theta] = \frac{(z - z_1)}{\lambda} \sin\theta . \tag{3-B.23}$$

To eliminate the aliasing error the sampling frequency used needs to meet the Nyquist frequency requirement, that is,

$$F_{sample} \geq \frac{2(z - z_1)}{\lambda} \geq \frac{2(z - z_1)}{\lambda} \sin\theta = 2 f_I(\theta), \tag{3-B.24}$$

where λ is the wavelength in the medium. From the above equation it follows that the number of sampling points for $\theta = 0 \sim \pi/2$ is

$$N_s \geq \frac{2(z_{\max} - z_1)}{\lambda}, \tag{3-B.25}$$

where $z_{\max}$ is the maximum dimension of the field to be calculated in the *z*-direction. The above equation will be used in the following calculations.

To evaluate the accuracy and efficiency of the two algorithms, the on-axis acoustical fields of the spherically focused transducer are calculated from the algorithms and compared with the analytical solution [4,5],

$$\tilde{p}(\rho, z) = \frac{\rho_0 c v_n e^{-j\omega t}}{1 - z/F} \left\{ \exp[jkz] - \exp\left[jk\sqrt{z^2 + (1 - z/F) 4F^2 \sin\left(\frac{\alpha}{2}\right)} \right] \right\}, \tag{3-B.26}$$

where $\alpha = \arcsin(a/F)$.

The angular spectra calculated by the *k*- and θ-space algorithms are shown in Fig. 3-B.1(a) and (b), respectively. The difference is the horizontal axis, the direction cosine n_ρ in Fig. (a), whereas the angle θ in Fig. (b). The sampling points used are 4500 for the *k*-space algorithm and only 1500 for the θ-space algorithm. But the field constructed from the k-space algorithm shows large aliasing error (Fig. 3-B.2(a)), whereas the field from the θ-space algorithm has very small aliasing error (Fig. 3-B.2(b)). This demonstrates that the θ-space algorithm is much better than the k-space algorithm, both in efficiency and accuracy.

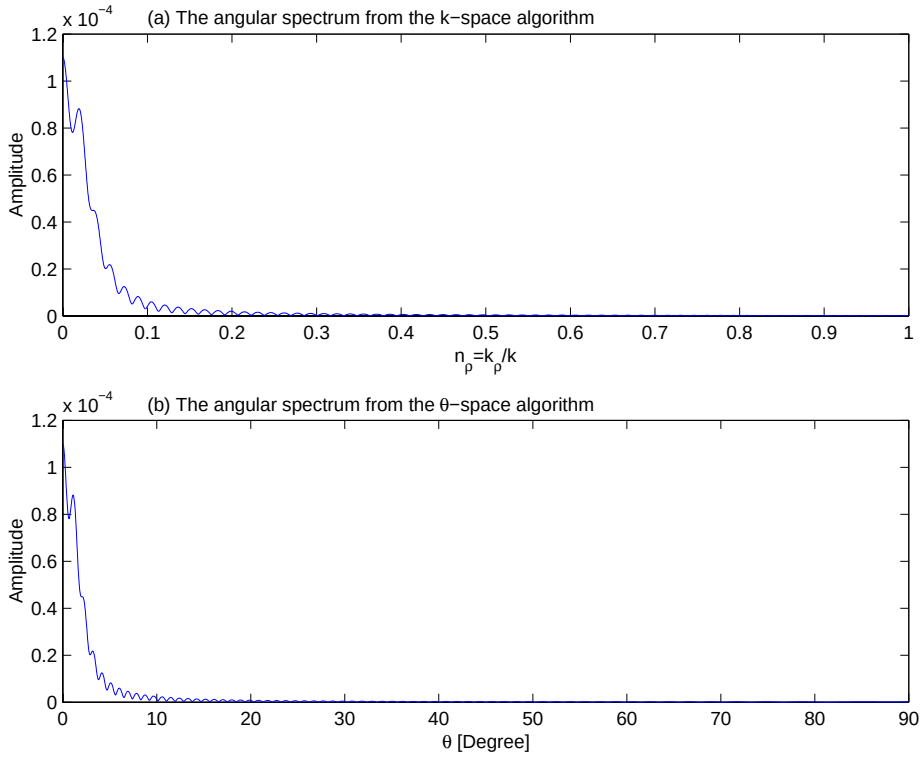

Fig. 3-B.1. Angular spectra of the spherically circular transducer calculated from (a) the k-space method and (b) the θ -spcae method.

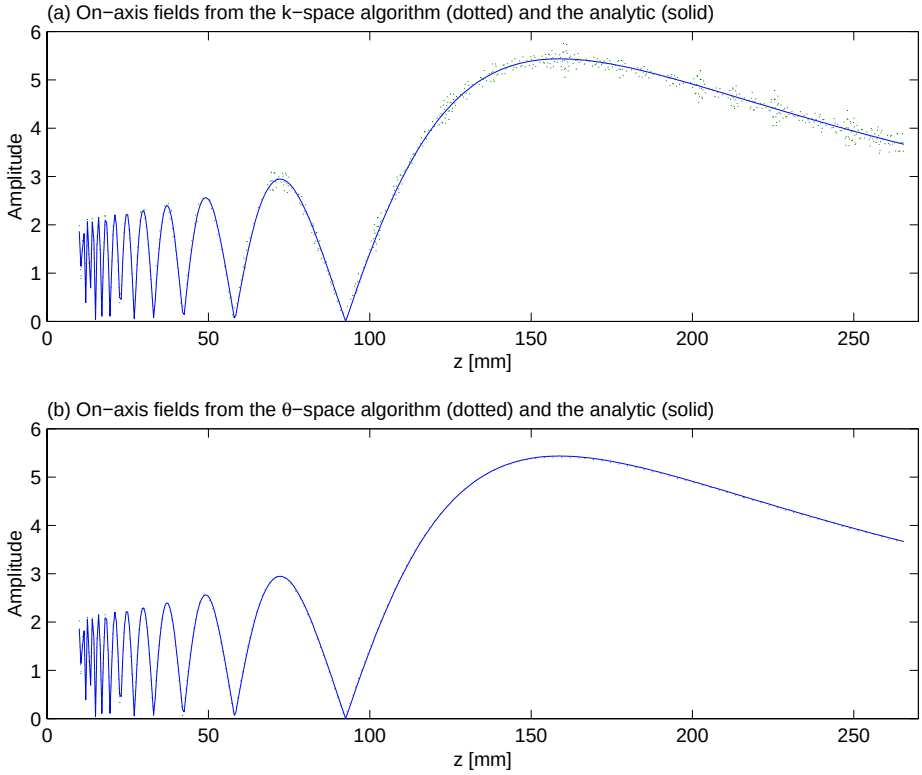

Fig. 3-B.2. Comparison of the on-axis fields of the spherically circular transducer calculated from the analytic solution (solid) and from (a) the k-space algorithm (dotted), and (b) the θ -space algorithm (dotted).

Appendix 3-C. Theories of the ASA for modeling acoustic and elastic fields from axisymmetric transducers

In this appendix, the theories of the ASA for modeling acoustic and elastic fields radiated by axisymmetric transducers are presented. An acoustic field is the field in a fluid, and an elastic field is the one radiated by a transducer into a solid. In the present case, the sloid is a plate with planar surfaces and immersed in a fluid. Assuming that such a solid plate has a thickness of D and its two interfaces are positioned at $z= z_{fs}$ and $z= z_{fs}+D$. At both interfaces, reflection and refraction will occur. The reflected and refracted fields will be formulated below.

It is known that a time-harmonic field of the curved transducer with $\tilde{v}_n(x, y, z; \omega)$ can be represented by an angular spectrum of plane waves, $V(k_x, k_y; z_1)$, in a plane at $z= z_1$. For a axisymmetric transducer, the angular spectrum (in the $z= z_1$ plane) in a fluid can be calculated by (Eq. (3-B.15) in Appendix 3-B)

$$V(\theta, z_1) = 2\pi \int_0^{\rho} \frac{\tilde{v}_n(\rho, f(\rho))}{\cos\theta_z} J_0(k \sin\theta\rho) \exp[j(z_1 - f(\rho))k\cos\theta]\rho d\rho \,. \tag{3-C.1}$$

Spherically focused (circular or annular) transducers are a special case of the axisymmetric transducers. A spherically circular transducer can be thought of as a special case of the annular transducer with a_1=0 and a_2=a.

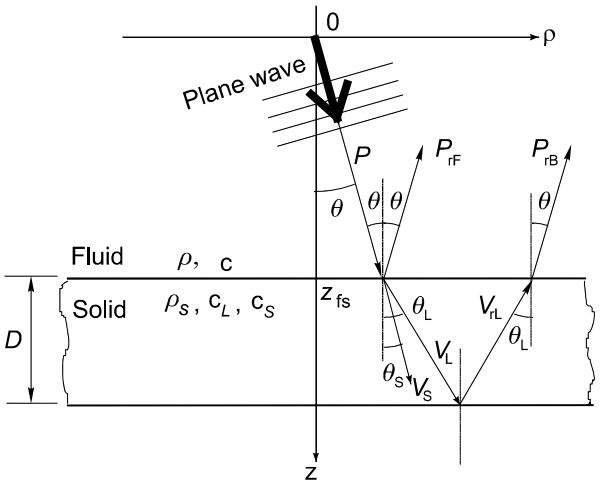

Fig. 3-C.1. Propagation of a plane wave in a fluid and a solid plate immersed in the fluid.

A pressure plane wave in the fluid at point (ρ, z) can, thus, be expressed by

$$P(\theta;\rho,z) = \rho_0 c k^2 V(\theta, z_1) J_0(\rho k \sin\theta) \sin\theta \exp\left[j(z - z_1) k \cos\theta\right]. \qquad \text{(3-C.2)}$$

The propagation of this plane wave in a fluid and a solid plate immersed in the fluid is shown in Fig. 3-C.1. When this pressure plane wave in Eq. (3-C.2) propagates on the immersed solid plate it will, at interface $z = z_{fs}$ ($> z_1$), be partly reflected back into the fluid, and partly transmitted into the solid in the modes of a longitudinal wave (LW), a shear wave (SW), or other wave modes. Here only the LW is considered.

The reflected wave at the front interface ($z = z_{fs}$) can be written, in terms of pressure, as

$$\begin{aligned} P_{rF}(\theta;\rho,z) &= R_{fs}(\theta) P(\theta;\rho,z_{fs}) \exp\left[-j(z - z_{fs}) k \cos\theta\right] \\ &= \rho_0 c k^2 V(\theta, z_1) J_0(\rho k \sin\theta) \sin\theta \exp\left[-j(z + z_1 - 2z_{fs}) k \cos\theta\right], \quad (z \le z_{fs}), \end{aligned} \qquad \text{(3-C.3)}$$

where $R_{fs}(\theta)$ is the reflection coefficient at the fluid/solid interface.

The transmitted LW in terms of particle velocity can be written as

$$\begin{aligned} \mathbf{V}_L(\theta;\rho,z) &= \frac{\hat{\mathbf{L}} k_L T_{fs}(\theta) P(\theta;\rho,z_{fs}) \exp\left[j(z - z_{fs}) k_{zL}\right]}{k \rho_0 c}, \\ &= \hat{\mathbf{L}} k_L k T_{fs}(\theta) V(k \sin\theta, z_1) J_0(\rho k \sin\theta) \sin\theta \exp\left[j(z_{fs} - z_1) k \cos\theta + j(z - z_{fs}) k_L \cos\theta_L\right] \\ &\qquad (z \ge z_{fs}), \end{aligned} \qquad \text{(3-C.4)}$$

where $T_{fs}(\theta)$ is the transmission coefficient at the fluid/solid interface, $\hat{\mathbf{L}} = (\hat{\boldsymbol{\rho}} \sin\theta_L + \hat{\mathbf{z}} \cos\theta_L)$ is a unit vector defining the propagation and polarization directions, $k_{zL} = k_L \cos\theta_L$, and θ_L is the LW refraction angle determined from the incident angle θ and the Snell's law stating $k \sin\theta = k_L \sin\theta_L$.

At the back (solid/fluid) interface ($z = z_{fs} + D$), the transmitted LW is reflected and the reflected LW can be written as

$$\begin{aligned} \mathbf{V}_{rL}(\theta;\rho,z) &= \hat{\mathbf{L}}_r R_{sf}(\theta) V_L(\theta;\rho,z_{fs} + D) \exp\left[-j(z - z_{fs} - D) k_{zL}\right] \\ &= \hat{\mathbf{L}}_r k_L k R_{sf}(\theta) T_{fs}(\theta) V(k \sin\theta, z_1) J_0(\rho k \sin\theta) \sin\theta \\ &\quad \times \exp\left[j(z_{fs} - z_1) k \cos\theta - j(z - z_{fs} - 2D) k_L \cos\theta_L\right] \\ &\qquad (z_{fs} \le z \le z_{fs} + D), \end{aligned} \qquad \text{(3-C.5)}$$

where $R_{sf}(\theta)$ is the reflection coefficient at the solid/fluid interface, and $\hat{\mathbf{L}}_r = (\hat{\boldsymbol{\rho}}\sin\theta_L - \hat{\mathbf{z}}\cos\theta_L)$. At the front (solid/fluid) interface ($z = z_{fs}$), the reflected LW $\mathbf{V}_{rL}$ is transmitted, and the transmitted LW in the fluid in terms of pressure again can be written as

$$\begin{aligned} P_{rB}(\theta;\rho,z) &= \frac{k\rho_0 c T_{sf}(\theta) V_{rL}(\theta;\rho,z_{fs}) \exp\left[-j(z-z_{fs})k_z\right]}{k_L} \\ &= \rho_0 c k^2 T_{sf}(\theta) R_{sf}(\theta) T_{fs}(\theta) V(k\sin\theta, z_1) J_0(\rho k\sin\theta)\sin\theta \\ &\qquad \times \exp\left[-j(z-2z_{fs}+z_1)k\cos\theta + j2Dk_L\cos\theta_L\right] \\ &= \frac{T_{sf}(\theta)R_{sf}(\theta)T_{fs}(\theta)}{R_{fs}(\theta)} \exp\left[j2Dk_L\cos\theta_L\right] P_{rF}(\theta,\rho,z), \ (z \le z_{fs}). \end{aligned} \tag{3-C.6}$$

The reflection and refraction coefficients at the fluid/solid interface, R_{fs} and T_{fs}, and those at the solid/fluid interface, R_{sf} and T_{sf}, are given in [28]. Inserting the relations $k_L = k_{0L} + j\alpha_L$ into the above equation, the LW attenuation of the solid plate can be explicitly expressed.

The acoustic ($\tilde{p}$, $\tilde{p}_{rF}$ and $\tilde{p}_{rB}$) and elastic fields ($\tilde{v}_L$ and $\tilde{v}_{rL}$) due to the radiation by an axisymmetric transducer can be obtained by superimposing the corresponding decomposed components (P, P_{rF}, P_{rB}, V_L and V_{rL} in Eqs. (3-C.2), (3-C.3), (3-C.6), (3-C.4), and (3-C.5), respectively) in the following general relation,

$$\tilde{g}(\rho,z) = \frac{1}{2\pi}\int_0^{\pi/2} G(\theta,\rho,z)\,d\theta\,. \tag{3-C.7}$$

ISSN 1404-0344

CM Digitaltryck AB, Bromma, 2001